DOE/ER/03072--49

DE89 011592

DOE/ER/3072-49

Princeton University
Elementary Particles Laboratory
Department of Physics

HUNTING FOR THE RARE DECAY $K^+ \to \pi^+\mu^+\mu^-$

Mats A. Selen

January 1989

DISCLAIMER

Department of Energy Contract DE-AC02-76ER03072

Hunting for the rare decay $K^+ \rightarrow \pi^+\mu^+\mu^-$

MATS A. SELEN

A dissertation
presented to the Faculty
of Princeton University
in candidacy for the degree of
Doctor of Philosophy

Recommended for acceptance
by the Department of Physics

January 1989

Abstract

This thesis describes an experimental search for the rare decay $K^+ \to \pi^+\mu^+\mu^-$. The data were accumulated during two weeks of running Brookhaven AGS experiment E787. Offline event reconstruction reduces the sample to three candidates. If one assumes all three events are background, then an upper limit of 2.1×10^{-7} is set at the 90% confidence level. Two of these events cannot be explained in terms of the major background channel. Assuming the background is sufficiently understood, the interpretation of these two candidates as genuine $K^+ \to \pi^+\mu^+\mu^-$ events results in a measured branching ratio of $(6.1 \pm 4) \times 10^{-8}$.

An upper limit on the process $K^+ \to \pi^+ H$, $H \to \mu^+\mu^-$ is found as a function of Higgs mass in the interval $2m_\mu \leq M_H \leq 320$ MeV. This limit never exceeds 1.5×10^{-7} at the 90% confidence level.

We also set an upper limit on the decay mode $K^+ \to \mu^+\nu\mu^+\mu^-$ of 3.7×10^{-7} at the 90% confidence level. This is the first experimental limit set on this process.

to Judy, Jimmy and Emily.

Acknowledgements

This thesis belongs to my wife Judy, and my kids Jim and Emily. They stand by me with endless patience while I selfishly indulge in this great little game we call physics.

The reason I enjoy my work as much as I do, is that I get to hang out with some wonderful people. My advisor Stew Smith is definitely at the top of this list. He has helped us out countless times, and he and his wife Norma have been like our family. I could go on, but I should probably try and keep this brief.

Dan Marlow, Peter Meyers and Bill Louis are three of the brightest guys I've had the pleasure of calling friends, and I hope some of their smarts have rubbed off during my endless barrage of stupid questions. Frank Shoemaker has forgotten more electronics than I'll ever know, and has taught me plenty.

The remainder of my friends are mostly students like myself. Dan, Dimitri, John, Ken, Bill, Hien, and all the rest. Lorraine is not a student, but luckily she doesn't mind hanging out with me anyway. Life at this place would not have been much fun without you guys.

Thanks also to Prof. Fitch for reading my thesis when he had better things to do. Sorry if I was a pain in the ass!

Before I wrap this up, let me acknowledge two more people who have influenced me greatly. Innes MacKenzie and Jack MacDonald got me started in physics, and have been my friends for ten years.

Finally, I'd like to thank my father and mother for teaching me to work hard and hate mediocrity. It doesn't sound like much, but it's probably the most important thing I'll ever learn.

Contents

1. Introduction

About 15 years ago, a theory known as the standard model[1] was introduced which made specific predictions about the interactions between subatomic particles. It was confirmed experimentally that the model correctly described to first order the behavior of the microworld, but it also made specific predictions about the finer details of particle interactions that have yet to be verified. A drawback of the model is that, even though it explains all observed electro-weak phenomena, it contains several parameters that must be put in "by hand" without any fundamental motivation. For this reason it is essential that the attempt be made to explore the finer details of its predictive ability.

Brookhaven AGS experiment E787 was conceived, designed and constructed for the purpose of studying rare decays of the K^+ meson with sufficient sensitivity to probe the standard model to second order. Specifically, E787 was designed to improve the present limit on $K^+ \rightarrow \pi^+\nu\bar{\nu}$ from 1.4×10^{-7}[2] to 2×10^{-10}, roughly three orders of magnitude.

The experimental apparatus is also well suited for detecting $K^+ \rightarrow \pi^+\mu^+\mu^-$, which is the topic of this thesis. In contrast to $\pi\nu\bar{\nu}$, the interpretation of $\pi\mu\mu$ results in terms of second order weak interactions is difficult since the main expected contribution to this decay rate is due to long range electromagnetic effects. On the plus side, this decay mode has never been experimentally observed, and the predicted branching ratio is such that we hope to see some events. In the following sections we will see that other interesting physics can also be probed via a careful study of $K^+ \rightarrow \pi^+\mu^+\mu^-$.

The experiment is a collaborative effort among Brookhaven National Laboratory, Princeton University, and TRIUMF, and was approved in the fall of 1983. The first actual data-taking took place in the spring of 1988, and it is data from this run that is the topic of this thesis.

1.1 Background Information

Kaons have historically provided a rich source of insight into the nature of fundamental interactions[1].

- The concept of *associated production* was introduced in 1952 by Pais[3] to explain why K's and Λ's are easy to produce yet decay relatively slowly. This in turn led Gell-Mann[4] and Nishijima[5] to introduce the additive quantum number *strangeness*.
- The observation that $K^+ \to \pi^+\pi^0$ and $K^+ \to \pi^+\pi^+\pi^-$ both occur with high probability even though the final states have opposite parity (the $\tau-\theta$ puzzle), led Lee and Yang (in 1956) to propose that parity is *not* conserved in weak interactions[6].
- The observation of the decay $K_L^0 \to \pi^+\pi^-$ by Christenson, Cronin, Fitch, and Turlay in 1964 led to the conclusion that CP invariance can indeed be violated[7].
- The absence of $\Delta S = 1$ neutral currents, specifically the supression of $K^0 \to \mu^+\mu^-$, led Glashow, Iliopoulos and Maiani to propose the GIM mechanism in 1970[8]. A consequence of this was the predicted existence of the *charm* quark.

The use of K's as a tool to study fundamental interactions is attractive for several experimental reasons:

- The copious quantity in which K's can be produced at relatively low energy machines* allows high statistics experiments to be carried out. For example, the AGS can produce 5×10^{12} protons/spill at 30 GeV. This translates to a K^+ intensity of about 5×10^5/spill entering the E787 detector. If $\sim 2\times10^5$/spill of these are successfully stopped in the fiducial stopping region of the detector, then 1000 hours of running with a spill cycle of 3 seconds yields a sample of $\sim 2.4\times10^{11}$ K^+ decays!
- The relatively long mean life of the $K^\pm$, 12.4 ns, allows the construction of elaborate secondary beamlines.
- Although there is no shortage of possible decay modes for a charged kaon (see table 1), the kinds of particle that can appear in the final state are limited by the mass of the K to be only π's, μ's, e's, ν's and γ's. This simplifies the task of secondary particle identification.

* By today's standards of high energy accelerators.

Particle	$I^G(J^P)C_a$ [a]	Mass [b] (MeV) Mass^2 (GeV^2)	Mean life [b] (sec) $c\tau$ (cm)	Partial decay mode: Mode	Fraction [b]	p or p_{max} [c] (MeV/c)
STRANGE MESONS [a]						
				K^+ (or K^- CC)		
$K^\pm$	$\frac{1}{2}(0^-)$	493.667 ±0.015 m^2=0.2437	1.2371×10^{-8} ±0.0026 S=1.9* $c\tau$=370.9 $(\tau^+ - \tau^-)/\bar{\tau}$= (0.11 ±0.09)% (test of CPT) S=1.2*	$\mu^+\nu$	(63.50 ± 0.16)%	236
				$\pi^+\pi^0$	(21.16 ± 0.15)%	205
				$\pi^+\pi^+\pi^-$	(5.59 ± 0.03)% S=1.1*	125
				$\pi^+\pi^0\pi^0$	(1.73 ± 0.05)% S=1.4*	133
				$\pi^0\mu^+\nu$	(3.20 ± 0.09)% S=1.7*	215
				$\pi^0 e^+\nu$	(4.82 ± 0.05)% S=1.1*	228
				$\mu^+\nu\gamma$	[e](5.8 ± 3.5)$\times10^{-3}$	236
				$\pi^0\pi^0 e^+\nu$	(1.8 $^{+2.4}_{-0.6}$)$\times10^{-5}$	207
				$\pi^+\pi^- e^+\nu$	(3.90 ± 0.15)$\times10^{-5}$	203
				$\pi^+\pi^+ e^-\bar{\nu}$	(<1.2)$\times10^{-8}$	203
				$\pi^+\pi^-\mu^+\nu$	(1.4 ± 0.9)$\times10^{-5}$	151
				$\pi^+\pi^+\mu^-\bar{\nu}$	(<3.0)$\times10^{-6}$	151
				$e^+\nu$	(1.54 ± 0.07)$\times10^{-5}$	247
				$e^+\nu\gamma$ (SD+)[h]	(1.52 ± 0.23)$\times10^{-5}$	247
				$e^+\nu\gamma$ (SD−)[h]	(<1.6)$\times10^{-4}$	247
				$\pi^+\pi^0\gamma$	[i,e](2.75 ± 0.16)$\times10^{-4}$	205
				$\pi^+\pi^+\pi^-\gamma$	[e](1.0 ± 0.4)$\times10^{-4}$	125
				$\pi^0\mu^+\nu\gamma$	[e](<6)$\times10^{-5}$	215
				$\pi^0 e^+\nu\gamma$	[e](3.7 ± 1.4)$\times10^{-4}$	228
				$\pi^+ e^+ e^-$	(2.7 ± 0.5)$\times10^{-7}$	227
				$\pi^- e^+ e^+$	(<1)$\times10^{-8}$	227
				$\pi^+\mu^+\mu^-$	(<2.4)$\times10^{-6}$	172
				$\pi^+\gamma\gamma$	[e](<3.5)$\times10^{-5}$	227
				$\pi^+\gamma\gamma\gamma$	[e](<3.0)$\times10^{-4}$	227
				$\pi^+\nu\bar{\nu}$	(<1.4)$\times10^{-7}$	227
				$\pi^+\gamma$	(<4)$\times10^{-6}$	227
				$\pi^\pm e^+\mu^\pm$	(<7)$\times10^{-9}$	214
				$\pi^+ e^-\mu^+$	(<5)$\times10^{-9}$	214
				$e^+\nu\nu\bar{\nu}$	(<6)$\times10^{-5}$	247
				$\mu^+\nu\nu\bar{\nu}$	(<6)$\times10^{-6}$	236
				$\mu^+\nu e^+ e^-$	(11 ± 3)$\times10^{-7}$	236
				$\mu^-\nu e^+ e^+$	(<2.0)$\times10^{-8}$	236
				$e^+\nu e^+ e^-$	(2 $^{+2}_{-1}$)$\times10^{-7}$	247
				$\mu^+\nu_e$	(<4)$\times10^{-3}$	236

Table 1. A list of K^+ decay modes (from the Review of Particle Properties)

1.2 The Standard Model

The modern theory of electromagnetic and weak interactions, more commonly referred to as the "The Standard Model", is undeniably one of the great achievements of modern theoretical physics. The prediction and subsequent experimental observation of the intermediate vector bosons ($W^\pm, Z$) is perhaps its most celebrated success, but is by no means the only one. The theory successfully combines the weak and electromagnetic interactions in a renormalizable way, removing diver-

gences that had previously ruled out second and higher order calculations.

Before proceeding with a discussion of the calculations relevant to this thesis, we will briefly review the $V - A$ interaction and GIM supression.

1.2.1 The $V - A$ interaction

Motivated by the need for a relativistically invariant theory, Dirac and others sought to formulate an equation of motion that treated the spatial and temporal coordinates on an equal footing.* The Klein-Gordon equation was quadratic in both derivatives making it relativistically invariant, but failed to account for the two-component nature of spin 1/2 particles. It did however allow the existence of states having negative probability densities, which are now understood in terms of antiparticles.

Wishing to remove these negative solutions, Dirac (in 1928) formulated an equation of motion *linear* in derivatives. The resulting *Dirac equation* is arguably one of the most important theoretical tools conceived in the twentieth century[9].

In convenient notation, this equation can be written:

$$i(\gamma^\mu \partial_\mu - m)\psi = 0 \tag{1.1}$$

Where γ^μ are Dirac 4×4 γ-matrices and ψ is a 4-component wave function.

The only unique Lorentz covariant interactions that can be constructed using the γ matrices are the following:

Scalar	$\overline{\psi}\psi$
Vector	$\overline{\psi}\gamma^\mu\psi$
Tensor	$\overline{\psi}\sigma^{\mu\nu}\psi$
Pseudoscalar	$\overline{\psi}\gamma^5\psi$
Axial Vector	$\overline{\psi}\gamma^5\gamma^\mu\psi$

(1.2)

Where $\gamma^5 \equiv i\gamma^0\gamma^1\gamma^2\gamma^3$ and

* The Schrodinger equation was *not* Lorentz invariant since it was linear in $\partial/\partial t$ and quadratic in $\partial/\partial x$

$$\sigma^{\mu\nu} = \frac{i}{2}(\gamma^\mu\gamma^\nu - \gamma^\nu\gamma^\mu) \tag{1.3}$$

In 1958, Feynman and Gell-Mann proposed that all charged weak interactions can be described by an effective Lagrangian density[10]:

$$\mathcal{L} = -\frac{1}{2}\frac{G_F}{\sqrt{2}}(\mathcal{J}_\nu\mathcal{J}^{\nu\dagger} + \mathcal{J}^{\nu\dagger}\mathcal{J}_\nu) \tag{1.4}$$

Where $\mathcal{J}_\nu$ is a universal charged weak current containing both leptonic and hadronic contributions (j and J respectively):

$$\mathcal{J}^\nu = j^\nu + J^\nu \tag{1.5}$$

The leptonic part of the current was experimentally found to have the form:

$$j^\nu = (\nu_e\,,\,\nu_\mu\,,\,\nu_\tau)\gamma^\nu\frac{(1-\gamma^5)}{2}\begin{pmatrix} e \\ \mu \\ \tau \end{pmatrix} \tag{1.6}$$

The $\gamma^\nu(1-\gamma^5)$ factor is a linear combination of the *vector* and *axial vector* terms from (1.2), and accounts for the name of the "$V-A$" interaction. This form of interaction is guaranteed to violate parity, since $\frac{1}{2}(1-\gamma^5)$ is the helicity projection operator.

1.2.2 The GIM Mechanism

The above leptonic current, by definition, does *not* mix the different lepton generations. This is consistent with the experimental observation that individual lepton number seems to be an exactly conserved quantum number.

Shown below are the three lepton and three quark generations containing the fundamental fermions.

$$\begin{pmatrix} \nu_e \\ e \end{pmatrix} \quad \begin{pmatrix} \nu_\mu \\ \mu \end{pmatrix} \quad \begin{pmatrix} \nu_\tau \\ \tau \end{pmatrix} \quad \begin{pmatrix} u \\ d \end{pmatrix} \quad \begin{pmatrix} c \\ s \end{pmatrix} \quad \begin{pmatrix} t \\ b \end{pmatrix} \tag{1.7}$$

The idea of interactions being confined within generations is aesthetically pleasing, and it would be nice if this carried over into the quark sector. With the above

definition of the quark doublets, however, we see that interactions do *not* stay within generation boundaries. A case in point is the $K^+ \rightarrow \mu^+\nu$ decay in which the hadronic current is clearly connecting an s quark and a u quark (see Fig. 1).

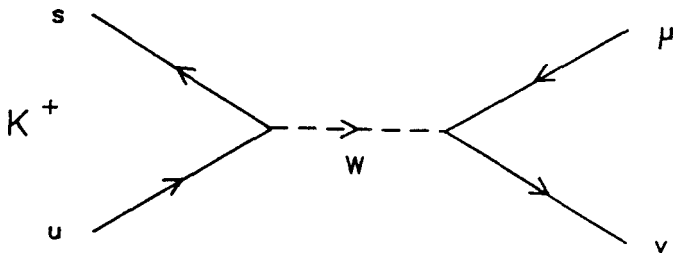

Figure 1. Feynman diagram for the $K^+ \rightarrow \mu^+\nu$ decay mode. The charged weak current changes an s quark into a u quark.

We can reconcile the observed quark mixing with our wish for generation conservation by redefining the quark doublets. This is analogous to a co-ordinate transformation in that we "rotate" to a new weak eigenstate basis using a unitary matrix M.

Specifically:

$$\begin{pmatrix} u \\ d \end{pmatrix}, \begin{pmatrix} c \\ s \end{pmatrix}, \begin{pmatrix} t \\ b \end{pmatrix} \longrightarrow \begin{pmatrix} u \\ d_c \end{pmatrix}, \begin{pmatrix} c \\ s_c \end{pmatrix}, \begin{pmatrix} t \\ b_c \end{pmatrix} \tag{1.8}$$

Where

$$\begin{pmatrix} d_c \\ s_c \\ b_c \end{pmatrix} = \mathrm{M} \begin{pmatrix} d \\ s \\ b \end{pmatrix} \tag{1.9}$$

and M is a 3×3 unitary matrix with 4 free parameters, as proposed by Kobayashi and Maskawa[11].

With this redefinition of the quark doublets, charged interactions do *not* mix generations, (u connects only to d_c etc). This is not surprising since by definition d_c contains bits of s and b as well as d.

We can now write down the form of the hadronic charged weak current in analogy with (1.6):

$$J^\nu = (\bar{u}\,,\,\bar{c}\,,\,\bar{t})\gamma^\nu \frac{(1-\gamma^5)}{2} \begin{pmatrix} d_c \\ s_c \\ b_c \end{pmatrix} \tag{1.10}$$

The above formalism was constructed in such a way that hadronic charged weak currents would not mix the "rotated" doublets. As a bonus we find that neutral currents are similarly constrained in that they will not connect different quark flavors. This is simply a manifestation of the fact that the K-M matrix is unitary:

$$(\bar{d}_c, \bar{s}_c, \bar{b}_c) \begin{pmatrix} d_c \\ s_c \\ b_c \end{pmatrix} = (\bar{d}, \bar{s}, \bar{b})\, \mathrm{M}^\dagger \mathrm{M} \begin{pmatrix} d \\ s \\ b \end{pmatrix} = (\bar{d}, \bar{s}, \bar{b}) \begin{pmatrix} d \\ s \\ b \end{pmatrix} \tag{1.11}$$

Since $\mathrm{M}^\dagger\mathrm{M} = \mathrm{I}$ by unitarity.

This is known as the GIM mechanism, and was first used to explain the puzzling experimental absence of strangeness changing weak neutral currents.

1.3 Calculations relevant to $K^+ \to \pi^+\mu^+\mu^-$

It is the GIM mechanism that allows us to probe the standard model to second order, since the first order *weak* processes for both $K^+ \to \pi^+\mu^+\mu^-$ and $K^+ \to \pi^+\nu\overline{\nu}$ are strictly forbidden, (as they would involve flavor changing weak neutral currents). Measurement of the $K^+ \to \pi^+\mu^+\mu^-$ branching ratio, however, will *not* enable us to draw conclusions regarding second order weak effects per se, since these do not contribute significantly to the final rate, as shown below.

Fig. 2(a) and (b) shows the leading diagrams contributing to the decay $K^+ \to \pi^+\nu\overline{\nu}$. The "box" diagram shows the exchange of two W's, and the other represents the *induced* dsZ coupling.

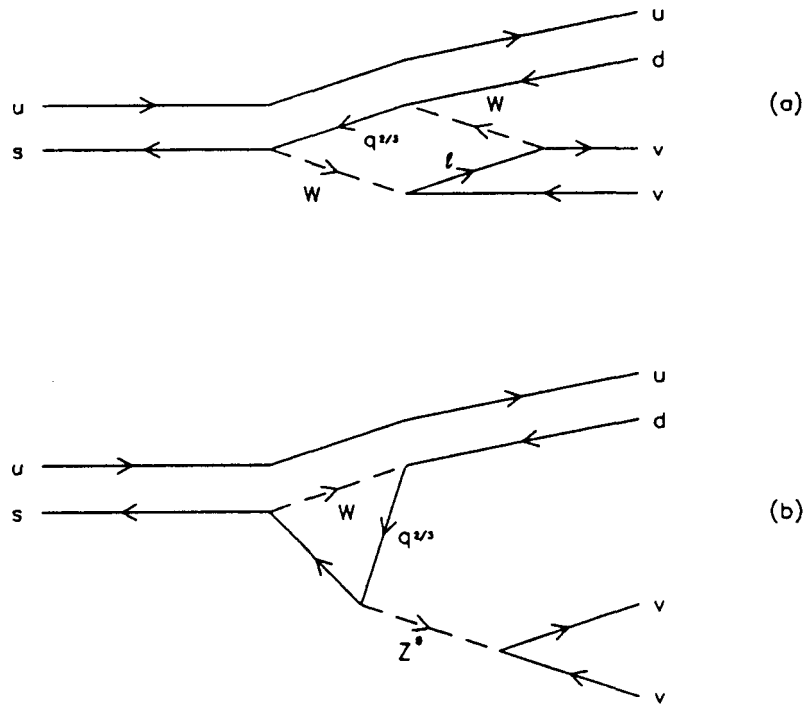

Figure 2. The leading diagrams contributing to $K^+ \to \pi^+\nu\bar{\nu}$. l can be any charged lepton and $q^{\frac{2}{3}}$ is any charge 2/3 quark.

The purely weak contribution to $K^+ \to \pi^+\mu^+\mu^-$ can be obtained from Fig. 2 by replacing external ν lines by μ's, and the internal lepton line in the box diagram by a ν.

There is a third contribution, however, that will dominate the other two: since the final state leptons in $K^+ \to \pi^+\mu^+\mu^-$ are charged, the Z in Fig. 2 can be replaced by a γ, representing a "long range" electromagnetic contribution. This is shown in Fig. 3. We would expect this induced $ds\gamma$ term to be relatively large, having an amplitude of order $G_F\alpha$ while the other purely weak diagrams should have amplitudes of order G_F^2.

An order of magnitude estimate of the contribution to the $\pi\mu\mu$ rate from the first two diagrams can be obtained by considering calculations done for the rate of $K^+ \to \pi^+\nu\bar{\nu}$.

Calculations of the $K^+ \to \pi^+\nu\bar{\nu}$ rate can be done quite accurately since the result can be expressed in terms of another rate which has been well measured[12,13].

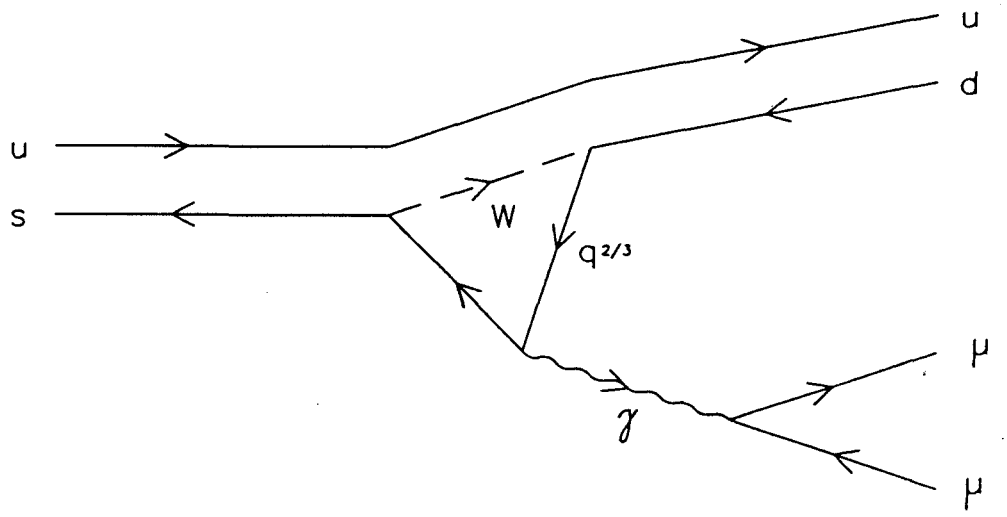

Figure 3. The leading diagram contributing to $K^+ \to \pi^+\mu^+\mu^-$. l can be any charged lepton and $q^{\frac{2}{3}}$ is any charge 2/3 quark. This diagram dominates the purely second order weak contributions because of its electromagnetic nature.

$$\frac{B(K^+ \to \pi^+\nu\bar{\nu})}{B(K^+ \to \pi^0 e^+\nu)} = 2 \cdot \left(\frac{\alpha}{4\pi sin^2\theta_W}\right)^2 \cdot \frac{\left|\tilde{\mathrm{D}}_i\right|^2}{V_{us}^2} \tag{1.12}$$

Technically, the two processes are related by an isospin rotation. Expressing the result as a ratio in this way removes large uncertainties associated with the hadronic wavefunctions. The accuracy of the predicted result is as good as the knowledge of the relevant parameters in the K-M matrix.

$$B(K^+ \to \pi^+\nu_i\bar{\nu}_i) = (0.61 \times 10^{-6}) \cdot \frac{\left|\tilde{\mathrm{D}}_i\right|^2}{V_{us}^2} \tag{1.13}$$

Where:

$$\tilde{\mathrm{D}}_i = \sum_{j=c,t} V_{js}^* V_{jd} \overline{\mathrm{D}}(x_j, y_i) \tag{1.14}$$

and $\overline{\mathrm{D}}(x_j, y_i)$ is a function only of the quark and lepton masses since

$$x_j = \frac{m_{q_j}^2}{m_W^2}, \quad y_i = \frac{m_{l_i}^2}{m_W^2} \tag{1.15}$$

The V's are the mixing parameters of the K-M matrix:

$$\mathrm{M} = \begin{pmatrix} V_{ud} & V_{us} & V_{ub} \\ V_{cd} & V_{cs} & V_{cb} \\ V_{td} & V_{ts} & V_{tb} \end{pmatrix} \tag{1.16}$$

where, for example, V_{ud} describes the $u \leftrightarrow d$ coupling.

It is interesting to note that $\overline{\mathrm{D}}(x_t, y) >> \overline{\mathrm{D}}(x_c, y)$, hence top quark couplings dominate the rate for $K^+ \rightarrow \pi^+ \nu\overline{\nu}$, indeed the rate depends rather strongly on the mass of the t quark.

Using the most favorable estimates of the standard model (K-M) parameters, the branching ratio for $K^+ \rightarrow \pi^+ \nu\overline{\nu}$ is still comes out below 10^{-9}.

One would expect the purely weak contribution to $K^+ \rightarrow \pi^+ \mu^+ \mu^-$ to be similarly small, leaving the induced $ds\gamma$ term dominant. This term is unfortunately difficult to calculate, although several attempts have been made. A recent calculation using chiral perturbation theory[14] has placed the branching ratio at:

$$BR(K^+ \rightarrow \pi^+ \mu^+ \mu^-) = (3.7 \rightarrow 7.2) \times 10^{-8} \tag{1.17}$$

The above number was obtained only after the value of an unknown renormalization constant was deduced by comparing a similar calculation for $K^+ \rightarrow \pi^+ e^+ e^-$ with experimental results.

There is a more pedestrian approach which will yield the same result. The leading order diagram for the process $K^+ \rightarrow \pi^+ e^+ e^-$ will be the same as for $\pi\mu\mu$, with the μ line in Fig. 3 replaced by an e. If one assumes that the electron and muon couple in the same way to the photon propagator,* then the ratio of the rates

* This assumption is known as $e - \mu$ universality, and is well established for charged current weak and electromagnetic interactions.

Coupling	V	A	S	P	T	PT
R	5.1	2.0	4.5	2.0	1.4	8.3

Table 2. Table of R vs lepton coupling assuming $e-\mu$ universality[15].

$(K^+ \to \pi^+e^+e^-)/(K^+ \to \pi^+\mu^+\mu^-)$ will be determined entirely by kinematics. This ratio R has been calculated assuming various coupling schemes[15], and the results are shown in Table 2.

If we assume the coupling is Vector in nature, the ratio of rates is;

$$\frac{BR(K^+ \to \pi^+e^+e^-)}{BR(K^+ \to \pi^+\mu^+\mu^-)} = 5.1 \tag{1.18}$$

From the measured value of $BR(K^+ \to \pi^+e^+e^-) = (2.7 \pm 0.5) \times 10^{-7}$ we can solve for the $K^+ \to \pi^+\mu^+\mu^-$ rate:

$$BR(K^+ \to \pi^+\mu^+\mu^-) = (5.3 \pm 1) \times 10^{-8} \tag{1.19}$$

We see that this gives essentially the same result as the chiral perturbation calculations.

It is apparent from Table 2 that a good measurement of the ratio R can determine the form of the coupling itself, which is of fundamental interest. Also pointed out by Beder and Dass[15], is the possibility of discovering the existence of genuine strangeness-changing semi-leptonic neutral currents by carefully studying the decays modes $K^+ \to \pi^+\mu^+\mu^-$ and $K^+ \to \pi^+e^+e^-$.

There is an additional point that should be made supporting the validity of calculations done using chiral perturbation theory. In this formalism, the virtual process $K^+ \to \pi^+\gamma(q)$ is forbidden to lowest order for all values of q^2, hence one might expect a supression of $K^+ \to \pi^+\mu^+\mu^-$ and $K^+ \to \pi^+e^+e^-$ relative to other rates[14]. Indeed, if we consider the ratio

$$\frac{BR(K^+ \to \pi^+e^+e^-)}{BR(K^+ \to \pi^0e^+\nu)} = (5.6 \pm 1.1) \times 10^{-6} \tag{1.20}$$

we see that it is an order of magnitude smaller than a single factor of α^2 can account for, indicating the presence of additional supression. (The naive guess that the ratio should be of order α^2 comes from counting the number of weak and electromagnetic

vertices in each: $K^+ \to \pi^+ e^+ e^-$, having a W propagator and a γ propagator, should have an amplitude of order $G_F \alpha$, and $K^+ \to \pi^0 e^+ \nu$, having only a W propagator, should have an amplitude of order G_F).

We see that two different theoretical methods of determining the $K^+ \to \pi^+ \mu^+ \mu^-$ branching ratio yield essentially the same result, although both suffer from having to rely on the experimental measurement of $K^+ \to \pi^+ e^+ e^-$ to determine unknown factors. This not only gives us a calculated number to use as a reference, but indicates that an accurate determination of the $K^+ \to \pi^+ \mu^+ \mu^-$ branching ratio may be a good hunting ground for new physics.

Before this writing, the experimental status in regard to $K^+ \to \pi^+ \mu^+ \mu^-$ was that no events had been observed; an upper limit on its branching ratio having been set at $\leq 2.4 \times 10^{-6}$ by bubble chamber experiments [16,17].

1.4 Setting limits on a light Higgs boson

The concept of *gauge invariance* is the underlying theme of modern field theory. Demanding local $U(1)$ gauge invariance leads to the celebrated QED Lagrangian, and the analogous construction on the group $SU(3)$ results in the non-Abelian theory of QCD. The Lagrangian of QED (QCD) demands the the photon (gluon) have zero mass, since the addition of a mass term would spoil its gauge invariance. This feature turns out to be a problem when one tries to write down a gauge invariant Lagrangian to describe the weak interactions, since the exchange bosons are known to be massive.

This problem is neatly solved by writing the Lagrangian in such a way as to permit *spontaneous symmetry breaking*. This allows the Lagrangian to retain its symmetry properties, which are essential for renormalizability, while admitting massive exchange quanta. These benefits are gained at the expense of introducing a new scalar field of undetermined mass: the *Higgs* field. A complete discussion of this formalism is beyond the scope of this introduction, and can be found in [1].

An interesting feature of the Higgs is that it couples to fermions with an amplitude proportional to the mass of the fermion, hence it will prefer to decay to the heaviest kinematically allowed particles. Specifically, for $2m_\mu \geq M_H \geq 2m_\pi$, the decay $H \to \mu^+ \mu^-$ dominates. Fig. 4 shows the tree level (a) and one loop (b) contributions to the decay $K^+ \to \pi^+ H$.

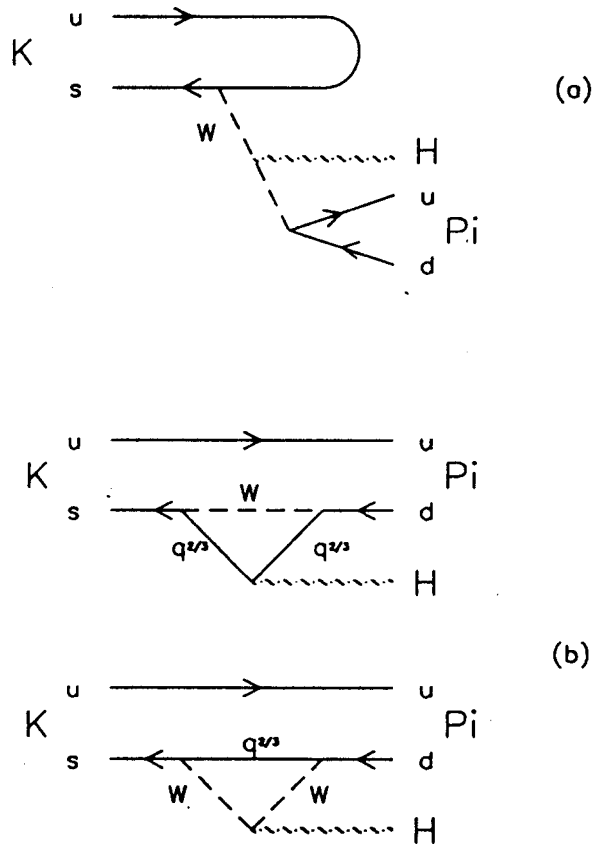

Figure 4. The tree level (a) and one loop (b) contributions to $K^+ \to \pi^+ H$.

Prior to this writing, the best upper limit on the decay mode $K^+ \to \pi^+ H$ in the mass range $2m_\mu \geq M_H \geq 2m_\pi$ was $\mathrm{BR}(K^+ \to \pi^+ H) \leq 4 \times 10^{-5}$[18].

Although the theoretical interpretation of $K^+ \to \pi^+ H$ results varies, the above limit can *not* be used to unambiguously rule out the existence of a Higgs like boson in the stated mass range[19,20].

Other experiments examining the decays of B and Υ mesons have been used to exclude the existence of a Higgs boson with mass $2m_\mu \geq M_H \geq 7\mathrm{GeV}$, at the 90% confidence level[20,19].

1.5 THE DECAY MODE $K^+ \to \mu^+\nu\mu^+\mu^-$

This is interesting primarily because there is no previous limit on its observation listed by the Particle Data Group. A possible diagram for this decay is shown in Fig. 5.

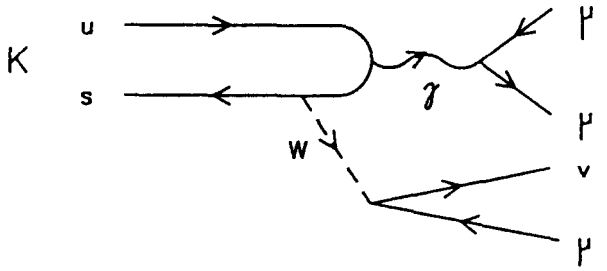

Figure 5. A possible diagram for $K^+ \to \mu^+\nu\mu^+\mu^-$.

A similar decay mode, $K^+ \to \mu^+\nu e^+e^-$, has been observed experimentally[21] with a branching ratio of $\mathrm{BR}(K^+ \to \mu^+\nu e^+e^-) = (1.1 \pm 0.3) \times 10^{-6}$. Since the diagram for $K^+ \to \mu^+\nu e^+e^-$ is the same as for $K^+ \to \mu^+\nu\mu^+\mu^-$, with the γ creating a pair of electrons rather than a pair of muons, we should be able to estimate $\mathrm{BR}(K^+ \to \mu^+\nu\mu^+\mu^-)$ by scaling $\mathrm{BR}(K^+ \to \mu^+\nu e^+e^-)$ by an appropriate phase-space factor.

A rough upper limit of this phase-space factor can be obtained by considering the ratio:

$$\frac{BR(K_L^0 \to \gamma\mu^+\mu^-)}{BR(K_L^0 \to \gamma e^+e^-)} \sim 1/60$$

Hence, we would expect that

$$BR(K^+ \to \mu^+\nu\mu^+\mu^-) \leq 1.8 \times 10^{-8}$$

The decay mode $K^+ \to \mu^+\nu\mu^+\mu^-$ is also intriguing because it represents another possible Higgs channel: $K^+ \to \mu^+\nu H$, $H \to \mu^+\mu^-$. The branching ratio for $K^+ \to \mu^+\nu H$, and the similar process $K^+ \to e^+\nu H$, can be calculated exactly to first order in chiral perturbation theory[22]. Unfortunately, the expected rate is $< 4 \times 10^{-8}$, well below our sensitivity for $K^+ \to \mu^+\nu\mu^+\mu^-$.

2. The Detector

2.1 Introduction

The E787 detector was designed primarily to search for the 2^{nd} order weak decay $K^+ \to \pi^+\nu\bar{\nu}$. The design philosophy was to maximize the geometrical acceptance by building a "4π" detector. The concept is very similar to that of colliding beam experiments in that the interactions of interest happen in the lab rest frame, and the detector is designed to subtend as much solid angle as possible around the interaction region.

In the case of the E787 detector, this "interaction region" is a segmented scintillator target, and the events under study are due to a beam of K^+'s which stop and decay in this target.

The topic of this thesis is *not* the hunt for $K^+ \to \pi^+\nu\bar{\nu}$, instead it deals with the search for another second order process: $K^+ \to \pi^+\mu^+\mu^-$. Although the detector was not designed specifically for this, it is surprisingly well suited for the task. In order to understand and appreciate the detector, however, it is most illuminating to present its description in the context of $K^+ \to \pi^+\nu\bar{\nu}$, since it is the properties of this decay mode that guided its design.

The two most important ingredients for a successful search for $K^+ \to \pi^+\nu\bar{\nu}$ are:

(*i*) The ability to unambiguously identify π^+'s.

(*ii*) The ability so say with certainty whether or not a given event had γ's associated with it.

In order to illustrate how these goals are achieved by the E787 detector, we will consider the case of a typical K^+ entering the detector.

Fig. 6 is a detailed perspective drawing of the entire detector assembly, and Fig. 7 shows a sketched cross-sectional view. These pictures may be useful in understanding the introduction presented below.

The K^+ encounters the first detector element immediately after passing through the final beamline quadrupole Q6. The beam instrumentation is located between Q6 and the central stopping target, and consists of a set of scintillators, a three plane multi wire proportional chamber (MWPC), a Čerenkov counter and an energy degrader. The Čerenkov counter is designed to distinguish between K's and π's. (This is crucial to the experiment since a scattered π can appear exactly like a $K^+ \rightarrow \pi^+\nu\bar{\nu}$ event). The scintillation counters are distributed in such a way as to form a telescope for the stopping kaons which points into the target, and the MWPC is needed offline to flag events where more than one beam particle entered the target during the ADC gate. The degrader slows the 750 MeV/c kaons to the extent that they will stop, on average, in the center of the target.*

The stopping target is composed of 379 scintillator elements arranged in a hexagonal array. After the K^+ stops, it will decay with a mean life of 12.4 ns. For the sake of illustration, let's assume the decay mode is $K^+ \rightarrow \pi^+\pi^0$, and that the π^+ leaves the target in any direction other than parallel to its axis. This sequence of events will leave a unique signature in the target, as seen in Fig. 8, a target event display showing ADC's and TDC's for a typical $K^+ \rightarrow \pi^+\pi^0$ event. The elements in which the K^+ stopped show very high deposited energies, while the elements hit by the secondary π^+ reflect only small energy depositions. The TDC's confirm this interpretation, indicating that the K^+ energy was deposited at $t = 0$, and that the π^+ hits happened at a later time.

The π^0 from the $K^+ \rightarrow \pi^+\pi^0$ decay will decay immediately, having a lifetime of 10^{-16} seconds. It is of utmost importance that at least one of the two resulting γ's be identified, lest the event be misidentified as $K^+ \rightarrow \pi^+\nu\bar{\nu}$. Examining Fig. 7 we see that the ***barrel veto*** together with the ***endcap veto*** effectively seal the detector against photon leakage. The only region not covered by by these systems is a cylindrical section of small diameter, concentric with the beam axis. This is not a problem, however, since the solid angle this presents is very small and a Monte Carlo study has shown that $K^+ \rightarrow \pi^+\pi^0$ decays where a high energy γ escapes via this route will not have the associated π^+ enter the fiducial region of the range stack.

If the initial K^+ had decayed via $K^+ \rightarrow \mu^+\nu$ rather that $K^+ \rightarrow \pi^+\pi^0$, there would be no γ's available to veto the event, and we would have to rely on other

* Only about 1/4 of the kaons which enter the degrader will come to rest in the target. The biggest loss factor, ~ 2, is due to nuclear interactions in the degrader, with other sizable losses arising from in-flight decays and scattering.

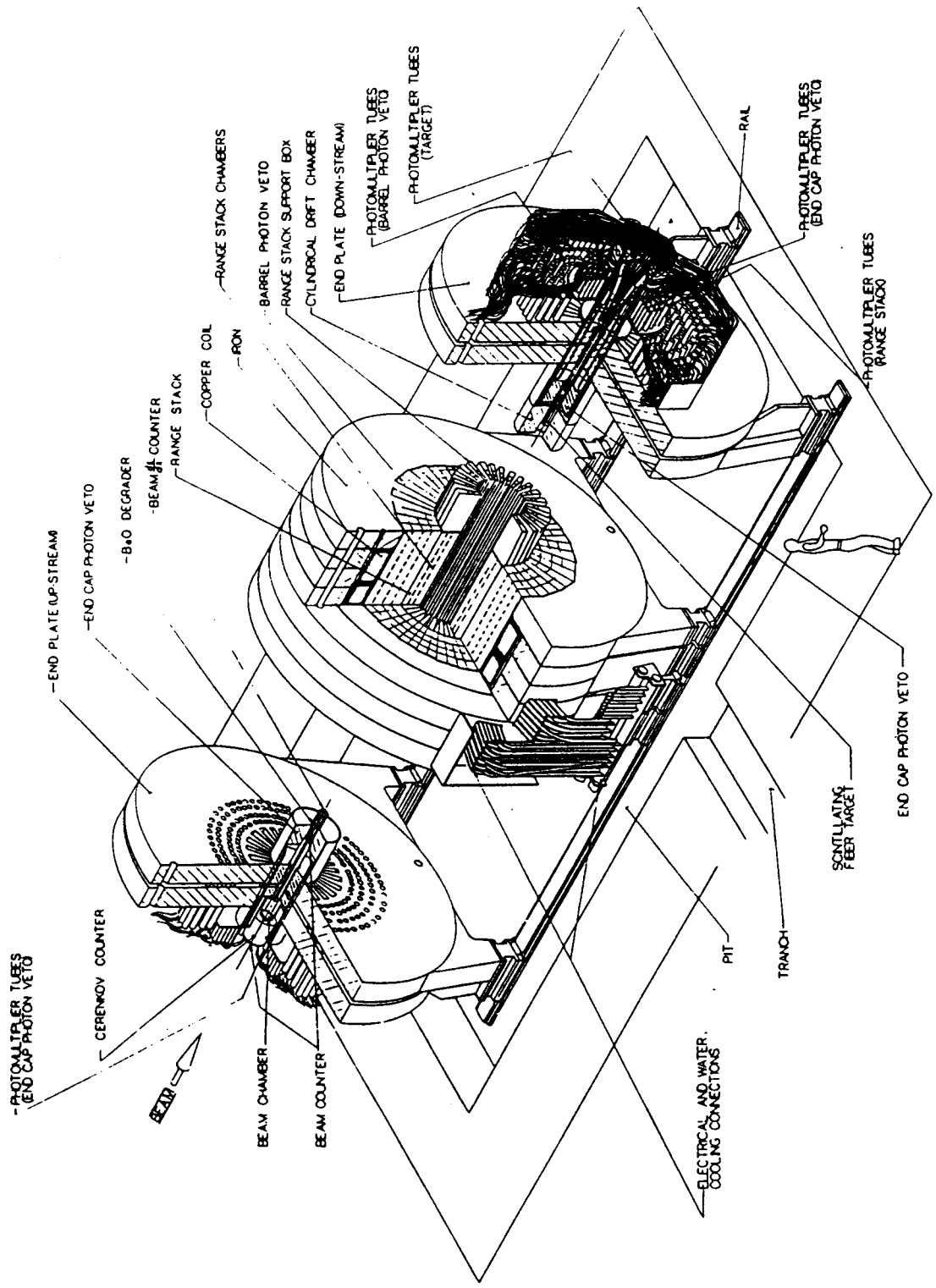

Figure 6. A perspective drawing showing the entire detector assembly. In this representation the magnet is in its open position, and portions have been cut away to display what is inside.

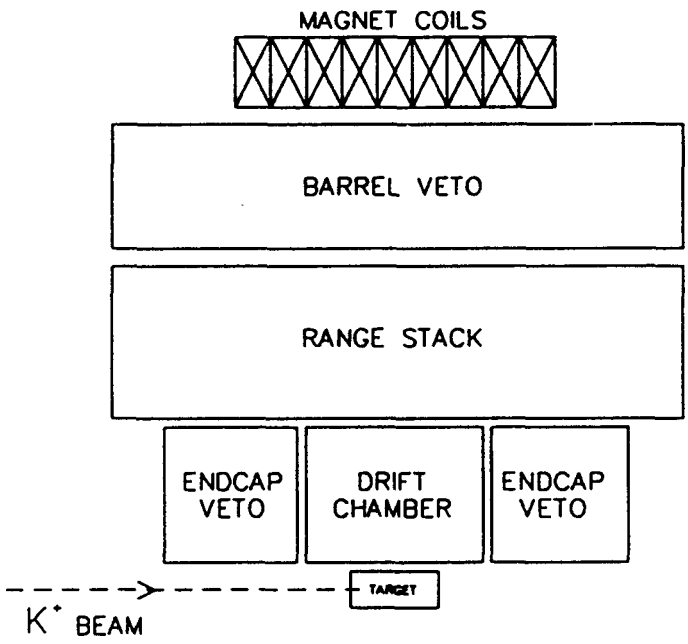

Figure 7. Cross-sectional sketch of E787 detector showing the solenoid, target, drift chamber, range stack, barrel veto and endcap subsystems. The detector has azimuthal symmetry, and only the "top" half is shown.

aspects of the detector to keep us from mistakenly identifying the μ^+ as a π^+(which would again make the event look like $K^+ \to \pi^+\nu\bar{\nu}$).

There are two main weapons available for this job. The first is the ability to measure the *momentum*, the *range*, and the total *energy* of the particle. These three quantities can be deduced by combining information obtained from the drift chamber, the range stack, and the target.

The range stack is, as the name implies, a stack of scintillator sheets. They are arranged in twenty four azimuthal *sectors* subtending 2π of the total solid angle seen by a K^+ at the center of the target. Each sector also contains two MWPC's, which are used to determine track positions. The radial segmentation of the range stack combined with MWPC and drift chamber z-slope information allows a precise

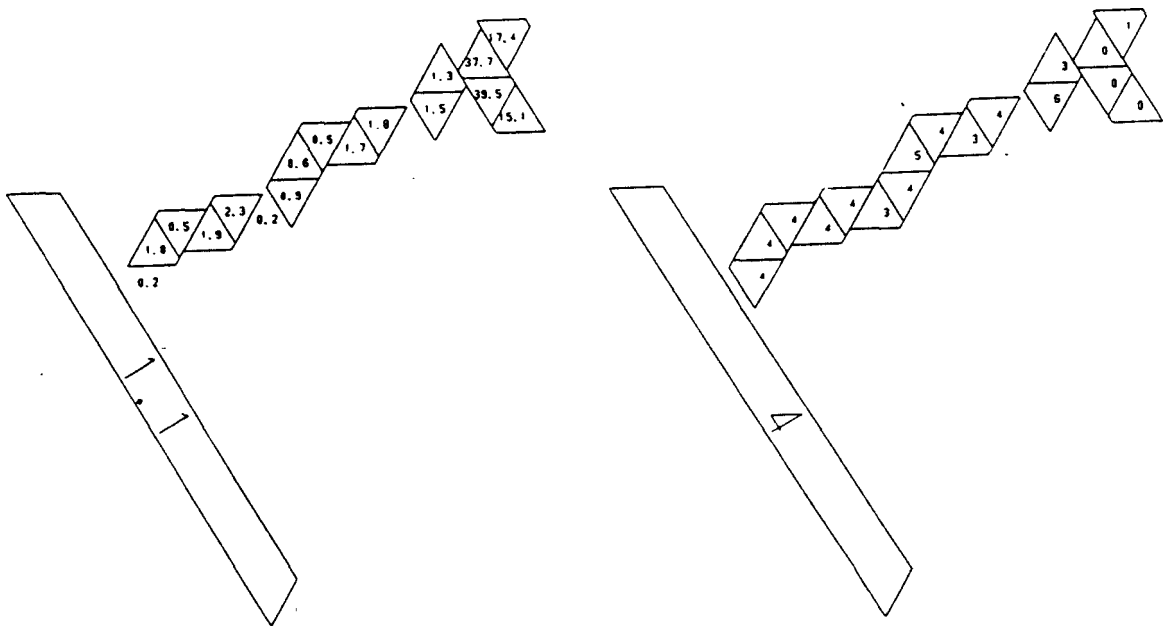

Figure 8. Target event display for a typical $K^+ \rightarrow \pi^+\pi^0$ event showing ADC's (left) and TDC's (right). The target elements are triangular, and the large outline represents one of the I-counters surrounding the target. The elements in which the K^+ stopped show a large energy deposition at early times, to be contrasted with the lightly ionizing π^+ track seen leaving the target about 4 ns later.

measurement of a particle's range. (The range in the target must also be included in the *total* range measurement).

The total energy is obtained by looking at the range stack and target ADC's, and the momentum is measured by the central drift chamber.*

The power of this technique to distinguish $K_{\pi 2}$'s from $K_{\mu 2}$'s is illustrated in Fig. 9 which is a scatter plot of momentum *vs* range for a mixed sample of $K^+ \rightarrow \pi^+\pi^0$ and $K^+ \rightarrow \mu^+\nu$ events. The muon and pion "blobs" are well separated.

The second weapon against muon misidentification is the system of 100 transient recorders which instrument the π^+ stopping region of the range stack, allowing us to measure the actual pulse shapes from each of these phototubes. This ability allows us to demand that any π^+ candidate exhibit the characteristic decay sequence

* The entire detector is contained within a solenoid providing a uniform 10 kG axial field.

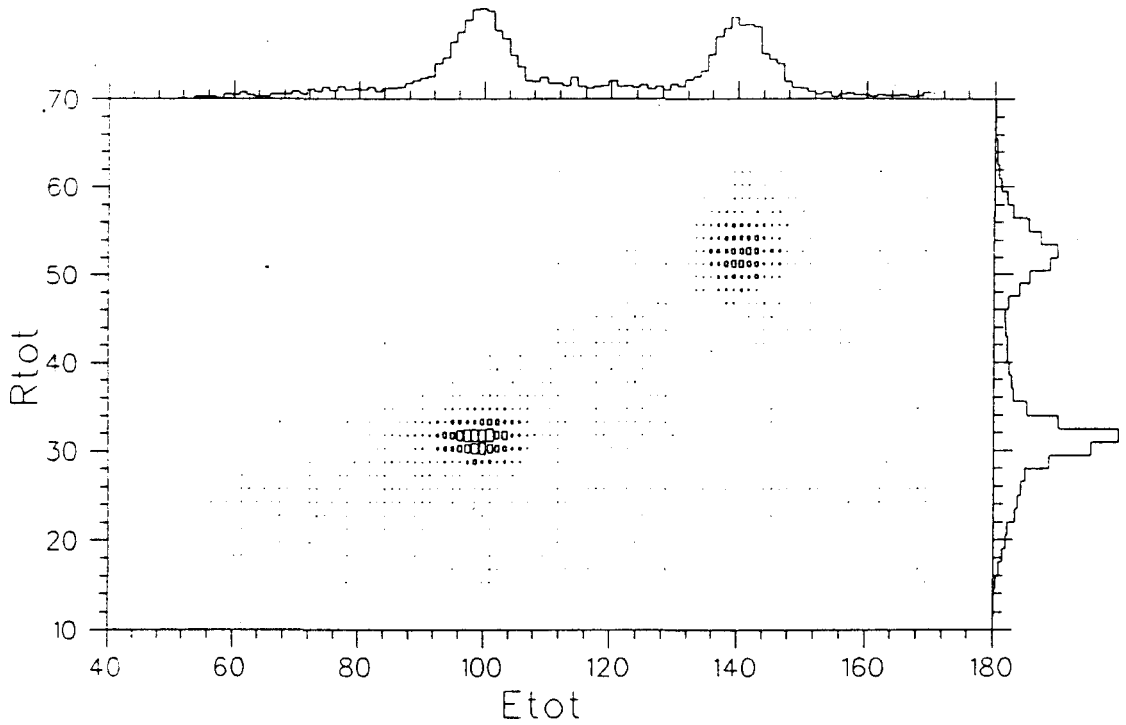

Figure 9. A plot of Energy *vs* Range for a mixed sample of $K^+ \to \pi^+\pi^0$ and $K^+ \to \mu^+\nu$ events. Notice the obvious separation between the two clusters of data representing μ^+'s and π^+'s.

$\pi \to \mu \to e$, which would *not* be seen for a muon. A sketch of this decay sequence is shown in Fig. 10.

From the above description it is clear that the E787 detector is exceptionally well suited for detecting $K^+ \to \pi^+\nu\bar{\nu}$ events: The γ veto coverage is effectively 4π and there are several powerful techniques for distinguishing π's from μ's.

The above description is only a brief and simplified outline of some of the components; in reality most of the subsystems perform more that one vital function. For instance, the range stack and target are also both used as γ detectors.

A more comprehensive description of each subsystem is presented below. The reader may find it useful to refer to Fig. 11, which is a detailed version of Fig. 7 previously presented.

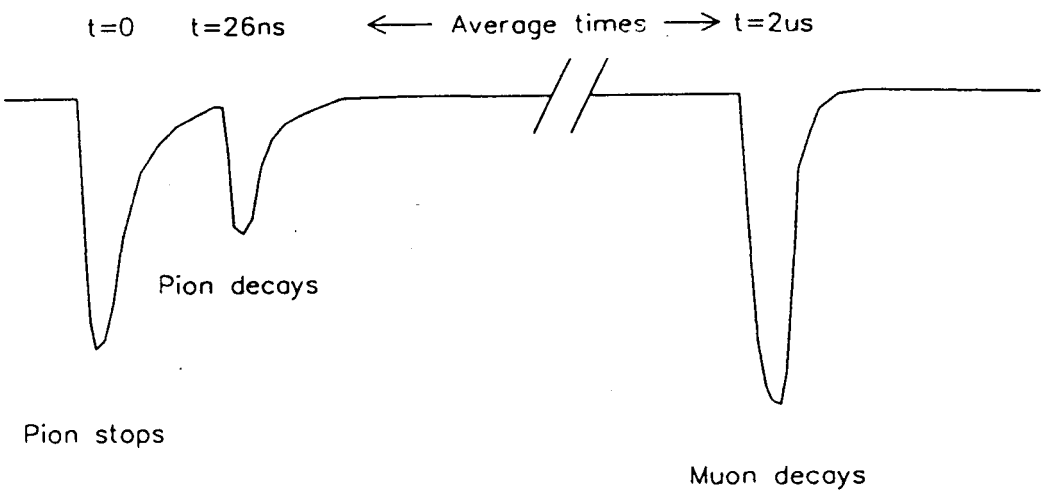

Figure 10. A typical sequence of events as captured by the transient recorders: The π^+ comes to rest in the range stack depositing the initial large pulse. This is followed (on average) 26 ns later by a smaller 4 MeV pulse from the $\pi^+ \rightarrow \mu^+$ decay, and finally the $\mu^+ \rightarrow e^+$ can be seen $\sim 2\mu$s later.

2.2 The Magnet

Basic Parameters:

Central field	1 Tesla
Voltage	263 Volts
Current	4126 Amps
Power	1.09 MW
Number of coils	18
Turns per coil	22
Coil thickness	8.1 cm

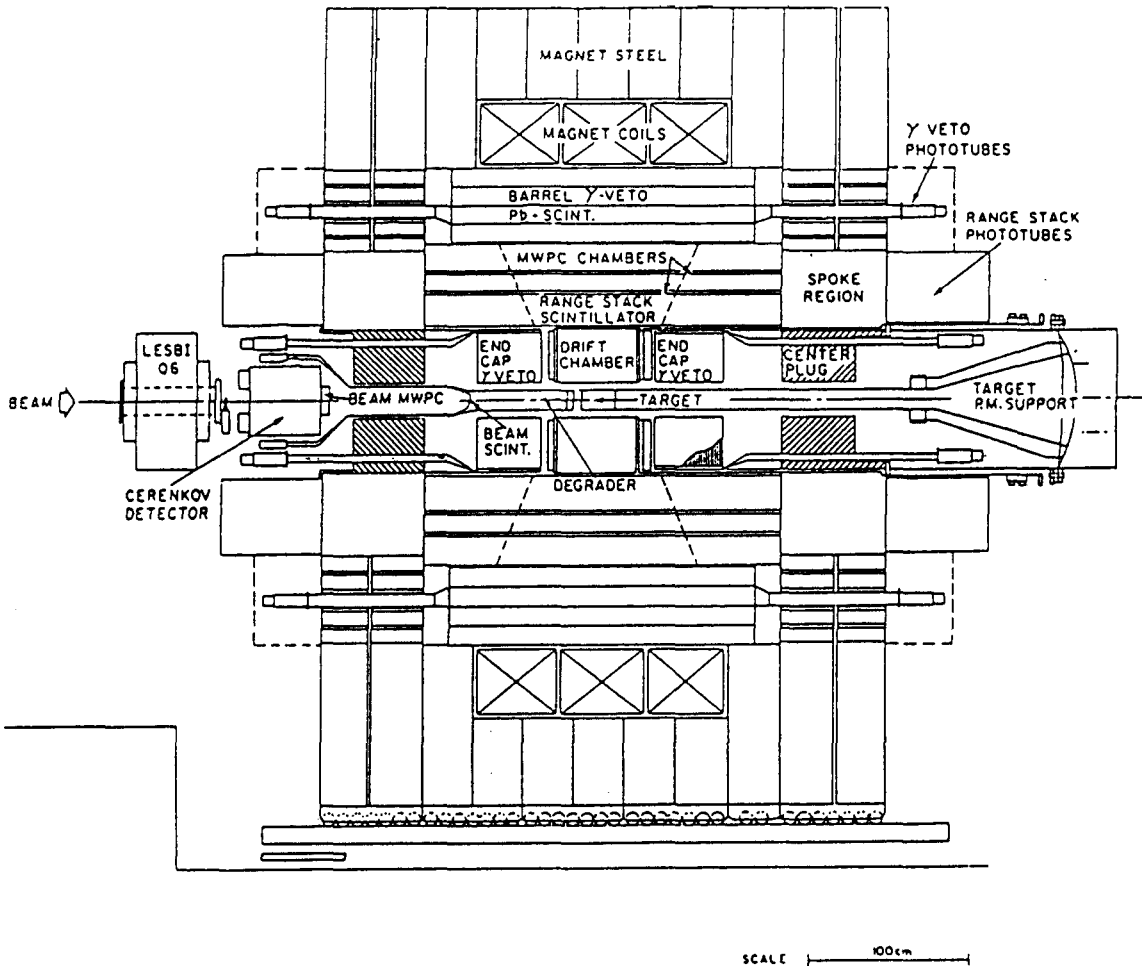

Figure 11. A scale cross sectional view of the detector showing each of the sub-systems in detail.

Coil inside diameter	296 cm
Cu conductor cross section	3.85 cm × 3.52 cm with 1.58 cm central hole
Overall outside diameter	500 cm
Overall length	352 cm
Inside length	221 cm
Iron yoke thickness	56 cm
End plate thickness	30 cm + (2.5 cm gap) + 32 cm

Total iron weight	365 Tons
Total copper weight	47 Tons

The E787 magnet is a large water-cooled copper device, whose usable field volume is a cylinder 222 cm long with a radius of 146 cm [23]. The current carrying element of the solenoid is an assembly of 18 coil "pancakes", each containing one electrical and two water cooling circuits. Fig. 12 is a photograph showing one of the pancakes being lifted into place during the assembly of the central magnet section. The support structure and flux return is constructed of iron salvaged from the SREL cyclotron, which was flame cut and welded to form the central cylindrical section and the two end plates.

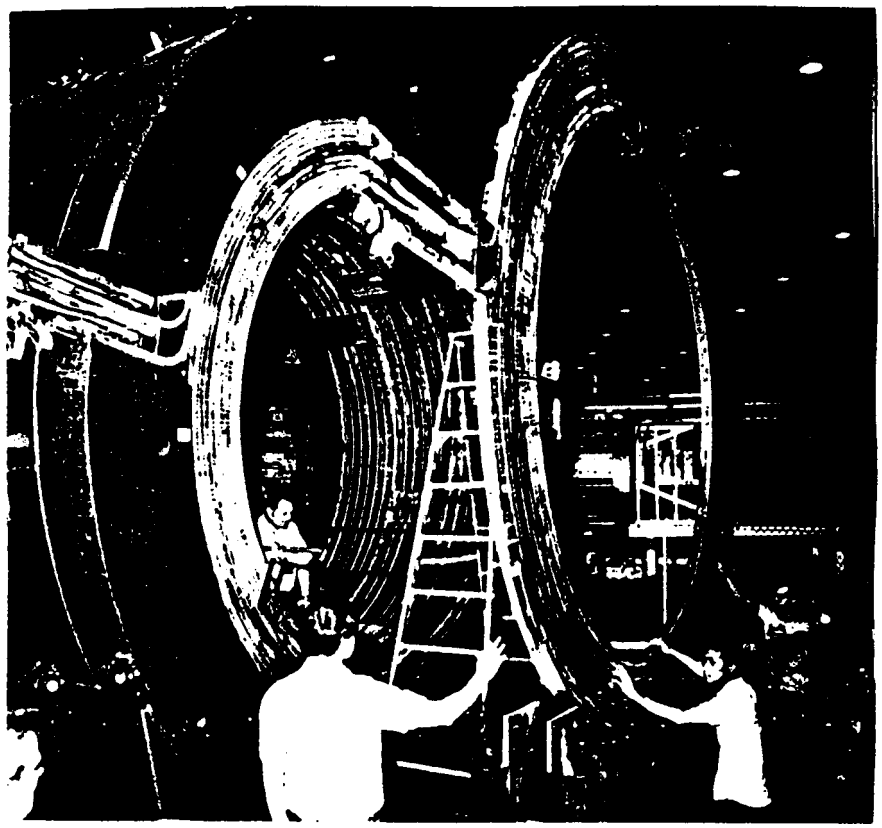

Figure 12. Photo of one of the coils being lifted into the central magnet assembly.

Fig. 13 is a photo of the central magnet section before the downstream (left) endplate was rigged into position. Both endplates are identical, each having a

central "hole" into which the cylindrical drift chamber, target, beam elements and end-caps are inserted. This is radially followed by a slotted region covering the range-stack. In this area, twenty four iron spokes provide structural support and flux confinement while leaving gaps through which the range-stack light guides and proportional chamber cabling extends. The area of each endplate covering the barrel veto section of the detector contains 192 machined holes for light guide access to the barrel veto.

The entire magnet assembly is rigged onto tracks allowing the endplates and central section to be moved independently (on machine rollers). This facilitates the installation of detector elements and allows proper positioning of the magnet in its extreme upstream position when the experiment is operating.

The magnet is powered by two power supplies, each rated for 4600A at minimum of 150V. The SCR design of the power supplies makes the current fed to the solenoid inherently noisy. To reduce this problem a large L-C filtering circuit was placed in series with the main coil. (A spare Panofsky quadrupole magnet was used to provide the additional "L", needed to isolate the capacitor bank from the power supplies).

2.3 The Beamline

A schematic view of AGS low energy separated beamline #1 ,LESB 1, is shown in Fig. 14 The septum magnet (D1) captures low momentum positive particles emerging from the tungsten target at the production angle of 10.5 degrees,* and steers them toward a pair of quadrupoles (Q1 and Q2). These are followed by another dipole (D2) which provides momentum separation as well as dispersing the beam in such a way that a better image is obtained at the mass slit[24]. An electrostatic separator is next, followed by another pair of quadrupoles (Q3 and Q4) immediately upstream of the horizontal mass slit. Finally, the beam is recombined and focussed by a last pair of quadrupoles bracketing a bending dipole (Q5, D3 and Q6).

The E787 solenoid (D4) is positioned as close to Q6 as possible to minimize kaon losses due to decays in flight, being about 16% per meter for 750 MeV/c kaons. The length of the beamline is 14.2 meters, resulting in a loss of $\sim$ 92% of the kaons which enter the beamline acceptance at Q1.

* An interesting number to quote is the effective solid angle of acceptance defined by D1, which is 2.5 mSter.

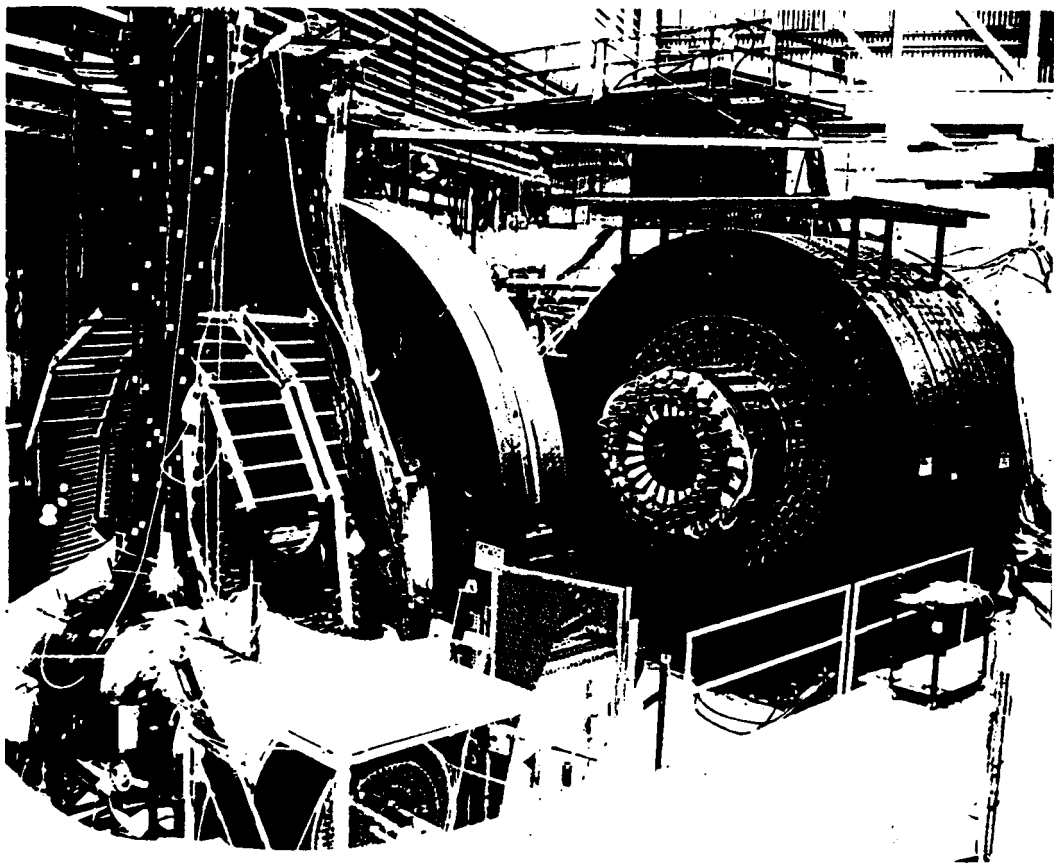

Figure 13. Photograph of the E787 detector before closing. The central section and endplates were rigged onto tracks located in the "pit", allowing them to be moved independently. The 24 range stack sectors can be seen protruding from the central section, radially followed by 48 sectors by 4 layers of barrel veto *logs*. Barely visible in the foreground is the central drift chamber prior to installation.

2.4 The Detector Beam Elements

This section will deal with the detector elements encountered by the beam after it emerges from the last focussing quadrupole (Q6). These can be categorized into four distinct subsystems: a Čerenkov counter, a beam MWPC, a set of scintillator

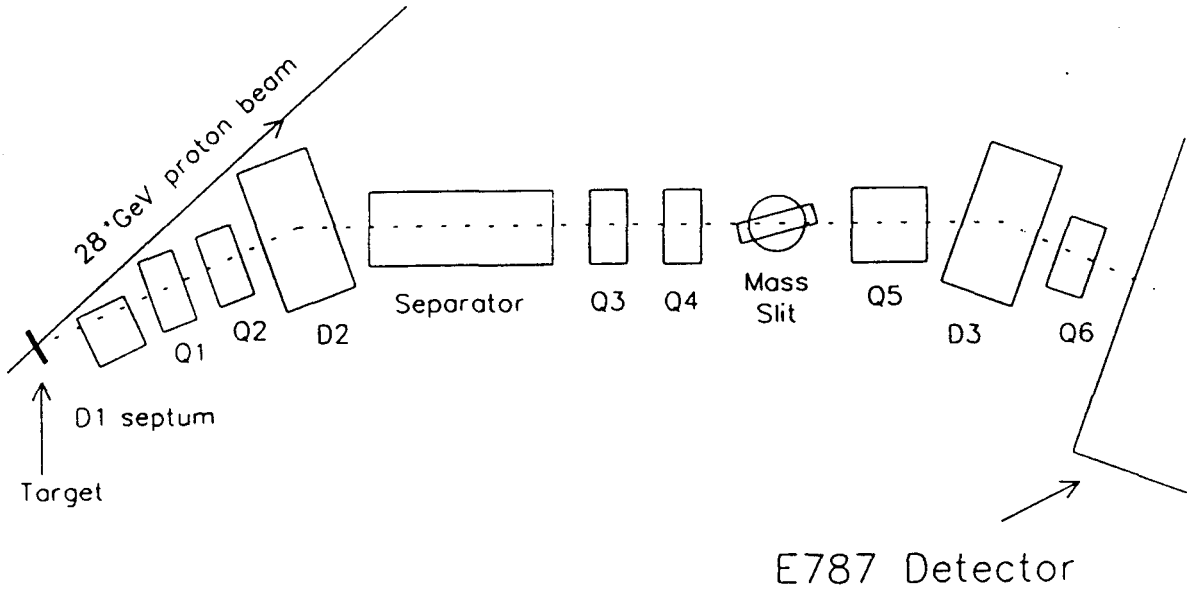

Figure 14. A schematic picture of the LESB 1 (low energy separated beam) beamline showing the relative positioning of the elements.

counters, and a degrader. The relative positioning of these components is shown in Fig. 15. The subsystems are described below.

2.4.1 The Čerenkov Counter

Basic Parameters:

Can diameter	43.8 cm
Can length	46.0 cm
Kaon phototubes	10 two inch EMI 9954KB
Pion phototubes	10 two inch EMI 9954KB
Instrumentation	Discriminators on all channels. ADC's and TDC's on ΣI discriminator outputs

The beam Čerenkov counter design is based on the fortuitous fact that for particles in the momentum range of interest to this experiment ($\sim$ 750 MeV/c) the velocities of K's and π's are such that the Čerenkov light from π's suffers total

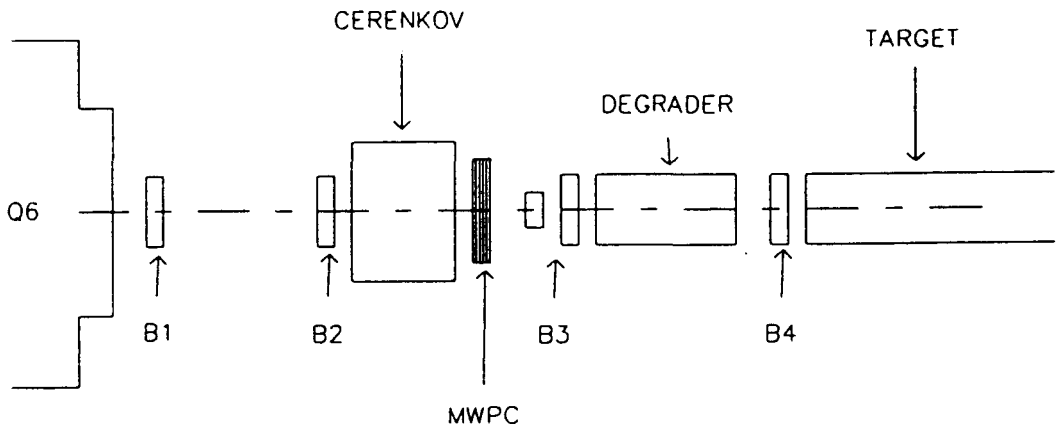

Figure 15. A schematic view of the E787 detector beam system. Shown is the relative positions of the Čerenkov counter, the beam wire chamber, the degrader, and the various scintillator elements.

internal reflection inside a lucite radiator, whereas the light from K's does not. This allows for the compact construction of a Čerenkov counter for the specific purpose of separating pions and kaons. A sketch of the design is shown in Fig. 16[25].

Since the light collection is quite efficient the timing characteristics of the $\check{C}_K$ signal are good, making it ideal as the main "beam" timing signal of the experiment. The $\check{C}_K$ phototubes have the additional advantage that they (by definition) do not see most of the π light.

2.4.2 The Beam MWPC

Basic Parameters:

Active area	5.1 cm high by 11.8 cm wide
Number of planes	3 (0°, +45°, −45° to vertical)
Sense wires per plane	72,120,120
Wire spacing	1.27 mm
Resolution per plane	$\sigma \leq 1$ mm
Timing Resolution	$\sigma \sim 5$ ns

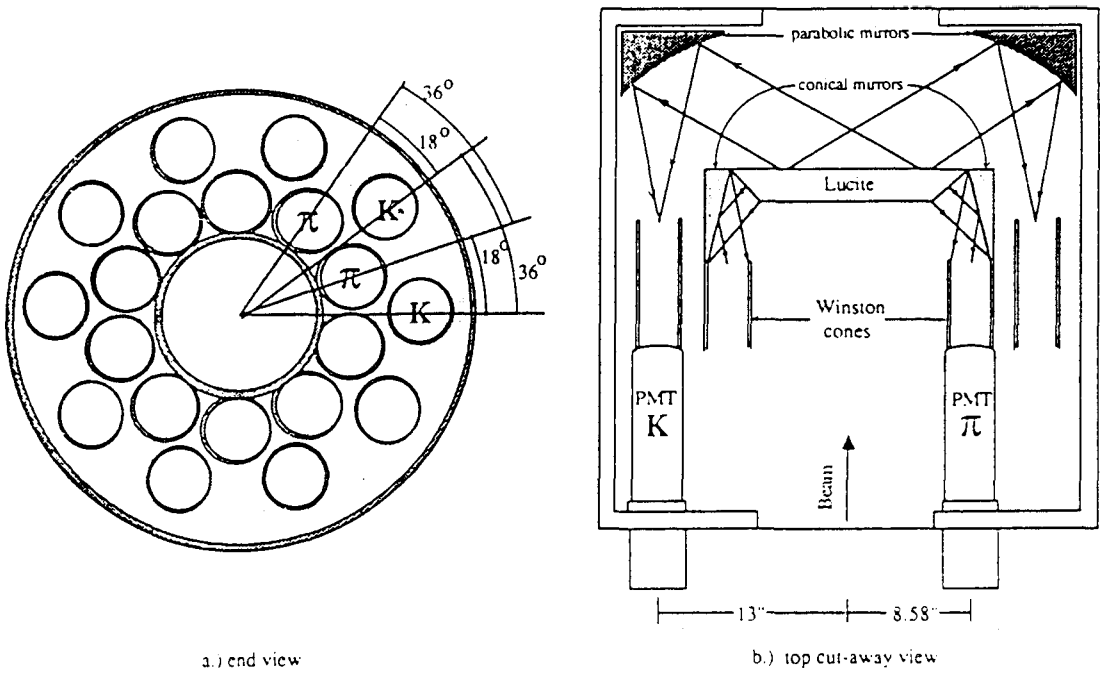

Figure 16. Rough outline of the Čerenkov counter design showing the how the K and π light is separately collected.

The main purpose of this device is to provide both spatial and timing information with sufficient resolution to allow detailed beam particle identification to be performed offline. This allows, for instance, the rejection of events where more than one beam particle entered the detector during the ADC gate. It is also useful as a monitor of the overall beam position and focus.

The chamber uses three planes whose wires are tilted at 0°, +45° and − 45° with respect to vertical. The wire pitch in each plane is 1.27 mm, but the wires are paired for a *net* pitch of 2.54 mm. The position resolution of any of the planes is about 1 mm. The overall hit position resolution is somewhat better since the problem is over-constrained.

2.4.3 The Beam Scintillators

Basic Parameters:

Number of elements	4

Effective element thickness	3.2 mm, 3.2 mm, 3.2 mm, 6.4 mm
Phototubes	Hamamatsu R1548 (dual photocathode)
Instrumentation	ADC's and TDC's on all channels

As can be seen in Fig. 15, the counters B1, B2, B3 and B4 form a telescope for the incoming particles.

— B1 is 17.5 cm wide by 4 cm high by 3.2 mm thick, and is positioned well upstream, close to the final quadrupole Q6.

— B2 is a hodoscope positioned immediately upstream of the Čerenkov counter. It has 8×4 segments in x and y respectively, and is 20 cm wide (in 2.5 cm slices) and 4 cm high (in 1 cm slices). Both B2 hodoscope layers were 3.2 mm thick.

— B3 was located between the MWPC and the degrader, and was intended mainly for beam tuning. It consists two elements, one small (5.1 cm by 3.8 cm by 3.2 mm), and one large (11.4 cm by 11.4 cm by 3.2 mm).

— B4 is a 4×4 hodoscope positioned at the downstream end of the degrader. As well as providing position information, it is also designed to be used as a dE/dx counter, allowing us to distinguish kaons from pions in the beam.* Each layer of this hodoscope is 6.4 mm thick by 10 cm wide in 2.5 cm slices.

2.4.4 The Degrader

Basic Parameters:

Material	BeO
Length	50.80 cm
Diameter	12.70 cm

A cylindrical BeO degrader was used to slow the incoming kaons sufficiently so they would, on average, stop in the center of the fiducial target region. The choice of degrader material was made after a careful Monte Carlo study of its effect on the beam, considering factors such as multiple scattering and kaon losses due to interactions.

* Since kaons about to enter the target are moving slowly and are hence more heavily ionising than the faster pions.

2.5 The Target System

Basic Parameters

Target radius (to flat)	5.31 cm
Length of fiducial region	24 cm (defined by I-counters)
Number of I-counters	6 (one on each target side)
I-counter thickness	0.635 cm
Number of clusters	378 + central fiber
Fibers per cluster	6
Fiber diameter	2mm
Phototubes	379 3/8 inch Hamamatsu R1635-02 on target elements
	12 2 inch EMI9813B on I and V counters
Instrumentation	ADC's and TDC's on all channels

The target system is designed to give ADC and TDC information about the stopping K^+, its subsequent decay and the resulting tracks [26,27]. Since resolving the (x, y) position of events is an important design parameter, the target is segmented into 378 independent clusters each with its own electronics[28]. This segmentation is also needed to reduce the average singles rate per element to a manageable level.

Fig. 17 shows how the 378 triangular clusters are stacked to form the finished hexagonal target geometry. Notice that the target is divided into three equivalent diamond shaped sub-structures. These were constructed separately and then assembled into the final shape. Each diamond contains 126 clusters, arranged in a nine by fourteen interlocking array[29].

The detailed makeup of each cluster is shown in Fig. 18. These are made by stacking six scintillating fibers (each two mm in diameter) into a mold and casting with epoxy, resulting in the triangular shaped clusters that are discussed above. The epoxy was carefully chosen to cure in such a way that any damage to the fibers was minimized.

The fibers themselves are made of 2 mm scintillator surrounded by a 25 μm dielectric cladding to improve the internal reflection properties of the fiber. As a measure to reduce optical crosstalk, each fiber was coated with 1000 Å of vacuum deposited aluminum. This aluminum coating also served the important function of protecting the cladding from being oxidized by the epoxy. The upstream ends of the fibers were also coated by a $\sim$ 1000 Å layer of vacuum deposited aluminum. It was found that this reflective layer increased the light yield at the phototubes by about 70%.

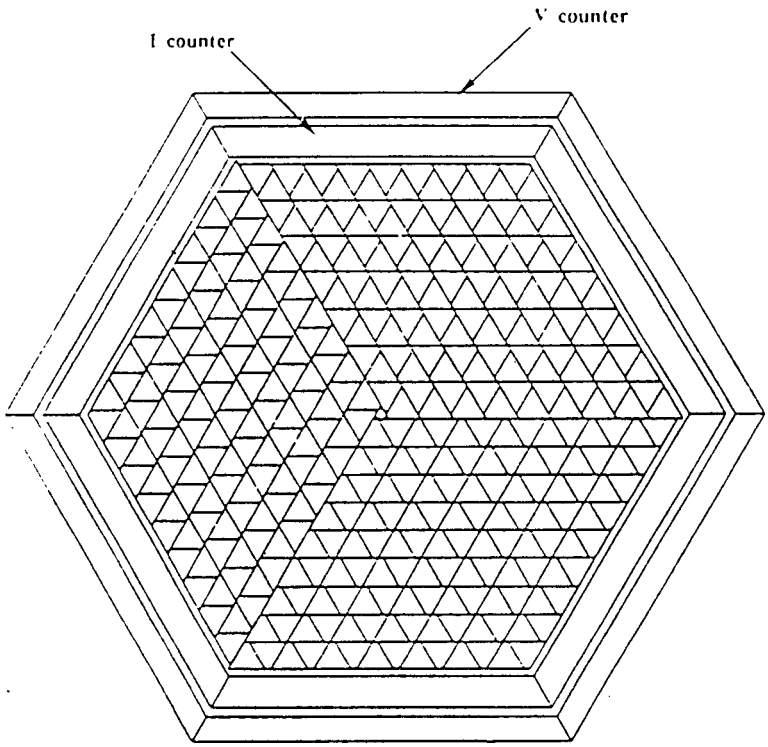

Figure 17. The geometry of the segmented target. The 378 triangular clusters are stacked to form the final hexagonal shape. The I-counters can be seen "lining" the outside of the target hexagon.

A notable feature of the target is that the scintillating fibers used also serve as lightguides to the phototubes. This approach of "active" lightguides simplifies the construction of the system and eliminates dead material in a region where good γ detection is desirable, but is not without drawbacks. The main potential problem is that the fiducial stopping region is not well defined. To remedy this the six outer edges of the target are surrounded by 6.4 mm thick "I-counters", whose active surfaces serve to define the acceptable stopping volume of the target[24]. Fig. 19 shows the positioning of the I-counters. The V-counters, used to veto particles which leave the target-lightguide system too far downstream, are also shown.

An LED flasher system was mounted on the upstream face of the target as an aid in the initial debugging of the 379 channels of ADC's and TDC's, and to allow

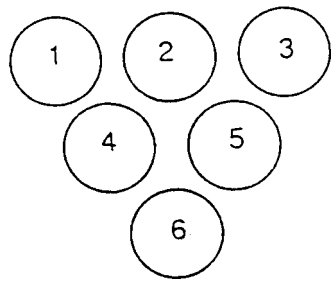

Figure 18. The composition of one of the triangular target clusters. The six coated scintillating fibers are cast in ScotchCast#8 epoxy, having a density of ~ 1.2.

periodic monitoring of the systems performance.

2.6 The Range Stack

Basic Parameters

Number of sectors	24
Layers per sector	21, 15 after ganging
Total thickness (flat $\rightarrow$ flat)	44.5 cm
Length of scintillator	182 cm (except T counter)
RSPC's per sector	2
Phototubes	672 EMI 9954KB on layers A-21
	48 Hamamatsu R1398 on T-counters
Instrumentation	ADC's and TDC's on all channels
	TD's on layers 11 $\rightarrow$ 18

The primary function of the range stack is to measure the range and energy of secondary particles from kaon decays. The stack is composed of twenty-four equivalent sectors, each one occupying fifteen degrees of cylindrical azimuth between ($-91\,\text{cm} \leq Z \leq +91\,\text{cm}$) and ($45.1\,\text{cm} \leq R \leq 89.6\,\text{cm}$).

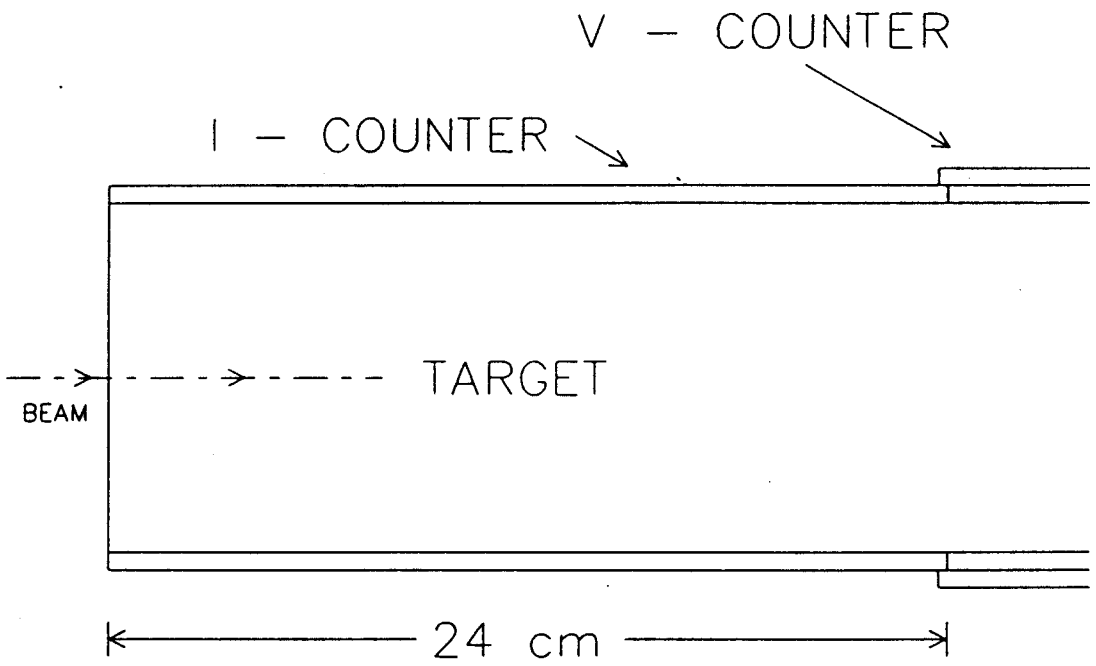

Figure 19. Side view of the target system showing the relative positioning of the I and V counters.

Fig. 20 shows how the twenty one pieces of scintillator are assembled to make each sector. Notice that the inside (smallest) counter is unlike the others in that its thickness is .635 cm rather than 1.905 cm. These T-counters differ also in that their active length is only 52 cm instead of the usual RS counter length of 182 cm. The T-counters serve to define the fiducial volume of the range stack as viewed from the target. This can be more clearly seen in the side view shown in Fig. 21.

The remaining twenty counters form the "stopping" region of the detector. Since range resolution is not critical (for $K^+ \to \pi^+\nu\bar{\nu}$) in the inner $\sim$ 18 cm, the individual counters in this region are ganged together as shown in Fig. 20, (this was also necessary due to the space limitations of light guides, phototubes and shields).

Also indicated in Fig. 20 is that each sector contains two wire chambers. These MWPC's are used to measure the z and ϕ positions of tracks penetrating the range

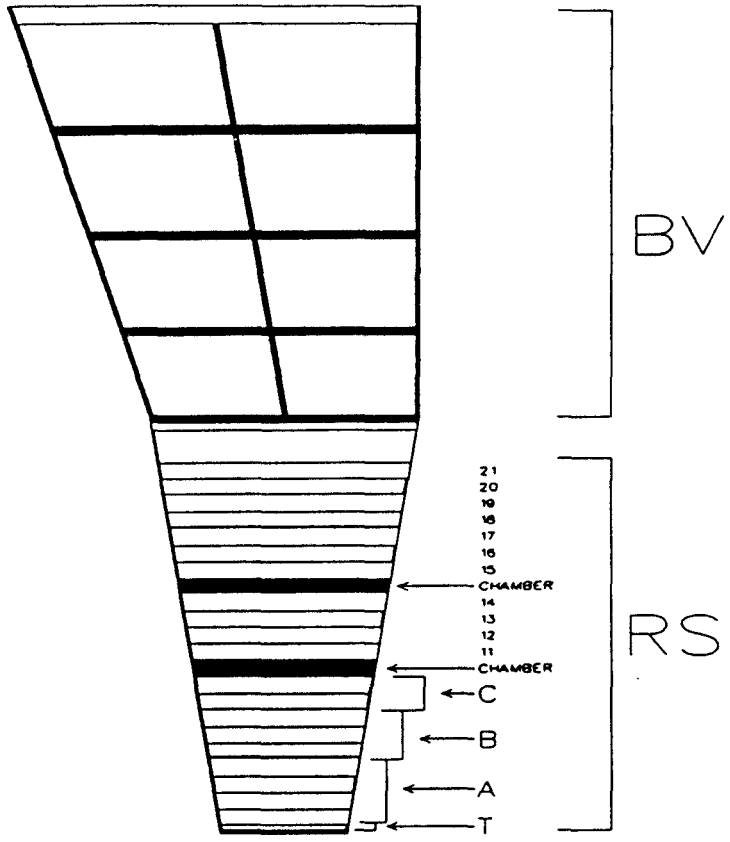

Figure 20. End view of one of twenty four range stack sectors, also showing the positioning of the barrel veto modules radially outside the range stack. The range stack layers are labeled according to the convention used in the rest of this thesis. Notice the position of the two range stack proportional chambers.

stack, providing information for both the online trigger system, and the offline trackfinding algorithms.

Although the RSPC's were not a crucial subsystem in the analysis of $K^+ \to \pi^+\mu^+\mu^-$ data, a brief description will be given for completeness.

Fig. 22 is a rough schematic of the design of one such chamber. The serpentine

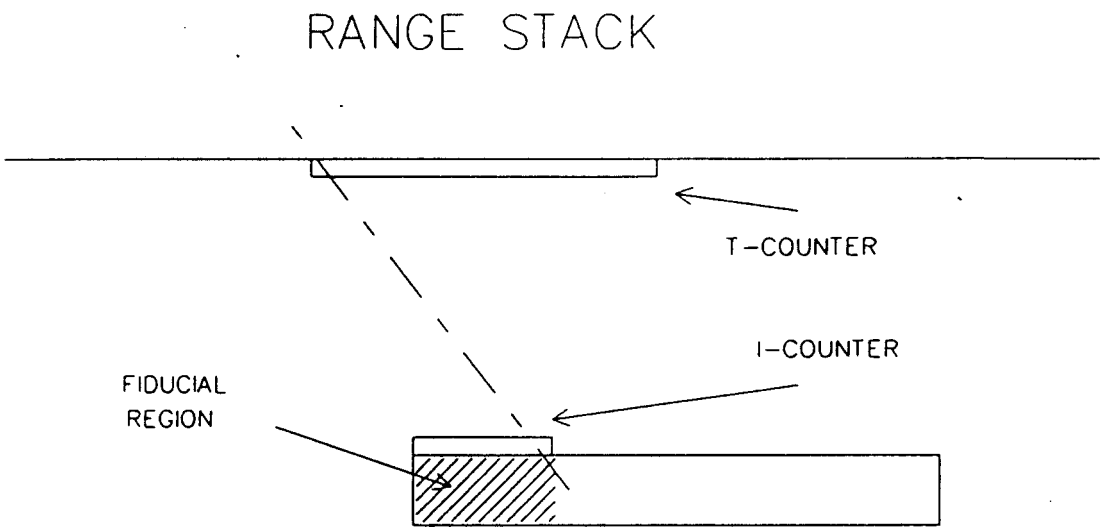

Figure 21. Side view showing the relative positioning of the target and range stack. Notice how the I-counters define the fiducial region of the target as the region from which a track can strike both the I-counters and the range stack T-counters. Counter sizes are exaggerated.

cathodes facilitate the use of TDC's to measure the Z position of a hit, while a tapped delay line system reading the anode wires provides additional data which can be used to deduce the azimuthal position "X" of the hit. The resolutions are roughly 1 cm in Z and 3.5 mm in X.

The entire range stack system (scintillators, light guides, chambers) is supported by a stainless steel "spider web", which is shaped in such a way as to provide the maximum support without extending into the fiducial region.

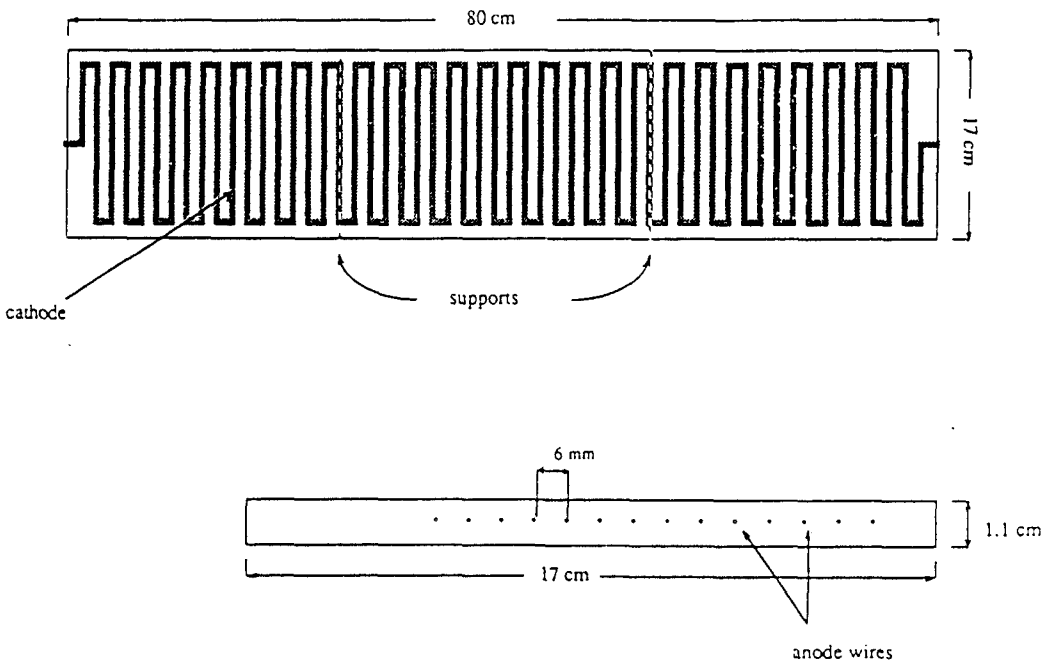

Figure 22. Design of the RSPC's. The serpentine cathode allows the z of a hit to be determined by measuring the difference in arrival time of the cathode pulses at the two ends.

2.7 The Barrel Veto

Basic Parameters

Innermost point	94.99 cm
Outermost point	147.96 cm
Total thickness	50.65 cm
Length of scintillator	190 cm
Number of sectors	48
Layers per sector	75
Layer composition	5mm scintillator, 0.012 L_{rad} each
	1mm lead sheet, 0.179 L_{rad} each
Mass per sector	879 kg
Segments per sector	4
Layers per segment	16, 18, 20, 21
Average radiation length	3.49 cm
Number of radiation lengths	14.05

Visible energy fraction		~ 0.3
Total mass		21.1 tons
	frame	3770 kg
	lead	10960 kg
	plastic	6230 kg
	wrapping	140 kg
Phototubes		384 three inch EMI 9821KB
Instrumentation		ADC's and TDC's on all channels

The barrel veto is situated radially outside the range stack, covering 2π in azimuth and ± 95 cm in Z. The main purpose of the barrel veto is to provide $4\pi\,\gamma$ ray detection (in conjunction with the endcaps) for efficient vetoing of $K^+ \rightarrow \pi^+\pi^0$ events.

Referring again to Fig. 13, we can see the 48 sectors $\times$ 4 layers of barrel veto "logs". Notice the non-projective geometry of the barrel modules, needed to eliminate photon losses in the support structure and associated gaps. The individual modules are extremely heavy, almost 900kg per sector, hence the barrel veto spider web must provide support along the full length of the logs to prevent them from sagging. These support "boxes" are bolted directly to the inside surface of the magnet, and are thermally decoupled by water cooling the outside of the boxes.

2.8 The Endcap Vetoes

Basic Parameters

Number of endcaps	2
Sectors per endcap	24
Pb-Scint layers per sector	66
Layer composition	5mm scintillator, 0.012 L_{rad} each
	1mm lead sheet, 0.179 L_{rad} each
Number or radiation lengths	14.6
Phototubes	48 two inch EMI 9854KB
Instrumentation	ADC's and TDC's on all channels

The endcap γ-veto consists of two plugs which fit into the central holes in the magnet endplates. They fit in such a way as to "fill the γ -gap" left by the barrel veto, as can be seen in Fig. 11.

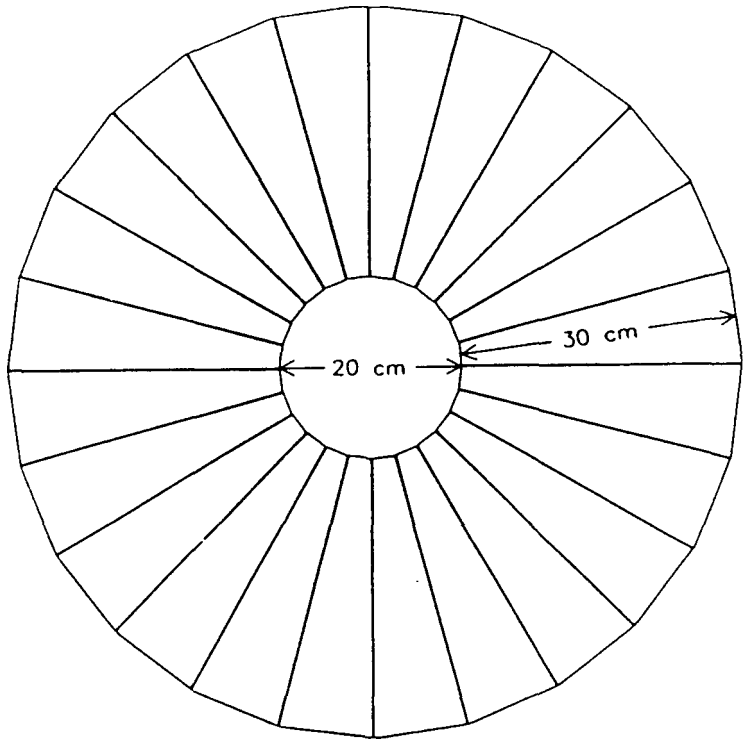

Figure 23. The design of the endcaps. The petal shaped lead-scintillator stacks are individually read out using a wave-shifter light-guide combination. Sizes shown are approximate.

The two endcaps are very similar in design, consisting of a central hole for the beam (or target) surrounded by twenty-four petal shaped lead-scintillator sectors, as shown in Fig. 23. The sectors are individually read out by wave-shifter bars.

2.9 The Central Drift Chamber

Basic Parameters

Inside radius	9.5 cm
Outside radius	43.2 cm
Active length	50.8 cm
Endplate thickness	13.5 mm (aluminum)
Wall thickness	0.5 mm (graphite-epoxy)
Number of layers	5
Cells per layer	36, 40, 50, 60, 70
Total number of cells	256
Sense wires per cell	8, 6 of which are instrumented

Gas mixture	Ar-Ethane (50:50)
Lorentz angle	$\sim 24°$ at 1 Tesla
Drift Time	200 ns to 400 ns
Hit resolution	$\sim 200\mu m$
Momentum resolution	$\frac{\Delta P}{P} \sim 2\%$

The central drift chamber is situated radially between the target and the range stack. It is long enough in the Z dimension to subtend the 2π solid angle of acceptance defined by the range stack and target.

The chamber consists of 256 cells, arranged in five radial layers as shown in Fig. 24 Layers 1, 3, and 5 are designed to measure the location of tracks in the X-Y plane. Layers 2 and 4 are "twisted" at stereo angles of 3.1° and 4.0° to provide Z information about the tracks.

The geometry of each cell is shown in Fig. 25 The dotted line represents the drift direction of electrons, which deviates from horizontal by $\sim 24°$ (the Lorentz angle). The eight sense wires are spaced 5.1mm apart, and of these only wires $2 \rightarrow 7$ are instrumented. A noteworthy feature is that the sense wires are alternately staggered by $254\,\mu m$ from the midplane to resolve the left-right ambiguity of tracks passing through the cell.

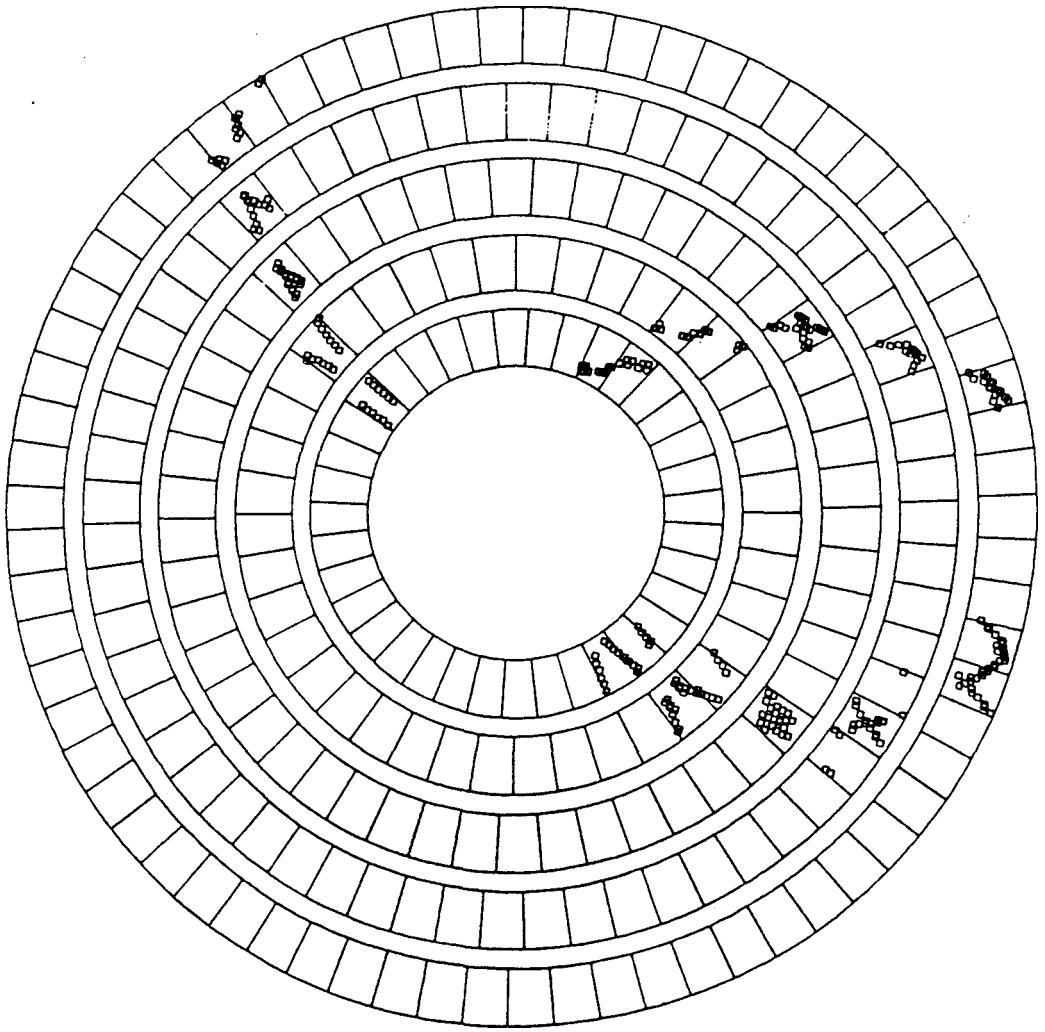

Figure 24. The geometry of the cylindrical drift chamber. The five radial layers are segmented into 36, 40, 50, 60, and 70 cells respectively. Layers 2 and 4 are at stereo angles to provide z information. The hits shown are from one of the $K^+ \rightarrow \pi^+\mu^+\mu^-$ candidates.

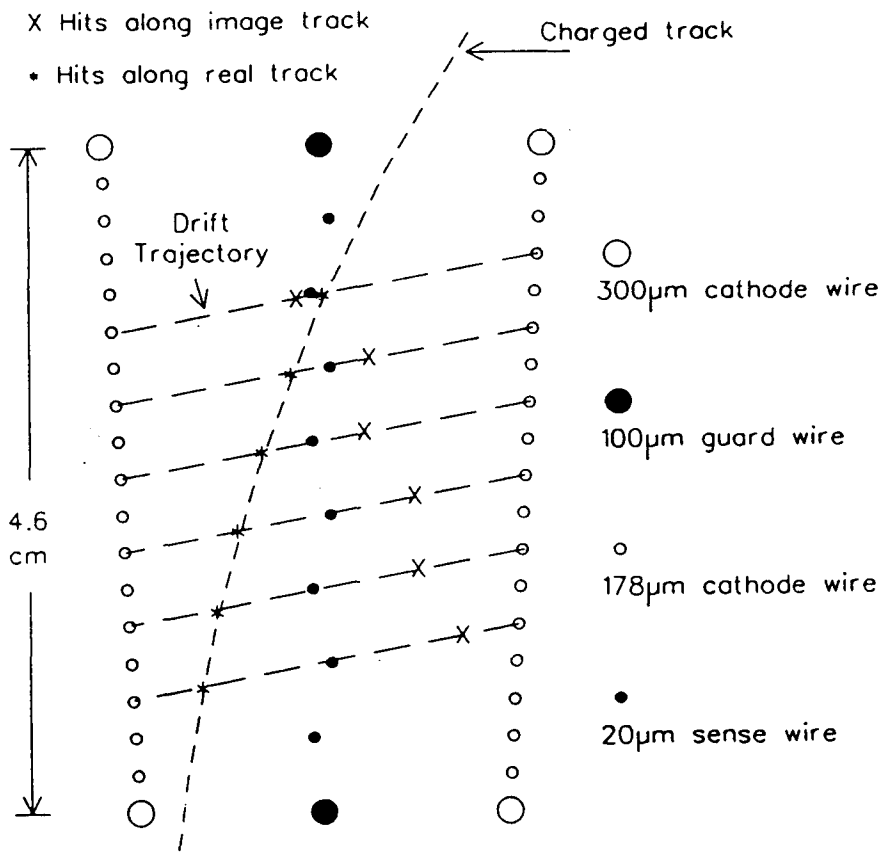

Figure 25. A rough sketch showing the construction of each of the 256 cells making up the drift chamber. Only the central six sense wires are instrumented. The horizontal dashed lines represent drift trajectories of electrons produced by a passing charged particle. The effect of staggering the sense wires can be seen by noticing how poorly aligned the image hits (×) are compared with the real hits (*).

3. The Data

3.1 Introduction

This section describes the processing of the $K^+ \rightarrow \pi^+\mu^+\mu^-$ data, from the trigger level to the final offline analysis. Also presented is a brief description of the running conditions under which the data were taken.

3.2 Data History

The 183 tapes of data used in this analysis are the result of the last two weeks* of E787's 1988 run. The total number of $K^+ \rightarrow \pi^+\mu^+\mu^-$ triggers on these tapes was 658,226, resulting from an exposure of 0.96×10^{10} $K_{T live}$'s.†

During most of this running period the beam intensity was such that about $130,000 \rightarrow 150,000$ K^+'s stopped in the target per spill, with the exception of a few runs having intensities as high as 280,000 K_T/spill and as low as 35,000 K_T/spill.

---

* May 4 → May 18, 1988.

† $K_{T live}$ is defined as $K_T \times$(fractional livetime), the total number of K^+'s that stopped in the detector while it was "live". The definition of K_T is given on the next page, and the fractional livetime typically varied from 60% to 80% depending on the beam rate and trigger mixture. The $K^+ \rightarrow \pi^+\mu^+\mu^-$ trigger was always mixed with other triggers, such as $K^+ \rightarrow \pi^+\nu\bar{\nu}$, $K^+ \rightarrow \pi^+\gamma\gamma$, and others used for calibration and monitoring. The most commonly used calibration and monitor "mix" used was the addition of one or two triggers per spill of K_{beam}, $K^+ \rightarrow \pi^+\pi^0$, $K^+ \rightarrow \mu^+\nu(1)$, $K^+ \rightarrow \mu^+\nu(2)$, $K^+ \rightarrow \pi^+\nu\bar{\nu}$(L0) and $K^+ \rightarrow \pi^+\gamma\gamma$(L0), where L0 denotes that these triggers were not subjected to level 1 or level 2 filtering.

3.3 THE LEVEL 0 $K^+ \rightarrow \pi^+\mu^+\mu^-$ TRIGGER

A detailed explanation of the trigger system is presented in appendices A and B, hence only a brief description is given here.

The definition of the $K^+ \rightarrow \pi^+\mu^+\mu^-$ level 0 trigger is:

$$K_{\mathrm{T}} \cdot DC \cdot (2T \cdot A's \text{ or } 3T \cdot A's)$$
$$\bullet\overline{(C_{\mathrm{CT}} + 11_{\mathrm{CT}} + 12_{\mathrm{CT}} + 13_{\mathrm{CT}} + 14_{\mathrm{CT}} + 15_{\mathrm{CT}} + 16_{\mathrm{CT}} + 17_{\mathrm{CT}} + 18_{\mathrm{CT}})}$$
$$\bullet\overline{(19 + 20 + 21 + BV + ECM + ECP)}$$

Where:

- $(T \cdot A)_i \Rightarrow$ Both ends of the T and A counters of sector i had discriminator hits in coincidence.
- $X_{\mathrm{CT}} \Rightarrow$ Range Stack layer X is part of a positive charged track. If the hit is in sector i, it is considered to be part of a positive charged track if either one of $(T \cdot A)_i$, $(T \cdot A)_{i-1}$, or $(T \cdot A)_{i-2}$ is asserted.
- $K_{\mathrm{T}} \Rightarrow K_{\mathrm{B}} \cdot \overline{VC}$
- $K_{\mathrm{B}} \Rightarrow \check{C}_{\mathrm{K}} \cdot B4 \cdot E_{\mathrm{T_g}}$: Where $\check{\mathrm{C}}_{\mathrm{K}}$ means there was a *kaon* signal from the Čerenkov counter, $E_{\mathrm{T_g}}$ means there was some energy deposited in the target, and $B4$ means there was hit in beam counter B4, located immediately upstream of the target.
- $IC \Rightarrow$ I-Counter sum above 0.15 MeV
- $VC \Rightarrow$ V-Counter sum above 2 MeV
- $BV \Rightarrow$ Barrel Veto sum above 5 MeV
- $ECM \Rightarrow$ Upstream Endcap sum above 10 MeV
- $ECP \Rightarrow$ Downstream Endcap sum above 10 MeV
- $DC \Rightarrow$ Delayed coincidence between $\check{\mathrm{C}}_{\mathrm{K}}$ and IC. This requirement rejected in-flight decays by demanding that there be at least a 2 ns delay between the time the K^+ stopped and the time it decayed. The decay time was assumed to be the time of a hit in the I-counters.

The above trigger was designed after a Monte Carlo study of $K^+ \rightarrow \pi^+\mu^+\mu^-$ decays showed events having at least two of the three decay tracks reaching the range stack will rarely have a track penetrating past layer B[30]. This Monte Carlo

result is shown in Fig. 26. This makes the $\pi\mu\mu$ trigger design particularly simple, as most of the detector is used as a veto. The only positive level 0 requirement, in addition to the usual beam logic, is that there be two or three T · A's in the range stack.

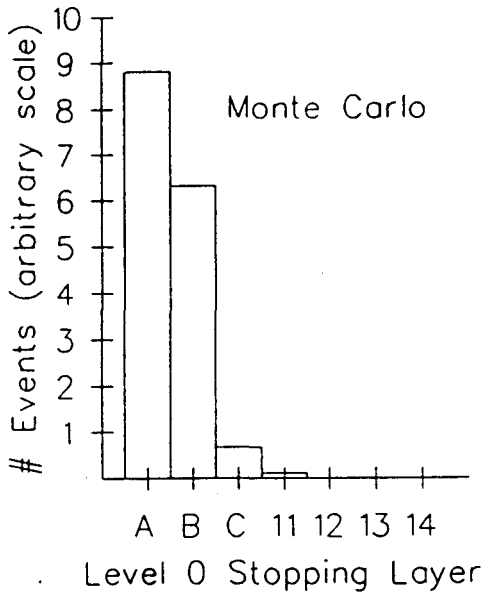

Figure 26. The Monte Carlo stopping layer for $K^+ \rightarrow \pi^+\mu^+\mu^-$ events passing the other level 0 cuts, as deduced by the level 0 trigger hardware (simulated). Notice that cutting on layer C as determined by the level 0 trigger will reject 5 % of the events having passed all other level 0 cuts.

There is a slight paradox in the trigger definition that deserves comment. Since the Q value for the decay is small ($\sim$ 140 MeV) most of the events will have only two tracks reaching the range stack. This leaves the third track to spiral around in the drift chamber. Many of these will "corkscrew" into the drift chamber endplate and one might think that the endcap veto would tend to reject events of this sort.* The reason this is *not* a problem is that these tracks have rather low momenta (less than 65 MeV in the $x - y$ plane) and the endplates are made of 1.3 cm thick aluminum. This will stop 70 MeV/c μ's at normal incidence, and particles spiraling

* The endcaps are located as close as possible to the ends of the central drift chamber.

in at an angle θ with respect to the normal of the plate will see the above thickness increased by a potentially large $1/\cos\theta$ factor.

The topology of $K^+ \to \pi^+\mu^+\mu^-$ events is sufficiently different from any of the more common decay channels that the very simple level 0 trigger shown above is all that is needed to reduce the trigger rate to about twenty events per spill. This simplicity also allows us to reliably determine the efficiency using Monte Carlo methods.

3.4 The Level 1 $K^+ \to \pi^+\mu^+\mu^-$ trigger

It was discovered that the $\pi\mu\mu$ trigger rate could be further reduced by a factor of two by using a simple level 1 trigger demanding that at least twenty target elements be hit. This level 1 trigger was deployed for $\sim 90\%$ of the $\pi\mu\mu$ data used in this analysis.

Fig. 27 is a simplified flowchart showing the sequence of events in the trigger system for a typical physics trigger (like $K^+ \to \pi^+\mu^+\mu^-$).

3.5 The Offline Analysis

3.5.1 KOFIA: Kaon Offline Interactive Analysis

The program KOFIA is the base for all E787 offline analysis. It is basically an analysis shell designed to fetch events from an input device and present them to user routines for subsequent analysis. It also handles the associated book keeping chores, such as accumulating scaler sums and keeping track of non-fatal error conditions. All the analysis performed on the $\pi\mu\mu$ data was done under KOFIA "supervision", with the exception of the Pass 0 analysis described below.

3.5.2 Pass 0

The purpose of pass 0 was twofold.

1) To "sort" the different trigger types found on the raw data tapes onto separate output tapes.

2) To do some simple and efficient cutting on the physics triggers in an attempt to reduce the number of tapes.

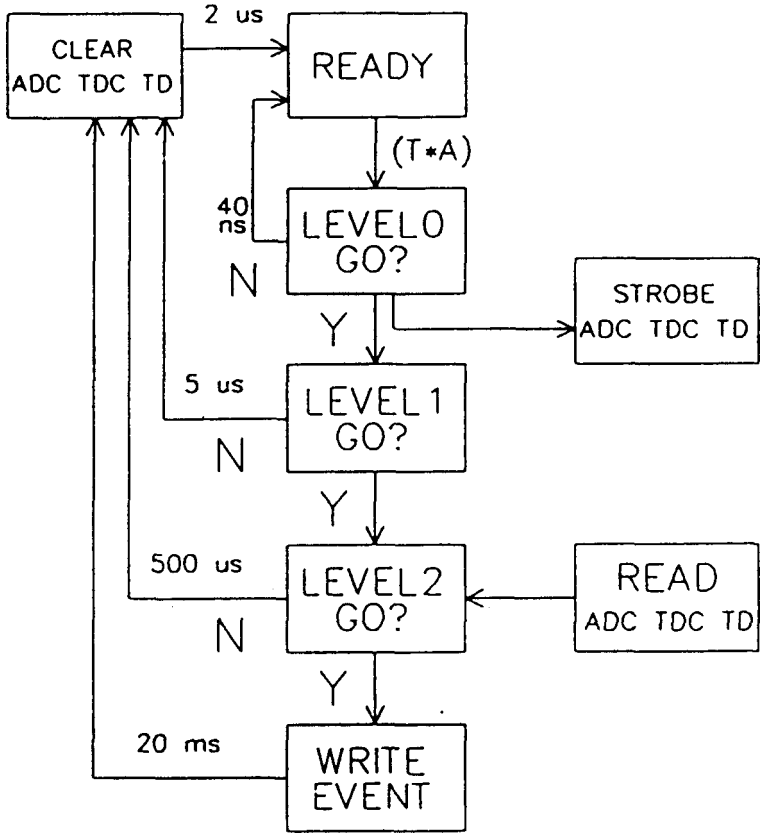

Figure 27. A simplified schematic of trigger system, showing the interaction of level 0, level 1, and level 2, with the data acquisition system.

Since the above task involved handling and analyzing hundreds of tapes, it was decided to do the processing on the IBM 3090 mainframe at BNL. An analysis shell similar in structure to KOFIA was written and implemented on the 3090 with this purpose in mind.

The pass 0 cuts applied to the $K^+ \to \pi^+\mu^+\mu^-$ data are listed below:

(*i*) Events having total in-time* energy greater than 5 MeV in the barrel veto and 10 MeV in the endcap were vetoed.

(*ii*) Layers C + 11 +...+ 21 of the range stack were allowed to have no more than 4 MeV of total in-time energy.

(*iii*) The in-time energy sum for range stack layers T, A and B was restricted to be less than 175 MeV.†

(*iv*) An I-counter "pattern cut" was performed demanding that at least two I-counters be struck, and if only two are hit they must not be adjacent.

The data reduction factor obtained from the above pass 0 cuts was approximately five for data taken with the level 1 trigger implemented and six for data taken with no level 1.

The reduced $K^+ \to \pi^+\mu^+\mu^-$ data set after pass 0 consisted of 127,210 events.

3.5.3 Drift chamber track reconstruction

The central drift chamber has five radial layers, each segmented into azimuthal cells.‡ Layers one, three and five are used for determining the track position in the $x-y$ plane only, and layers two and four are "twisted" to provide the stereo information needed for a z measurement. Due to the jet chamber design, a charged particle passing through a cell will give rise to a track "segment" in that cell, composed of up to six hits. In principle this segmentation of the track makes the reconstruction easier than for a conventional design, since each segment contains directional as well as positional information.

The reconstruction of a given track is done in two steps. First, a circular track is fit in the $x-y$ plane to the hits in layers one, three and five. This information is then used in layers two and four to deduce the z position of the stereo hits, which are then fit to yield the dip angle and absolute z position of the track.

There are several effects that complicate the above algorithm, all of which are aggravated when considering low momentum tracks:

- There is a left $\leftrightarrow$ right ambiguity in each cell because of its symmetric design. For stiff tracks this is usually not a problem as the correct track segment can

---

⋆ An ADC is considered to contain *in-time* energy if the TDC for the same channel showed a hit within 20 ns of the time of T · A.

† This is well above the total kinetic energy release for $K^+ \to \pi^+\mu^+\mu^-$ of 143 MeV.

‡ See the description furnished in the detector chapter for more details

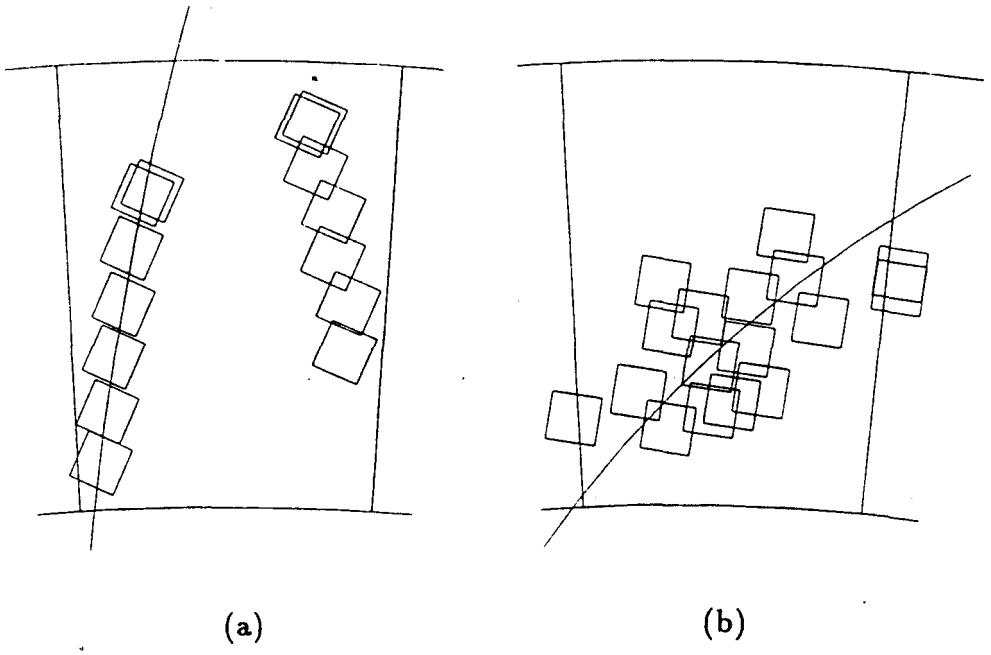

Figure 28. Examples of drift chamber cells having radial (a) and azimuthal (b) track segments.

be found by considering the χ^2 of the fit. For low momentum tracks traversing the cell "azimuthally", the problem is worse as the track segments will tend to overlap. Fig. 28 shows an example of each of the two above extremes.

- The circle-fit is inherently less accurate for low momentum tracks since these tracks tend to have little or no usable information in layer five. This means the radius of the circle must be determined from only two line segments at best.

- The z position obtained for the hits in the stereo layers depends critically on the fit in the $x-y$ plane, hence if there are large uncertainties in the circle fit the z information will be unreliable.
- Very low momentum tracks that do not reach layer four ($\lesssim$50 MeV/c) can not be reconstructed in z using the present algorithms.

Since the z fitting of low momentum tracks was inefficient and often inaccurate, it was decided that tracks that were successfully fit in the $x-y$ plane would be considered further even if the z fitting failed.*

3.5.4 Pass 1

The aim of the next two stages of analysis was to reduce the number of $\pi\mu\mu$ candidates to a small enough sample for handscanning. The selection is done by reconstructing each event with the assumption that it came from a $K^+ \to \pi^+\mu^+\mu^-$ decay, and applying cuts on quantities designed to measure how well the event fits this hypothesis.

To reconstruct all the events that survived pass 0 takes several days of VAX-3600 cpu time. To minimize the number of times this exercise had to be performed the pass 1 analysis was by definition the application of the *loosest* cuts possible that would serve to reduce the data to less than ten thousand events.

The structure of the event reconstruction program is shown in Fig. 29, and the selection cuts used in pass 1 are listed in table 3. The definitions of the various cuts are presented in the next section.

The pass 1 analysis reduced the data sample to 6,364 $\pi\mu\mu$ candidates.

3.5.5 Pass 2

Pass 2 was conceptually identical to pass 1, the only difference being that new cuts were added and the existing ones were made tighter. The type and "tightness" of the cuts were determined after a careful Monte Carlo study of $K^+ \to \pi^+\mu^+\mu^-$ decays, which is the subject of the next chapter.

The selection cuts used in pass 2 are listed in table 4

* It was found previously that even for low momentum tracks where a z fit was found, the errors were often so large that the z information was basically useless.

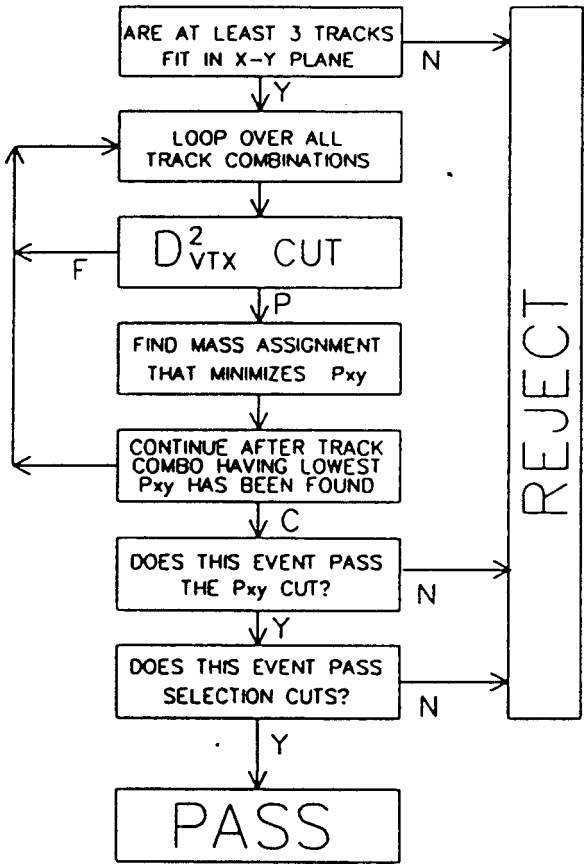

Figure 29. Flowchart of the $K^+ \to \pi^+\mu^+\mu^-$ event reconstruction algorithm.

3.5.6 Definitions and motivation for reconstruction cuts.

- $D^2_{vtx} \Rightarrow$ The sum of the squared distance of closest approach of each track to the point in the $x-y$ plane which minimizes D^2_{vtx}. Demanding that the three tracks all pass close to a single point (x,y) in the target will preferentially cut out events where the tracks are uncorrelated. It will also suppress $K^+ \to \pi^+\pi^0$ events where one of the γ's converted in the target since in this case the e^+e^- point of origin will tend to be removed from the K^+ decay vertex. A "good" vertex will have a small D^2_{vtx}.

Inner Loop	
Parameter	Constraint
D^2_{vtx}	$\leq 20\,cm^2$
P_{xy}	$\leq 60\,MeV/c$
Selection Cuts	
R_{vtx}	$\leq 5\,cm$
RS_{match}	≥ 1
N_{RS}	≤ 10
E_{BV}	$\leq 2\,MeV$

Table 3. Constraints imposed on the various selection parameters by the pass 1 analysis. See the text for definition of these parameters.

- $P_{xy} \Rightarrow$ The magnitude of the total momentum vector in the $x-y$ plane. If the $K^+ \to \pi^+\mu^+\mu^-$ decay occurs at rest† the total vector sum of the momenta at the decay vertex is zero. For events where there is missing energy, specifically $K^+ \to \pi^+\pi^0$, $\pi^0 \to \gamma e^+e^-$ (where the γ is missed), and $K^+ \to \pi^+\pi^-e^+\nu$, the total momentum can differ significantly from zero. The maximum "tightness" of this cut is limited by our ability to measure the momentum at the vertex. In practice we measure the momentum of a track in the drift chamber and the vertex momentum must be deduced by extrapolating the track back into the target, correcting for energy loss and the subsequent changing radius of curvature. Since multiple scattering and energy loss fluctuations cannot be taken into account in this process, the accuracy with which one can know the vertex momentum is limited to $\sigma \sim 20$ MeV/c.

- $R_{vtx} \Rightarrow$ The distance from the vertex (as found from reconstructing the drift chamber tracks) to the nearest point on the target edge. A positive value of R_{vtx} means the vertex was found to be outside the target. A cut on this quantity simply demands that the vertex found using the drift chamber tracks should not be far outside the target edge.

- $RS_{match} \Rightarrow$ The number of the drift chamber tracks used in the final reconstruction that point into struck segments in the range stack. Since we are by

† This should be the case since a delayed coincidence requirement was included in the level 0 $K^+ \to \pi^+\mu^+\mu^-$ trigger.

Events entering Pass 2		6,364
D^2_{vtx}	$\leq 5\,cm^2$	
P_{xy}	$\leq 60\,MeV/c$	
Events passing inner loop		4,787
Parameter	**Constraint**	**# Remaining**
R_{vtx}	$\leq 2\,cm$	4,730
RS_{match}	≥ 2	3,253
N_{RS}	≤ 5	1,049
E_{BV}	$\leq 1\,MeV$	948
P_{xy}	$\leq 40\,MeV/c$	549
θ_{min}	≥ 20 deg	280
D^2_{dc-tg}	$\leq 3\,cm$	139
E^{tg}_{junk}	$\leq 20\,MeV$	104
E^{ic}_{pmin}	$\geq 2\,MeV$	75
N_{TG}	≥ 20	72
P^{max}_{xy}	$\leq 150\,Mev/c$	41
IC_{match}	TRUE	32
E^{track}_{RS}	$\leq 120\,MeV$	26
E^{junk}_{RS}	$\leq 1\,MeV$	18
E_{EC}	$\leq 1\,MeV$	11

Table 4. Constraints imposed on the various selection parameters by the pass 2 analysis, and the number of events surviving each cut, applied in the order shown.

definition looking for a class of events where at least two tracks penetrate into the range stack, it is reasonable to demand the drift chamber and range stack information agree on this. (This is just an elaborate version of the level 0 trigger requirement of two or three T · A's). Two tracks pointing at the same range stack sector will count as two.

- N_{RS} $\Rightarrow$ The number of range stack counters with more than 1/2 MeV of in-time energy, *not* including T-counters. Most of the backgrounds one can imagine will have at least one electron track. If such an electron enters the range stack it will shower, resulting in a large number of hit counters. On the other hand, π^+'s and μ's will tend to deposit their energy in only one or two range stack counters. An exception worth mentioning is the behaviour of stopping π^-'s. As is discussed in chapter 5, these can also result in extra hits.

- E_{BV} $\Rightarrow$ The total in-time barrel veto energy.

- θ_{min} $\Rightarrow$ The minimum opening angle between any of three tracks found in the final reconstruction. The possible backgrounds $K^+ \rightarrow \pi^+\pi^0$, $\pi^0 \rightarrow \gamma\gamma$, $\gamma \rightarrow e^+e^-$ and $K^+ \rightarrow \pi^+\pi^0$ with $\pi^0 \rightarrow \gamma e^+e^-$ result in electron pairs created with small opening angle.

- DV_{dc-tg} $\Rightarrow$ The distance in the (x,y) plane between the position of the decay vertex as found by the drift chamber reconstruction and the center of the target fiber containing the most deposited energy, assumed to be the K^+ stopping fiber.

- E^{tg}_{junk} $\Rightarrow$ The energy outside, and not connected to, the main cluster of hit target elements. Since "junk" energy is typical of events where a γ converted in the target, it is desirable to try to measure this quantity.*

- E^{ic}_{pmin} $\Rightarrow$ The energy of the I-counter through which the lowest momentum track travels. Since e^+ tracks that enter the range stack are vetoed by the N_{RS} and E_{RS} cuts, the majority of surviving $K^+ \rightarrow \pi^+\pi^-e^+\nu$ events will have their e^+ track contained in the drift chamber. The ability to identify these tracks as e's as opposed to μ's or π's is crucial for rejecting $\pi\pi e\nu$ as a background to $\pi\mu\mu$. This identification is possible by measuring the dE/dx of the track in the target and I-counters. The potential of this technique can be illustrated by considering an unknown track having a momentum of 50 MeV/c (a typical momentum for tracks not reaching the range stack). As a rule of thumb, $dE/dX \sim dE/dX_{min}/\beta^2$. Hence, if the track were due to an electron, it would be roughly minimum ionizing since $\beta \sim 1$. For a heavier μ or π however, β^2 would be .18 and .12 respectively, and $dE/dX \gtrsim 5 \times dE/dX_{min}$. Since an accurate determination of dE/dx in the target for a given track is a difficult software task, it was decided to use only I-counter information at

* This main cluster is found by starting at the element having the highest deposited energy, (assumed to be the K^+ stopping element), and seeing which neighbors contain energy. This process then repeats in turn for each of these neighbors and so on until no more connected energy is found.

this level and to defer the more involved target dE/dx calculation to a "hand scan" algorithm. Only events where this track is not close to the I-counter edge are subjected to this cut, to avoid inefficiency due to small errors in the drift chamber fit. Also, only tracks with momentum less than 60 MeV/c are considered since at higher momenta the difference in dE/dx between $e^{\pm}$'s, μ's and π's becomes less distinct given the poor energy resolution of the I-counters. For the same reason, the minimum energy requirement in the momentum interval $50 \geq P \geq 60$ MeV/c was half of what it was for $P \leq 50$ MeV/c.

- $N_{TG} \Rightarrow$ The number of target elements containing more than 1/4 MeV deposited energy. As was mentioned earlier, some of the runs (about 10%) were not subjected to the level1 trigger which required that at least 20 target elements be hit. In order to have the entire data sample exposed to the same set of cuts, this requirement was demanded again.

- $P_{xy}^{max} \Rightarrow$ The maximum momentum of the three drift chamber tracks, measured in the $x-y$ plane. The maximum allowable momentum for a product of the decay $K^+ \rightarrow \pi^+\mu^+\mu^-$ is 172 MeV/c. Due to the detector geometry and trigger requirements however, there should rarely be a track with more than 150 MeV/c total momentum.

- $IC_{match} \Rightarrow$ Similar in nature to the RS_{match} cut, this demands that if an I-counter has one of the final reconstructed tracks going through it, it should contain deposited energy. Also required is that the I-counter be in contact with the main target cluster. This is a crude and simple attempt at matching target and drift chamber tracks.

- $E_{RS}^{track} \Rightarrow$ The sum of the in-time energies found in all range stack tracks. The Q value of $K^+ \rightarrow \pi^+\mu^+\mu^-$ is 142.7 MeV, however only a negligible fraction of events will have more than 120 MeV appearing in the range stack†.

- $E_{RS}^{junk} \Rightarrow$ The difference between the total range stack in-time energy and E_{RS}^{track}. Energy deposition in range stack counters *not* part of any tracks is characteristic of $K^+ \rightarrow \pi^+\pi^-e^+\nu$ events‡

- $E_{EC} \Rightarrow$ The total in-time endcap energy.

The pass 1 algorithm reduced the $K^+ \rightarrow \pi^+\mu^+\mu^-$ sample from over 127,000 events to 11.

† From Monte Carlo

‡ The e^+ shower can deposit energy over an extended region, and the π^- can interact to produce slow neutrons having a mean free path of ~ 30 cm.

3.5.7 Hand-scanning

A quick glance at the remaining eleven events allows us to reject six of them without resorting to any sophisticated hand scan algorithm. Of these six, two had a badly reconstructed drift chamber track,[§] and four had no range stack TDC information indicating a data-acquisition malfunction. The remaining five events had no obvious flaws and required closer inspection.

As was discussed above, a $K^+ \to \pi^+\pi^-e^+\nu$ event can appear to be a $K^+ \to \pi^+\mu^+\mu^-$ event if for some reason the e^+ cannot be distinguished from a μ^+. The worst scenario is that the decay vertex is close to the edge of the target[¶] and that the e^+ track and one of the other tracks emerge through the same I-counter. If the e^+ momentum is low enough that it does not enter the range stack and its dip angle is large enough that it hits the endplate of the drift chamber before re-entering the target, it will be extremely difficult to identify it as an electron. The usually powerful dE/dx method cannot be used since the pathlength is too small for a reliable target measurement, and the I-counter energy is contaminated by the second track.

We have no choice but to reject all events fitting into the above category, even though the $\pi\mu\mu$ acceptance will suffer. We will refer to this as the $\mathrm{IC_{plus}}$ cut.

If a low momentum track re-enters the target, particle identification is possible using a time-of-flight measurement. A 50 MeV/c e^+will complete one revolution in $\sim$ 3.5 ns while a μ having the same momentum would take $\sim$ 8 ns, (and a π even longer). This method will be extremely efficient since the timing resolution is at worst $\sim$ 2 ns, being much better in the usual case where several target elements are hit and their times can be averaged. We refer to this as the $\mathrm{TG_{\Delta T}}$ cut.

The $\mathrm{IC_{plus}}$ and $\mathrm{TG_{\Delta T}}$ cuts each claim one of the remaining five events, leaving three $\pi\mu\mu$ candidates.

§ In this case, *bad* means that in addition to finding the correct tracks, the reconstruction algorithm had found an extra track where there was none, meaning this is not an inefficiency problem.

¶ This condition is preferred for both $\pi\mu\mu$ and $\pi\pi e\nu$ decays since their Q values are low and the probability that all three tracks will emerge from the target is highest if the vertex is near the edge.

3.6 THE $K^+ \to \pi^+\mu^+\mu^-$ CANDIDATES

The three remaining candidates can be seen in Fig. 30, Fig. 31, and Fig. 32. Shown for each is a full detector display, and an enlarged view of the target system. The numbers next to the range stack counters show the in-time energy in the adjacent cluster of counters. Also listed for each track is the kinetic energy the particle would have if assigned the mass of a π, a μ and an e.

Listed with each candidate described below are two masses: The reconstructed K^+ mass and the μ-pair invariant mass. These were obtained by fitting the tracks in x, y and whenever possible z. The uncertainty in these numbers is about 7.5 MeV and 5 MeV respectively. The lowest momentum tracks of candidates #2 and #3 were not fitable in z, but since these momenta were < 38 MeV/c (in the $x-y$ plane) their contribution to the uncertainty in the reconstructed mass was small. The μ-pair mass was deduced from the momentum of the π^+ track, which was well measured in each case.

It should be noted that no in part of the analysis were events scrutinized on the basis of their reconstructed mass.

3.6.1 Candidate #1

Examining the event display, we see that this is an exceptionally clean event. The drift chamber momenta correlate well with the range stack energies given the mass assignments shown, as does the energy deposition in the target and I-counters. All three tracks can be fit in z.

Candidate #1	
Run 3029	Event 3061
$M_{\pi\mu\mu}$	494.3
$M_{\mu\mu}$	283.6

3.6.2 Candidate #2

This is also a very convincing $K^+ \rightarrow \pi^+\mu^+\mu^-$ event. The two tracks penetrating the range stack show the proper momentum energy correlation for the indicated assignments, neither one consistent with being an e^+. The dE/dx of the low momentum negative track in the I-counter should be at least 7 MeV for a μ^- and 11 MeV for a π^-. The energy observed is lower than both of these estimates.

Candidate #2	
Run 2980	Event 11491
$M_{\pi\mu\mu}$	495.3
$M_{\mu\mu}$	255.4

3.6.3 Candidate #3

This event is consistent with a $\pi\mu\mu$ hypothesis, and was therefore kept as a candidate. However, it is equally well explained as a $K^+ \rightarrow \pi^+\pi^-e^+\nu$ event. The reason for this ambiguity is that the only means of identifying the low momentum positive track is by considering dE/dx in the I-counter. If the particle is a e^+ we would expect it to leave between 1 and 1.5 MeV depending on the z-slope of the track. A μ^+ would leave between 7 and 10 MeV. The measured I-counter energy is 4 MeV, which is a factor of two away from either of the above predictions.

This type of event will not be a problem in future runs since the inner range stack layers will be instrumented with transient recorders which will allow us to identify negative tracks as either π^-'s or μ^-'s.

It is worth noticing that this event is topologically very similar to candidate #2, and that candidates #2 and #3 have the same μ-pair invariant mass. (The uncertainty in this mass is relatively small, about 5 MeV).

Candidate #3	
Run 2991	Event 2883
$M_{\pi\mu\mu}$	491.4
$M_{\mu\mu}$	256.0

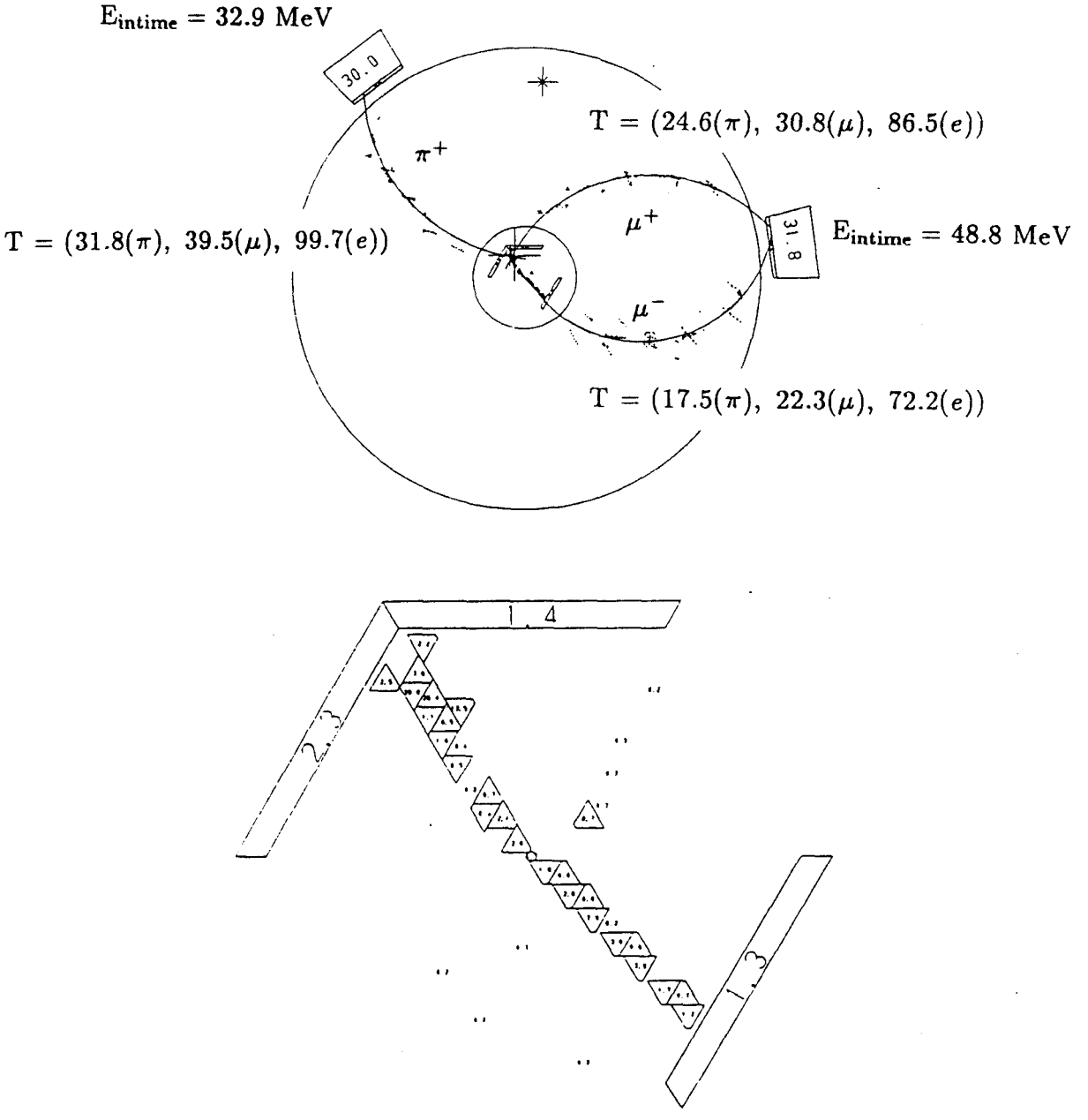

Figure 30. $K^+ \rightarrow \pi^+\mu^+\mu^-$ Candidate #1

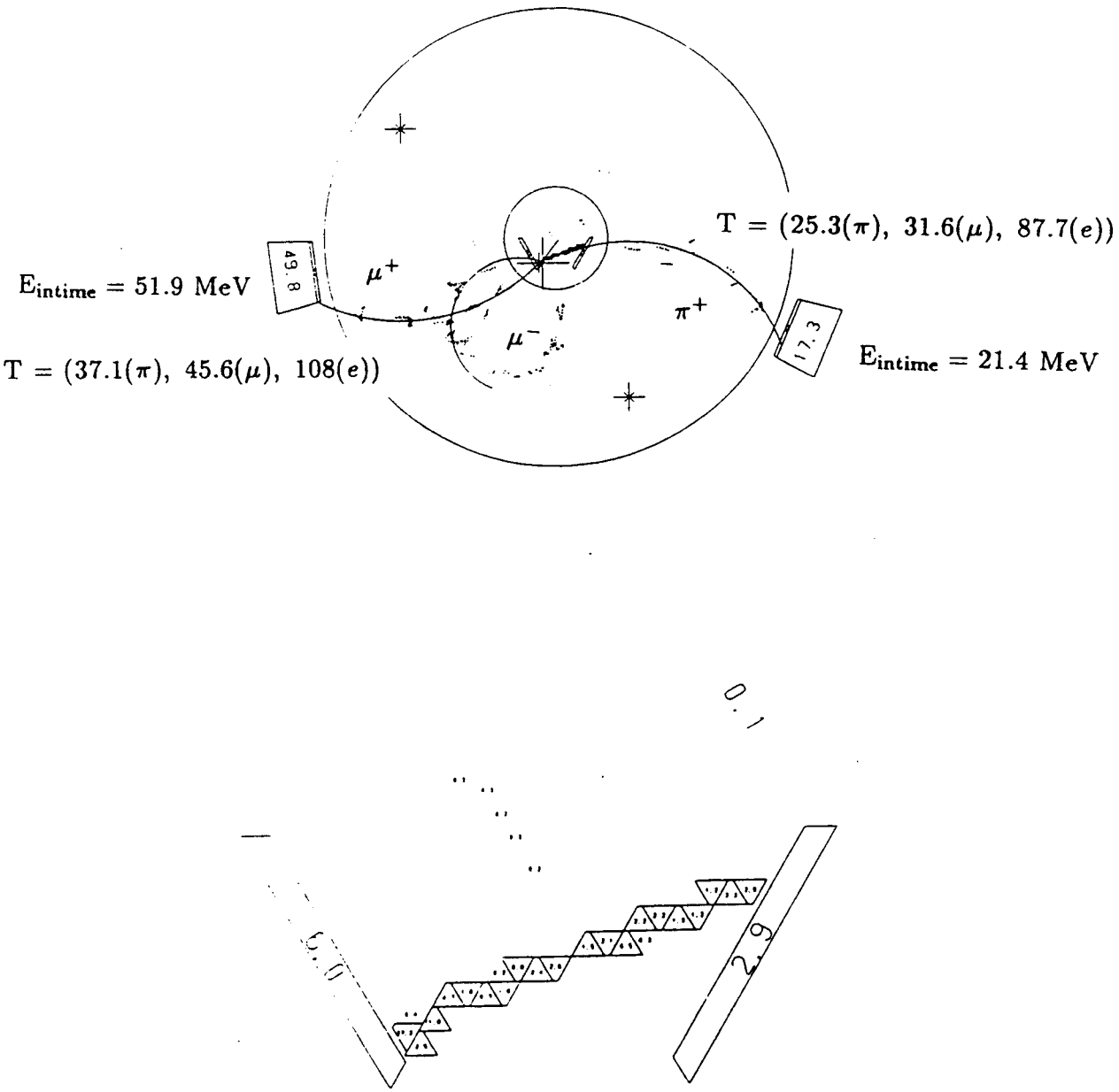

Figure 31. $K^+ \rightarrow \pi^+\mu^+\mu^-$ Candidate #2

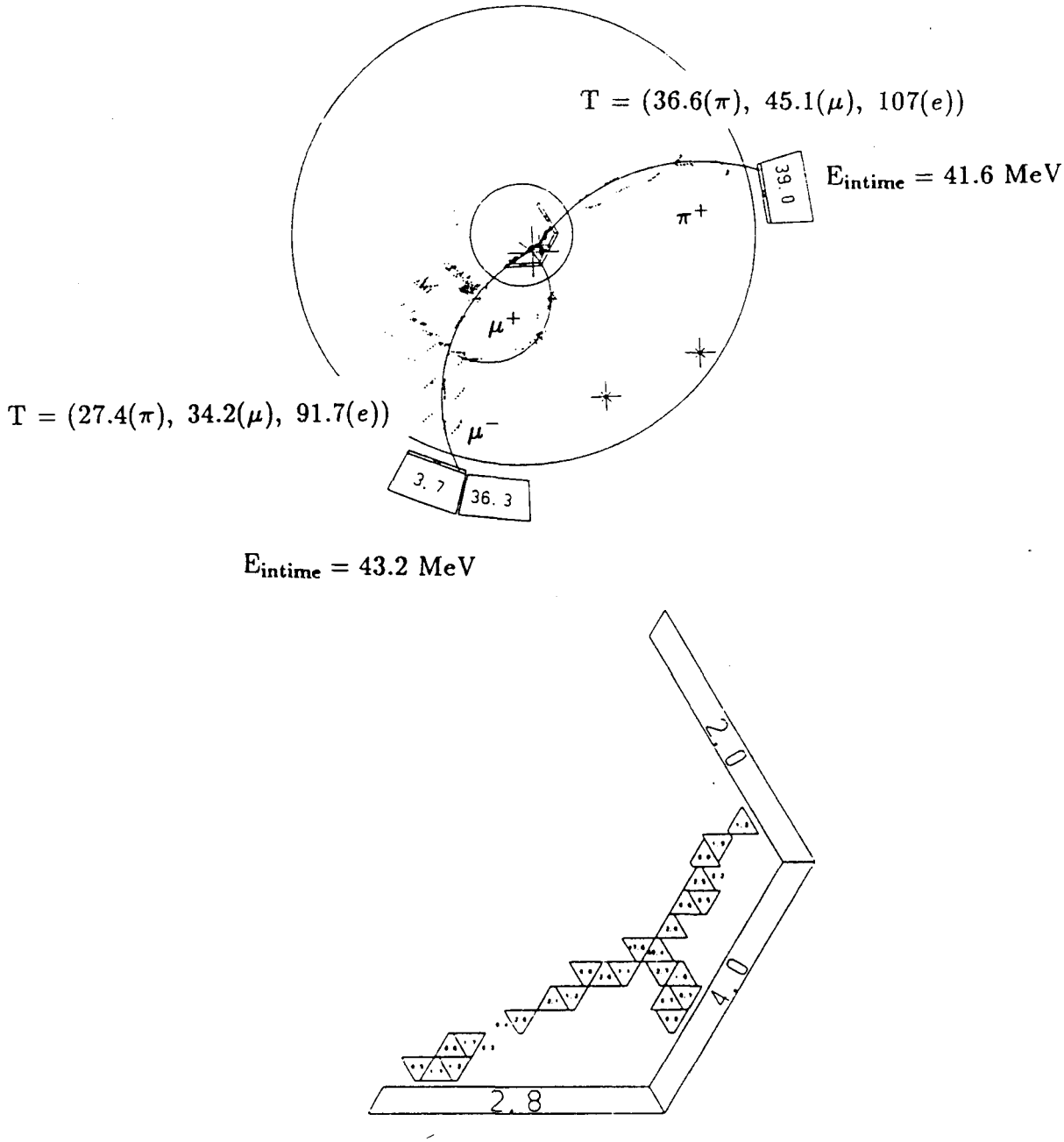

Figure 32. $K^+ \rightarrow \pi^+\mu^+\mu^-$ Candidate #3

4. The Acceptance

4.1 Introduction

As one might expect, deducing the acceptance is by far the most difficult part of the analysis. The final acceptance can be factored into parts as shown in the following table:

Source of inefficiency	How measured
K_{STOP}/K_{Tlive}	Monte Carlo and K_{beam} data
Delayed Coincidence	$K^+ \rightarrow \mu^+\nu$ data
Level 0 trigger	Monte Carlo
Level 1 trigger	Monte Carlo
Pass 0 analysis	Monte Carlo
Pass 1 analysis	Monte Carlo generated data
"Junk" energy cuts	$K^+ \rightarrow \mu^+\nu$ data
Hand scanning	Monte Carlo generated data

Table 1. Factors determining the acceptance, and how they were determined

Examining Table 1, it becomes obvious that one has to rely heavily on Monte Carlo calculations for several key acceptance factors.*

* The difference between *Monte Carlo* and *Monte Carlo generated data* is that in the former case the cuts were applied as the events were simulated, and in the latter case the "fake" events were written to files which were then analysed with the off-line analysis program.

The reason for this is that there are no convenient monitor triggers with the same topology as $K^+ \rightarrow \pi^+\mu^+\mu^-$ that can be used to monitor the efficiencies of the various cuts. Fortunately, $K^+ \rightarrow \pi^+\mu^+\mu^-$ is a straightforward process to simulate.

4.2 The E787 Monte Carlo: UMC

4.2.1 Introduction

The basic idea of the Monte Carlo algorithm is very simple. The program is started with a particle of given 4-momentum and 4-position. The overall trajectory of the particle being composed of many small "steps". During each step, one of three things can happen:

(*i*) The particle can undergo an interaction of some kind. The kinds of interactions that are available depend on the particle type. For instance, a π^+ can undergo a nuclear interaction whereas a μ^+ cannot, although both are subject to scattering. The probability of a given interaction taking place is $\delta x/\mathrm{L}$ (for $\delta x \ll \mathrm{L}$), where δx is the length of the step taken and L is the interaction length for the process in question.

(*ii*) Unless it is stable, the particle can decay. The chance of this happening is simply $\delta \mathrm{t}/\tau$ (for $\delta t \ll \tau$), where τ is the mean life of the particle and δt is the time taken during the step. Particles can decay at rest or in flight.

(*iii*) The particle can continue along its trajectory, depositing an appropriate amount of energy.

The size of the steps are chosen such that the probability of an interaction, other than "normal" energy loss, is small. Occurrences of type *(i)* and *(ii)* can result in the creation of new particles. Any particles created in this way will be worked on, one by one in turn, in the manner described above.

4.2.2 Interactions

It is the completeness and accuracy with which the interactions are accounted for that determine how well the Monte Carlo will simulate real data. Table 6 lists the types of interactions that UMC will allow and the particle types affected.

Type of interaction	Affecting	Comment
Energy loss	Charged particles	Includes the standard contributions, as well as inelastic scattering and Landau tails
Multiple scattering	Charged particles	Small angle as well as Mott scattering
Wire scattering	Charged particles	Only affects particles traversing the drift chamber
Showering	e^+ and e^-	Uses EGS
Nuclear	π's and K's in C	See TN112
Photonuclear	γ's	

Table 6. The types of particle interactions allowed by UMC

4.2.3 The drift chamber simulation

The easiest way to see how the hits in the drift chamber were simulated is to consider Fig. 33. Shown is one of the 256 drift chamber cells. The diagonal dashed lines represent the drift trajectories that electrons (created by a charged track traversing the cell) would follow. These trajectories terminate on sense wires staggered about a plane central to the cell. The time of a sense wire hit in the simulation is simply proportional to the distance from the wire that the track intersected the drift line for that wire.†

A wire will only have a hit if the track intersects its drift line. This is an approximation since under this assumption a track could cross a cell without registering any hits at all, simply by traveling between two drift lines. In the real drift chamber a track traversing the cell parallel to the drift lines would result in many hits, although they would probably not be reconstructible since many hits on only a few wires is difficult for a trackfinding algorithm to interpret.

As is indicated in Table 6, the Monte Carlo also attempts to simulate what happens when a charged particle passes through a drift chamber wire.

† This time is also "smeared" by a gaussian resolution function of appropriate width, $\sigma = 3.5ns$, to simulate electronic jitter and other uncertainties in the timing.

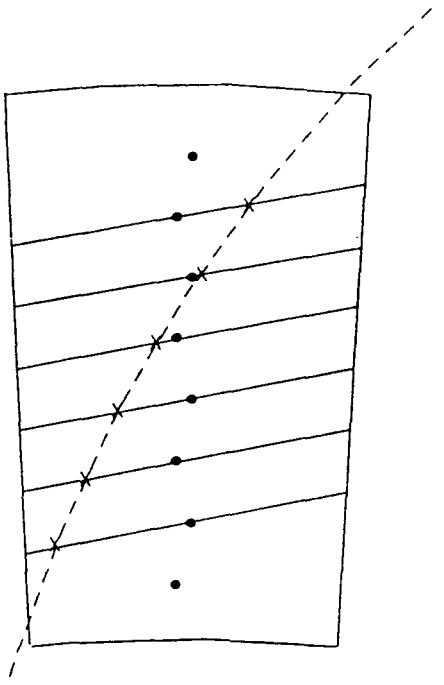

Figure 33. A drift chamber cell as seen by the Monte Carlo. The diagonal lines represent drift trajectories of electrons created by a passing charged track.

4.2.4 The K^+ target stopping distribution

Monte Carlo simulation of $K^+ \rightarrow \pi^+\mu^+\mu^-$ events shows that the majority of events originate from the perimeter of the target. This is understandable in view of the fact that dE/dx of π's and μ's of low momentum can be very high, going roughly as $1/P^2$ for low P. If the decay vertex were at the center of the target, each track would have to penetrate at least 6 cm of scintillator before entering the drift chamber which limits the momenta of the secondaries to a small region of phase space.

This biasing of the decay vertex toward the outside of the target presents a potential problem for the Monte Carlo however, since the acceptance one ultimately obtains will be a fairly strong function of the stopping distribution chosen used in the simulation.

The best way to deal with this uncertainty is to try and measure what the actual stopping distribution was during the runs when the $\pi\mu\mu$ data was accumulated, and to use this as input to the Monte Carlo. To this end, seventy percent (twenty six tapes) of the monitor data accumulated during the running period was analyzed.

The monitor analysis consisted of selecting the K_{beam} trigger events which satisfied the K_T and delayed coincidence trigger requirements, and measuring the K^+ stopping location. The (x,y) location of the vertex was assumed to be at the center of the target fiber with the highest deposited energy. Fig. 34 shows the results of this analysis.

The z stopping distribution was also measured by reconstructing events in the drift chamber whenever possible, and Fig. 35 shows the distribution obtained.

The (x,y) locations were written to an output file, and were used one by one by the Monte Carlo to start individual events. The z distribution used by the Monte Carlo was a gaussian whose mean and standard deviation were obtained from the data shown in Fig. 35.

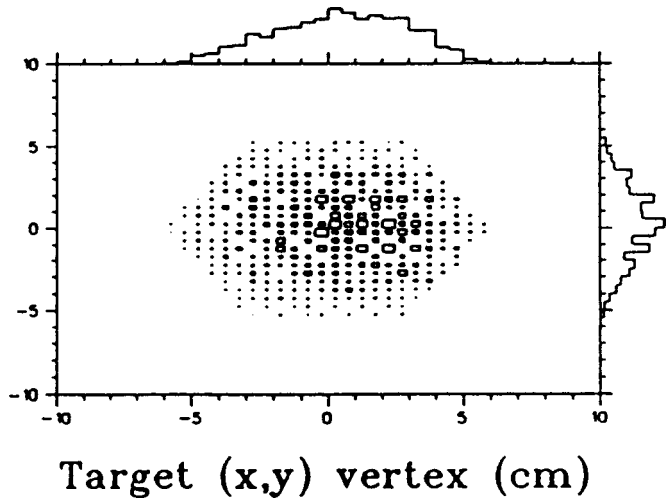

Figure 34. The X-Y location of the K^+ decay vertex as measured using the monitor triggers from 110 $K^+ \to \pi^+\mu^+\mu^-$ runs. The decay vertex was assumed to be at the center of the target fiber with the highest deposited energy.

4.2.5 More about the $K^+ \to \pi^+\mu^+\mu^-$ Monte Carlo

Some final remarks should be made regarding the $\pi\mu\mu$ simulation before presenting the results.

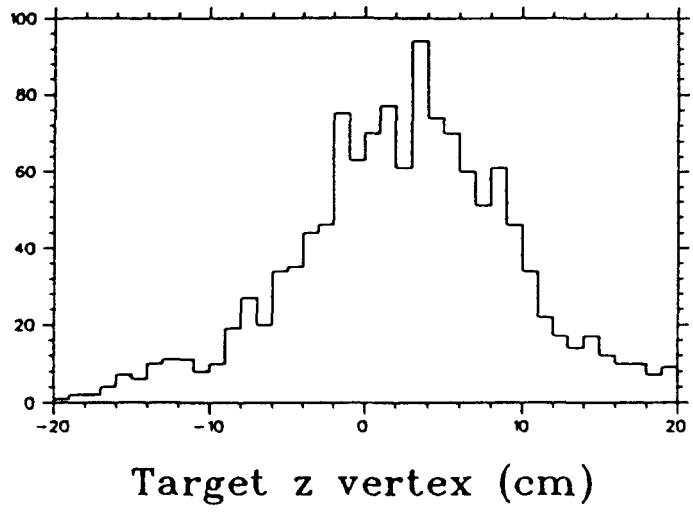

Figure 35. The Z location of the K^+ decay vertex as measured using the monitor triggers from 110 $K^+ \rightarrow \pi^+\mu^+\mu^-$ runs. The Z location was obtained by extrapolating the best fit drift chamber track back into the target. Only events that that had a drift chamber track with a z-fit were considered.

- The matrix element was assumed to be unity, the $\pi\mu\mu$ distributions being determined using phase space alone. This was a conscious decision made after examining the calculations done in reference[14].*
- Some types of particles are more difficult to Monte Carlo by virtue of the interactions they undergo. For example, electrons undergo electromagnetic showers which can spatially extend over the entire detector. Although this is in principle properly taken into account by UMC, it is nevertheless a more complicated and time consuming task to simulate an e^+ than a μ^+. Similarly, a π^- will be captured by a nucleus promptly upon stopping, resulting in a complicated distribution of neutrons and charged fragments, and this is *not* handled realistically in the Monte Carlo (yet). Since $K^+ \rightarrow \pi^+\mu^+\mu^-$ involves neither a $e^\pm$ or a π^-, it is more reliably simulated than other modes like $K^+ \rightarrow \pi^+\pi^-e^+\nu$.

* This is discussed in the introduction.

4.3 THE $K^+ \to \pi^+\mu^+\mu^-$ ACCEPTANCE

4.3.1 Factors obtained from data

Factor	Measured
$\mathcal{E}_{\rm DC}$	$0.83 \pm 0.01\,stat \pm 0.02\,syst$
$\mathcal{E}_{\rm intime}$	$0.85 \pm 0.01\,stat \pm 0.01\,syst$
$\mathcal{E}_{\rm KT}$	$0.86 \pm 0.01\,stat \pm 0.03\,syst$
$\mathcal{E}_{\rm TGjunk}$	$0.94 \pm 0.02\,stat \pm 0.05\,syst$

Table 3. Acceptance factors measured from data.

- $\mathcal{E}_{\rm DC}$: The efficiency of the delayed coincidence cut was deduced by examining kinematically* selected $K^+ \to \mu^+\nu$ events, and counting how many had the delayed coincidence bit set on the trigger bus.
- $\mathcal{E}_{\rm intime}$: The inefficiency of the in-time energy cut depends both on the threshold used and on the width of the prompt window. It was also found to scale linearly with beam intensity, which indicates that it is largely due to random vetoing by "other" events. The value shown is Table 3 reflects an average beam intensity of 150,000 K_T's per spill and assumes a 1 MeV veto threshold for each of the E_{RS}^{junk}, E_{BV} and E_{EC} cuts with a 20 ns prompt window half-width. It was obtained by looking at kinematically selected $K^+ \to \mu^+\nu$ events, which should in principle have no in-time extra energy, and counting how many failed the above cuts.
- $\mathcal{E}_{\rm KT}$: This is a correction factor which must be applied to the measured quantity $K_{T\,live}$ to obtain the actual number of K^+'s which stopped in the fiducial volume of the target while the detector was *live*. The main sources of "false" K_T's were kaons decaying in flight in the degrader in such a way that the decay product(s) satisfied the K_T requirement, and kaons leaving the target before stopping. The overall factor was deduced using a combination of Monte Carlo beam studies and real K_{beam} data.

* The kinematic selection was done by demanding the event have a momentum energy correlation appropriate for $K^+ \to \mu^+\nu$. This was defined as $220 \le P \le 248$ (MeV/c) and $136 \le E \le 152$ (MeV/c).

- $\mathcal{E}_{\text{TGjunk}}$: The E^{tg}_{junk} cut will tend to veto events where more than one beam particle entered the target during the ADC gate. The efficiency of this cut was measured by recording the E^{tg}_{junk} spectrum of kinematically selected $K^+ \rightarrow \mu^+\nu$ events.

4.3.2 Factors obtained from Monte Carlo

The Monte Carlo was used to generate 100,000 $K^+ \rightarrow \pi^+\mu^+\mu^-$ events. The effects of the trigger and the pass 0 analysis the on these events was simulated, and the results are summarized in Table 8 and Table 9.

# Events Entering Level 0		96,821
Requirement	**Events Lost**	**Events Remaining**
Any T · A	44,679	52,136
2 or 3 T · A's	35,216	16,920
$E_{BV} \leq 5$ MeV	45	16,875
I-C hit	414	16,461
No V-C hit	587	15,874
$E_{EC} \leq 10$ MeV	6	15,868
L0 Range $\leq$ Layer C	840	15,028
$\overline{RS(19+20+21)}$	15	15,013
Level 0 Efficiency		0.155
$N_{TG} \geq 20$	1,777	13,236
Level 1 Efficiency		0.882
Net Trigger Efficiency		0.137

Table 8. The $K^+ \rightarrow \pi^+\mu^+\mu^-$ trigger efficiency as calculated by Monte Carlo

The events that passed the trigger and pass 0 cuts simulated in the monte carlo were written to output files having the same bank structure as the real data tapes.

# Events Entering Pass 0		13,236
Requirement	**Events Lost**	**Events Remaining**
$N_{IC} \geq 2$	162	13,074
IC pattern	772	12,302
$E_{RS}(tot) \leq 175$ MeV	10	12,292
$E_{RS}(11 \rightarrow 21) \leq 4$ MeV	233	12,059
Pass 0 Efficiency		0.911

Table 9. The $K^+ \rightarrow \pi^+\mu^+\mu^-$ Pass 0 efficiency as calculated by Monte Carlo

These events were, for the purpose of the pass 2 analysis, authentic $\pi\mu\mu$ events having been detected, processed and saved in the same way as any other data taken during the run. The pass 2 reconstruction algorithm, as described in the previous chapter, was run on these events in order to deduce the pass 2 analysis efficiency. The results are presented in Table 10. The pass 1 analysis was not run on the data first, since pass 1 is equivalent to pass 2 with looser cuts.

Events entering Pass 2		12,059
D^2_{vtx}	$\leq 5\,cm^2$	
P_{xy}	$\leq 60\,MeV/c$	
Events passing inner loop		804
Parameter	Constraint	# Remaining
R_{vtx}	$\leq 2\,cm$	804
RS_{match}	≥ 2	796
N_{RS}	≤ 5	794
E_{BV}	$\leq 1\,MeV$	793
P_{xy}	$\leq 40\,MeV/c$	748
θ_{min}	$\geq 20^o$	734
D^2_{vtx}	$\leq 3\,cm$	727
E^{tg}_{junk}	$\leq 20\,MeV$	727
E^{ic}_{pmin}	$\geq 2\,MeV$	725
N_{TG}	≥ 20	723
P^{max}_{xy}	$\leq 150\,Mev/c$	723
IC_{match}	TRUE	718
E^{track}_{RS}	$\leq 120\,MeV$	715
E^{junk}_{RS}	$\leq 1\,MeV$	664
E_{EC}	$\leq 1\,MeV$	655
Pass 2 Efficiency		0.054

Table 10. Constraints imposed on the various selection parameters by the pass 2 analysis, and the number of events surviving each cut, applied in the order shown to Monte Carlo $K^+ \rightarrow \pi^+\mu^+\mu^-$ data passing simulated trigger and pass 0 cuts.

4.3.3 Drift chamber reconstruction efficiency

The $\pi\mu\mu$ analysis depends heavily on drift chamber information, hence the ability of the Monte Carlo to accurately simulate drift chamber data is essential to the acceptance calculation.

The track reconstruction efficiency for both real and simulated data was deduced by hand-scanning events of both types, which had *not* been subjected to any software drift chamber cuts. Only low momentum tracks not reaching the range stack were considered.*

The results are shown below:

Data	# Scanned	# Reconstructed	Efficiency
Real	44	41	.93 ± .2
MC	41	37	.90 ± .2

There is good agreement, although the errors are large.† Based on this result, we will assume that the Monte Carlo adequately reproduced track reconstruction inefficiency.

4.3.4 Final $K^+ \to \pi^+\mu^+\mu^-$ acceptance

We are now ready to combine the various factors described in the previous sections to form the *final* acceptance for $K^+ \to \pi^+\mu^+\mu^-$. Table 11 shows the result of this exercise.

The individual efficiencies obtained from Monte Carlo, ($\mathcal{E}_{\rm L0}$, $\mathcal{E}_{\rm L1}$, $\mathcal{E}_{\rm Pass0}$, and $\mathcal{E}_{\rm Pass2}$), were combined into a single factor: $\mathcal{E}_{\rm MC}$.

The factor $\mathcal{E}_{\rm hand}$ is the efficiency of the hand-scan cuts $\rm IC_{plus}$ and $\rm TG_{\Delta T}$, estimated by hand-scanning Monte Carlo events.

⋆ It was previously found that the fitting routines used in the $\pi\mu\mu$ analysis are ~ 100% efficient for high momentum tracks.

† It is quite uncommon for "raw" $K^+ \to \pi^+\mu^+\mu^-$ data to contain low momentum tracks, hence hundreds of events had to be scanned to obtain the above numbers.

Factor	Acceptance
$\mathcal{E}_{\mathrm{DC}}$	$0.83 \pm 0.01\,stat \pm 0.02\,syst$
$\mathcal{E}_{\mathrm{intime}}$	$0.85 \pm 0.01\,stat \pm 0.01\,syst$
$\mathcal{E}_{\mathrm{KT}}$	$0.86 \pm 0.01\,stat \pm 0.03\,syst$
$\mathcal{E}_{\mathrm{TGjunk}}$	$0.94 \pm 0.02\,stat \pm 0.05\,syst$
$\mathcal{E}_{\mathrm{MC}}$	$(6.77 \pm 0.3\,stat \pm 1.3\,syst) \times 10^{-3}$
$\mathcal{E}_{\mathrm{hand}}$	$0.89 \pm 0.07\,stat \pm 0.01\,syst$
$\mathcal{E}_{\mathrm{TOTAL}}$	$(3.4 \pm 0.3\,stat \pm 0.7\,syst) \times 10^{-3}$

Table 11. The total detection efficiency for $K^+ \to \pi^+\mu^+\mu^-$.

4.4 THE $K^+ \to \mu^+\nu\mu^+\mu^-$ ACCEPTANCE

The method for determining the acceptance for this decay mode, like the others, involves the generation of Monte Carlo events that are then analyzed as if they were real data. As for the case of $\pi\mu\mu$, the events were generated using pure phase space to determine the four-momenta of the secondaries. The analysis parameters used in pass 2 were the same as those used for $\pi\mu\mu$. The results are summarized in Table 12.

The events which must be considered as candidates for this decay mode are the same ones found in the $K^+ \to \pi^+\mu^+\mu^-$ analysis, since they cannot reliably be differentiated.* This also means that the $K^+ \to \mu^+\nu\mu^+\mu^-$ efficiency is subject to the hand-scan efficiency factor $\mathcal{E}_{\rm hand}$.

Factor	Acceptance
$\mathcal{E}_{\rm DC}$	$0.83 \pm 0.01\,stat \pm 0.02\,syst$
$\mathcal{E}_{\rm intime}$	$0.85 \pm 0.01\,stat \pm 0.01\,syst$
$\mathcal{E}_{\rm KT}$	$0.86 \pm 0.01\,stat \pm 0.03\,syst$
$\mathcal{E}_{\rm TGjunk}$	$0.94 \pm 0.02\,stat \pm 0.05\,syst$
$\mathcal{E}_{\rm MC}$	$(3.69 \pm 0.3\,stat \pm 0.7\,syst) \times 10^{-3}$
$\mathcal{E}_{\rm hand}$	$0.89 \pm 0.07\,stat \pm 0.01\,syst$
$\mathcal{E}_{\rm TOTAL}$	$(1.9 \pm 0.2\,stat \pm 0.4\,syst) \times 10^{-3}$

Table 12. The total detection efficiency for $K^+ \to \mu^+\nu\mu^+\mu^-$ using the same selection parameters as in the $K^+ \to \pi^+\mu^+\mu^-$ analysis.

* The key to differentiating between $K^+ \to \pi^+\mu^+\mu^-$ and $K^+ \to \mu^+\nu\mu^+\mu^-$ lies in the ability to distinguish π^+ from μ^+ in the range stack. This is not reliably done with a momentum-energy correlation alone, and requires the inner range stack layers to be instrumented with transient recorders. (The power of using transient recorders for particle identification is discussed in chapter 2).

4.5 THE $K^+ \to \pi^+ H$; $H \to \mu^+\mu^-$ ACCEPTANCE

The process $K^+ \to \pi^+ H$; $H \to \mu^+\mu^-$ was simulated for eight higgs masses in the range $225\,MeV \leq M_H \leq 320\,MeV$. The resulting values of $\mathcal{E}_{\rm MC}$ were combined with $\mathcal{E}_{\rm DC}$, $\mathcal{E}_{\rm intime}$, $\mathcal{E}_{\rm KT}$, $\mathcal{E}_{\rm TGjunk}$, and $\mathcal{E}_{\rm hand}$, to yield the total acceptance as a function of M_H. The results are summarized in Fig. 36.

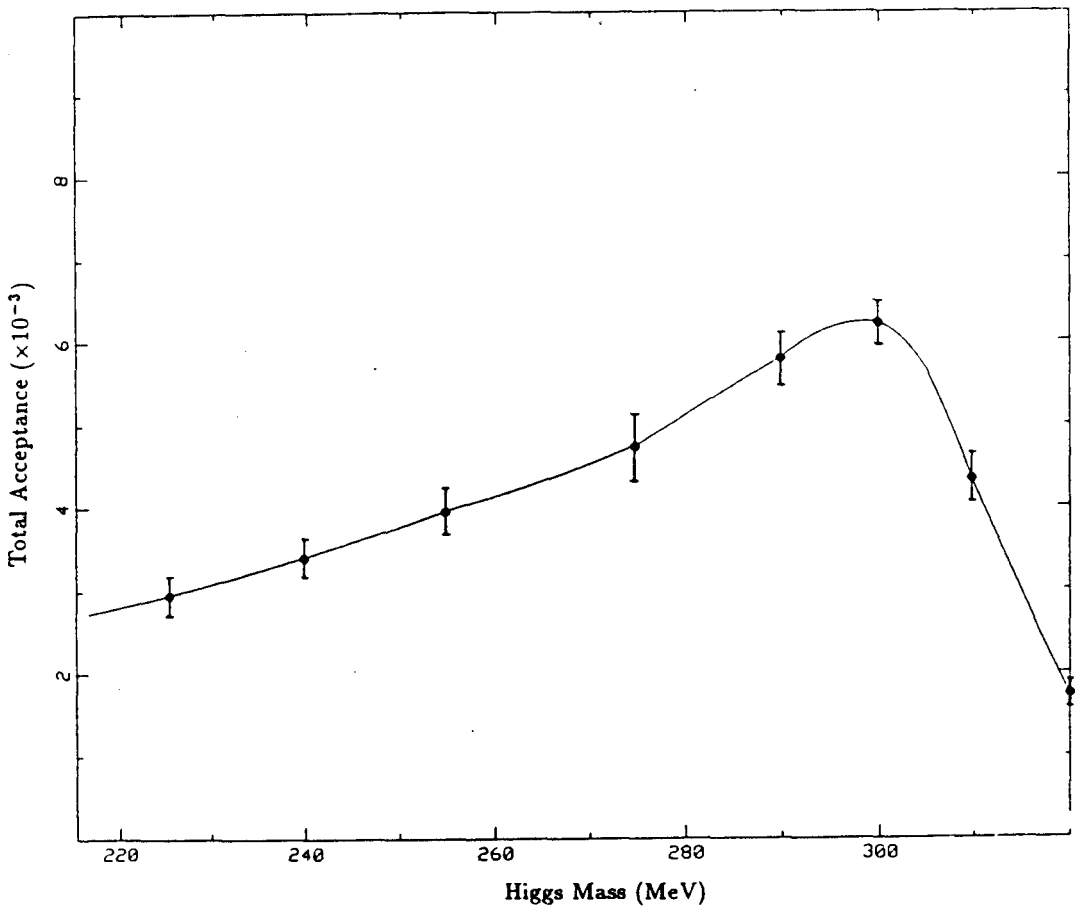

Figure 36. The total detection efficiency for $K^+ \to \pi^+ H$, $H \to \mu^+\mu^-$, as a function of M_H, using the same selection parameters as in the $K^+ \to \pi^+\mu^+\mu^-$ analysis. The eight data points represent values of M_H simulated by the Monte Carlo, (error bars are statistical). The solid line connecting the points is a quadratic interpolation.

5. The Background

5.1 Introduction

The backgrounds for any process must be understood before any claims can be made regarding its observation.*

We know of one particular decay mode, $K^+ \to \pi^+\pi^-e^+\nu$, whose signature in the detector is very similar to $K^+ \to \pi^+\mu^+\mu^-$. These events have been identified in our data sample, and Fig. 37 shows two of a set of over fifty such candidates.† The very similar decay mode $K^+ \to \pi^+\pi^-\mu^+\nu$ may also be a possible background.

There may also be other background processes due to more common decay channels like $K^+ \to \pi^+\pi^+\pi^-$ or $K^+ \to \pi^+\pi^0$ with $\pi^0 \to \gamma e^+e^-$. These do not normally produce three track events in the E787 detector that look like bona fide $\pi\mu\mu$ candidates, but at the level of 1 in 10^7 almost anything is possible.

All of the above decay modes are examined in this chapter.

5.2 The $K^+ \to \pi^+\pi^-e^+\nu$ background

The most important similarity between $K^+ \to \pi^+\pi^-e^+\nu$ and $K^+ \to \pi^+\mu^+\mu^-$ is the track topology: Most events have two tracks reaching the range stack and one spiraling in the drift chamber, with the minimum opening angle between any two tracks tending to be large. As far as the drift chamber is concerned, this is the same track signature as a $\pi\mu\mu$ event, and, as such, should have a similar reconstruction

* Since the $\pi\mu\mu$ analysis will result in an upper limit rather than in a branching ratio, we strictly speaking do not need to worry at all about any background effects. It is however useful to consider the possibilities.

† These were selected by a set of cuts which will be described later in this chapter.

efficiency. For this reason it is of special interest since the ability to predict the number of such events found would give us confidence that the Monte Carlo is working properly.

Monte Carlo generated $K^+ \rightarrow \pi^+\pi^-e^+\nu$ events were analyzed using the same parameters as were used in the $K^+ \rightarrow \pi^+\mu^+\mu^-$ analysis. In this way, the detection efficiency for $\pi\pi e\nu$ was determined. The main difference in efficiency is due to the pass 2 analysis. Table 13 shows how each of the pass 2 cuts affected the Monte Carlo generated $\pi\pi e\nu$ events, and a summary of results is presented in Table 14. Notice that the factors $\mathcal{E}_{\rm KT}$ and $\mathcal{E}_{\rm DC}$ are the same as for $\pi\mu\mu$, the reason being that these quantities reflect hardware that was common to both triggers.

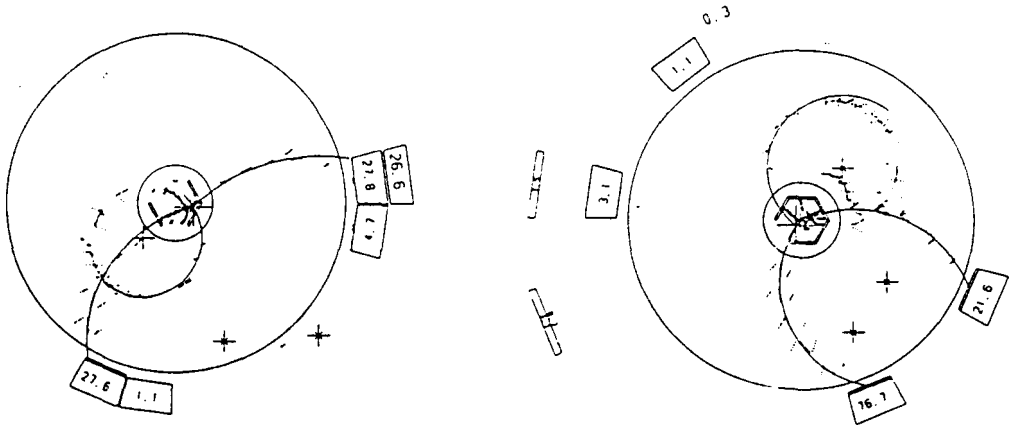

Figure 37. Two $K^+ \rightarrow \pi^+\pi^-e^+\nu$ candidates. These are two of a sample of fifty such events selected by software and well defined hand-scanning.

Having this efficiency we can predict the number of $\pi\pi e\nu$ events we should observe in the final $\pi\mu\mu$ sample:

$$\begin{aligned} N_{\pi\pi e\nu} &= \text{Acceptance} \times \text{Exposure} \times \text{Branching Ratio[31]} \\ &= (2.4 \pm 0.8 \pm 0.5 \times 10^{-5}) \times (0.96 \times 10^{10}) \times (3.90 \pm 0.15 \times 10^{-5}) \\ &\sim 9 \pm 3 \,\text{Events} \end{aligned}$$

Events entering Pass 2		3079.
D^2_{vtx}	$\leq 5\,cm^2$	
P_{xy}	$\leq 60\,MeV/c$	
Events passing inner loop		192
Parameter	Constraint	# Remaining
R_{vtx}	$\leq 2\,cm$	190
RS_{match}	≥ 2	178
N_{RS}	≤ 5	157
E_{BV}	$\leq 1\,MeV$	131
P_{xy}	$\leq 40\,MeV/c$	81
θ_{min}	$\geq 20^o$	76
D^2_{vtx}	$\leq 3\,cm$	75
E^{tg}_{junk}	$\leq 20\,MeV$	73
E^{ic}_{pmin}	$\geq 2\,MeV$	64
N_{TG}	≥ 20	64
P^{max}_{xy}	$\leq 150\,Mev/c$	64
IC_{match}	TRUE	46
E^{track}_{RS}	$\leq 120\,MeV$	44
E^{junk}_{RS}	$\leq 1\,MeV$	25
E_{EC}	$\leq 1\,MeV$	11
Pass 2 Efficiency		3.6×10^{-3}

Table 13. The effect of the pass 2 $\pi\mu\mu$ selection cuts on Monte Carlo $K^+ \rightarrow \pi^+\pi^-e^+\nu$ data.

When hand-scanning the final $\pi\mu\mu$ sample we found 2 ± 1 events consistent with being $\pi\pi e\nu$.

The number observed is less than the number predicted. However, there is a reason to expect this. As was mentioned in the previous chapter, the monte carlo

Factor	Acceptance
$\mathcal{E}_{\rm DC}$	$0.83 \pm 0.01\,stat \pm 0.02\,syst$
$\mathcal{E}_{\rm intime}$	$0.85 \pm 0.01\,stat \pm 0.01\,syst$
$\mathcal{E}_{\rm KT}$	$0.86 \pm 0.01\,stat \pm 0.03\,syst$
$\mathcal{E}_{\rm TGjunk}$	$0.94 \pm 0.02\,stat \pm 0.05\,syst$
$\mathcal{E}_{\rm MC}$	$(4.2 \pm 1.4\,stat \pm 0.8\,syst) \times 10^{-5}$
$\mathcal{E}_{\rm TOTAL}$	$(2.4 \pm 0.8\,stat \pm 0.5\,syst) \times 10^{-5}$

Table 14. The total detection efficiency for $K^+ \to \pi^+\pi^-e^+\nu$ using the same selection parameters as in the $K^+ \to \pi^+\mu^+\mu^-$ analysis.

does not take π^-'s properly into account. In the simulation, when a π^- stops it is assumed to interact immediately, and in so doing deposit a random fraction of its mass as visible energy in the stopping counter. This agrees partly with reality, since on average one proton and one alpha are released per captured π^-[32]. The average kinetic energies of the p and α are 17 MeV and 7 MeV respectively, hence their ranges are negligible and the energy will end up in the stopping counter.

What is *not* included in the Monte Carlo is that, on average, 2.8 neutrons will also be released with an mean shared kinetic energy of 68 MeV. Any of these neutrons can cause an event to be vetoed by depositing some of its energy, within a time window of 20 ns, in a part of the detector in which no energy is expected. In the case of the $K^+ \to \pi^+\mu^+\mu^-$ pass 2 analysis, very tight "junk energy" cuts were imposed in the RS, BV and EC.

The statistical error on the above numbers is great, as is the uncertainty due to π^- vetoing. In an attempt to reduce both of these unknowns, a special $\pi\pi e\nu$ analysis was performed. It was hoped that by relaxing cuts that veto events based on extra energy, the π^- uncertainty would be reduced. This should also select a larger sample of $K^+ \to \pi^+\pi^-e^+\nu$, both for Monte Carlo and real data, reducing the statistical errors.

The values of these new cuts and their effect on the pass 2 acceptance for Monte Carlo $\pi\pi e\nu$ events can be seen in Table 15. The changed parameters are denoted by a $(*)$.

Events entering Pass 2		3079
D^2_{vtx}	$\leq 5\,cm^2$	
P_{xy}	$\leq 60\,MeV/c$	
Events passing inner loop		192
Parameter	Constraint	# Remaining
R_{vtx}	$\leq 2\,cm$	190
RS_{match}	≥ 2	178
N_{RS}	≤ 10 (*)	178
E_{BV}	$\leq 2\,MeV$ (*)	162
P_{xy}	$\leq 40\,MeV/c$	106
θ_{min}	$\geq 45^o$ (*)	88
D^2_{vtx}	$\leq 3\,cm$	87
E^{tg}_{junk}	$\leq 20\,MeV$	85
E^{ic}_{pmin}	none (*)	85
N_{TG}	≥ 20	85
P^{max}_{xy}	$\leq 150\,Mev/c$	83
IC_{match}	TRUE	58
E^{track}_{RS}	none (*)	58
E^{junk}_{RS}	none (*)	58
E_{EC}	none (*)	58
Pass 2 Efficiency		1.88×10^{-2}

Table 15. The effect of the $\pi\pi e\nu$ selection cuts on $\pi\pi e\nu$ Monte Carlo data.

If we use this new value for the pass 2 $\pi\pi e\nu$ efficiency, we arrive at the following prediction for the number of events we should observe:

$$\begin{aligned} N_{\pi\pi e\nu} &= \text{Acceptance} \times \text{Exposure} \times \text{Branching Ratio} \\ &= (1.3 \pm 0.2 \pm 0.2 \times 10^{-4}) \times (0.96 \times 10^{10}) \times (3.90 \pm 0.15 \times 10^{-5}) \\ &\sim 49 \pm 10 \text{ Events} \end{aligned}$$

When the selection cuts listed in Table 15 were applied to the real data, the resulting number of passing events was 78. These were then examined by hand and sorted into three categories.

(*i*) Good $\pi\pi e\nu$ (37): Events that looked exactly like the Monte Carlo carlo generated $\pi\pi e\nu$ candidates passing the same cuts.

(*ii*) Poor $\pi\pi e\nu$ (8): Events that did not look as good as those in category *(i)*, but could not be ruled out as candidates.

(*iii*) Not $\pi\pi e\nu$ (33): Events that looked nothing like category *(i)*.

Fig. 38 shows the reconstructed mass of the $\pi\pi e\nu$ candidates in category (*i*), and the Monte Carlo $\pi\pi e\nu$ candidates passing the same cuts. The events were reconstructed in the $x - y$ plane only.

We will consider the events is category *(i)* to be good $\pi\pi e\nu$ candidates and those in category *(ii)* to be an indication of the systematic error in our procedure, obtaining:

$$N_{\text{observed}} = 37 \pm 6 \pm 8$$

Even with the selection cuts loose, we expect the π^- to veto a noticeable fraction of the real $K^+ \to \pi^+\pi^- e^+\nu$ events, *i.e.* we would expect the number of $\pi\pi e\nu$ events predicted by Monte Carlo to be higher than the number observed. The above numbers are consistent with this hypothesis, but the error bars are too large to make a quantitative conclusion.

A sample of $K^0_S \to \pi^+\pi^-$ events, acquired using a special charge exchange trigger, were examined to try and estimate the fraction of $K^+ \to \pi^+\pi^- e^+\nu$ events that the π^- will veto. An extremely crude analysis indicated that between 20% and 40% would have been rejected in the pass 0 analysis based on extra range stack energy alone, although it is difficult to argue that these numbers should be used for anything more than a compelling argument to improve the Monte Carlo.

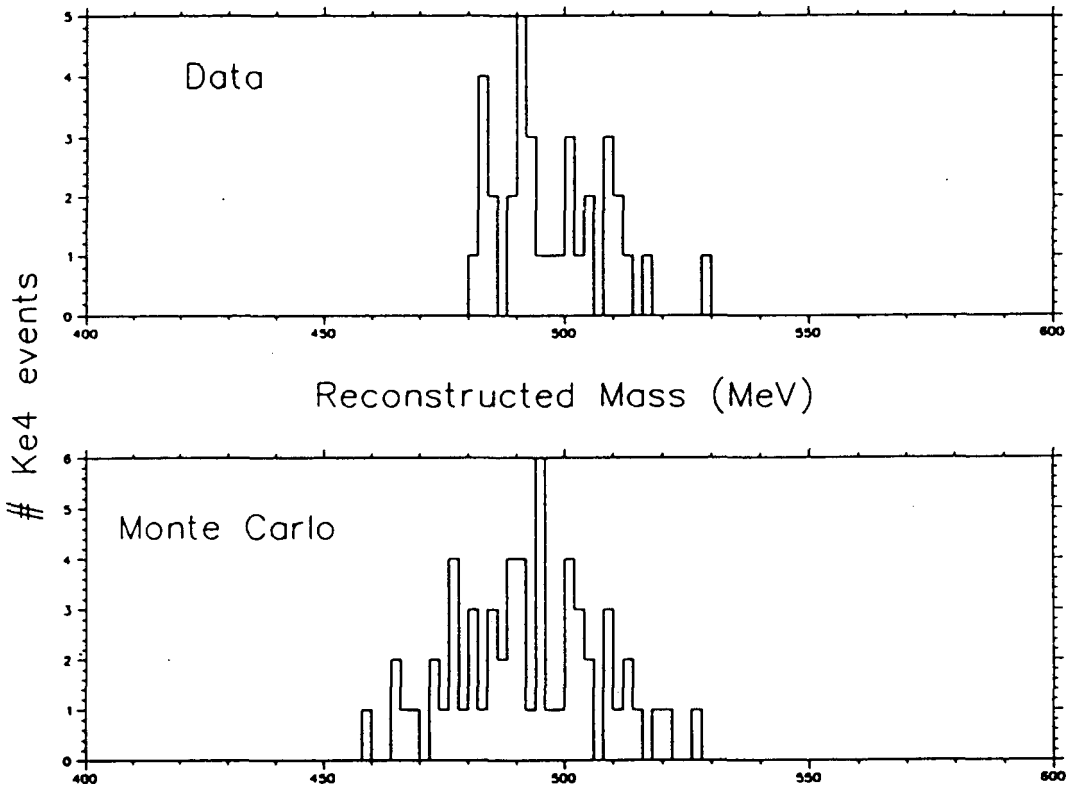

Figure 38. Mass plots for $K^+ \to \pi^+\pi^-e^+\nu$ events selected by the same criteria from data (top) and Monte Carlo (bottom). The reconstruction was done in the $x - y$ plane only.

5.3 THE $K^+ \to \pi^+\pi^-\mu^+\nu$ BACKGROUND

To study the acceptance for $K^+ \to \pi^+\pi^-\mu^+\nu$, 109784 such events were generated by the Monte Carlo. None of these events had three reconstructible tracks in the drift chamber.* We can therefore set an upper limit on the product of the acceptance factors obtained by Monte Carlo:

$$\mathcal{E}_{\rm MC} \leq 2.1 \times 10^{-5} \ (90\% \ {\rm CL})$$

Multiplying by the other factors $\mathcal{E}_{\rm DC}$, $\mathcal{E}_{\rm KT}$, $\mathcal{E}_{\rm intime}$, $\mathcal{E}_{\rm TGjunk}$, and $\mathcal{E}_{\rm hand}$, we get the total efficiency for detecting $K^+ \to \pi^+\pi^-\mu^+\nu$ in the final $\pi\mu\mu$ sample.

$$\mathcal{E}_{\rm TOTAL} \leq 1.1 \times 10^{-5}$$

We have already learned by studying $K^+ \to \pi^+\pi^-e^+\nu$ that the efficiency calculated by Monte Carlo will be too high because the π^- is not properly simulated. (Recall, the Monte Carlo predicted we should see 9 ± 3 $\pi\pi e\nu$ events in the final $\pi\mu\mu$ sample, and the actual number seen was 2 ± 1). Based on this previous observation, we will reduce the above acceptance by a further conservative factor of 2 to take into account the π^- vetoing:

$$\mathcal{E}_{\rm TOTAL} \leq 0.55 \times 10^{-5}$$

Using this to predict the number if $\pi\pi\mu\nu$ events to expect in the final sample we obtain:

$$\begin{aligned} &{\rm N}_{\pi\pi\mu\nu} = {\rm Acceptance} \times {\rm Exposure} \times {\rm Branching\,Ratio} \\ &\leq (0.55 \times 10^{-5}) \times (0.96 \times 10^{10}) \times (1.4 \pm 0.15 \times 10^{-5}) \\ &\leq 0.7\,{\rm Events} \end{aligned}$$

If $K^+ \to \pi^+\pi^-\mu^+\nu$ events were present in the data, they should be easy to distinguish since their reconstructed mass will be at least 30 MeV below the K^+ mass. The reason for this mass difference is threefold:

* The low Q value, 109 MeV, makes it extremely unlikely that all three charged particles will escape the target with enough energy to satisfy the three-track requirement in the drift chamber.

(*i*) The π^+ is assigned the mass of a μ^+ by the reconstruction algorithm. If $P = 100$ MeV/c, the difference in total energy between a π and a μ is 27 MeV.

(*ii*) Assigning the π^+ track a μ^+ mass also causes dE/dx in the target to be underestimated, lowering the extrapolated vertex momentum.

(*iii*) The ν energy is lost.

No events having a low reconstructed mass were seen in the final $\pi\mu\mu$ sample.

5.4 THE $K^+ \to \pi^+\pi^+\pi^-$ BACKGROUND

We will consider the decay $K^+ \to \pi^+\pi^+\pi^-$ as presenting four distinct background components. These are the cases where none, one, two, or three of the pions decay in flight, and will be discussed separately below.

It should be pointed out that the first three cases will result in reconstructed mass distributions that are centered at least 30 MeV below the kaon mass. Since the mass resolution is ≤ 7 MeV, any background events would have to come from the tails of these peaks, at the 4σ level.

$\to$ There is *no* indication of any low mass distributions in the data.

Presented below are arguments why the areas of the potential background peaks should be very small.

• $K^+ \to \pi^+\pi^+\pi^-$, *none* of the π's decaying in flight:

This component can be ruled out as a background for two reasons:

(*i*) From kinematic arguments, it is highly improbable for these events can satisfy the trigger and still have three reconstructible tracks in the drift chamber, two of which must reach the range stack. This is simply because the Q value for $K^+ \to \pi^+\pi^+\pi^-$ is a very modest 75 MeV, and the range of a low energy π is small enough that the probability of all three π's escaping the target, while satisfying the level 1 trigger requirement that at least 20 target elements be hit, is minute. If all three π's *do* escape the target, two of them must have at least 65 MeV/c momentum in order to reach the range stack, while the third must have a minimum momentum of 30 MeV/c in order to reach layer three of the drift chamber. These requirements make the process even less likely.

(*ii*) If events in this category *were* able to satisfy the cuts, their reconstructed mass spectrum would peak at least 60 MeV below the kaon mass. We see *no* such events in the data.

• $K^+ \to \pi^+\pi^+\pi^-$, *one* of the π's decaying in flight:

If a π decays in flight, the resulting μ can have a boosted momentum, provided it comes out in the "forward" direction. The μ has the additional advantage of having a lower dE/dx than a π of the same momentum, and will therefore have a higher probability of escaping the target. Clearly, the π has to decay before it loses too much energy in order to optimize the μ's chances of escape. If we demand that one of the π's has to decay within 3 cm of the K^+ vertex, the effective $K^+ \to \pi^+\pi^+\pi^-$ branching ratio is reduced by a factor of 7.7×10^{-3}.* The choice of 3 cm is very conservative for several reasons:

— If the π's evenly share the 74.9 MeV of available kinetic energy, each will have a momentum of 87 MeV/c. The range of an 87 MeV/c π is less than 3.5 cm, and falls quickly with momentum. (The range of an 80 MeV/c π is about 2.5 cm).

— Since dE/dx for a π can be much higher than for a μ of the same momentum, (the difference is over 2 MeV/cm at a momentum of 70 MeV/c), the reconstructed mass will be shifted down by a potentially large amount, which is roughly proportional to the energy lost by the π before it decays.

— Unless the μ direction of motion is exactly collinear with the π, the μ track will not point back to the K^+ decay vertex. If the π decays far from the K^+ vertex, the potential for a badly reconstructed vertex is high due to the longer "lever arm".

We will also ask that the angle the μ makes with the axis defined by the π direction of motion be no more than 60° in the π rest frame. Outside this region, the boost given the μ is relatively small, and the energy lost to the ν is larger. This is angle defines 1/4 of the solid angle.

The effective branching ratio for $K^+ \to \pi^+\pi^+\pi^-$ under these constraints becomes 1.1×10^{-4}.

If we assume that the acceptance for events of this type is the same as that found above for $K^+ \to \pi^+\pi^-\mu^+\nu$, we find the number of expected events to be:

$$N \leq (0.55 \times 10^{-5}) \times (0.96 \times 10^{10}) \times (1.1 \times 10^{-4})$$

$$\leq 6 \text{ Events}$$

The reconstructed mass of these events, using the same arguments as for $K^+ \to \pi^+\pi^-\mu^+\nu$, will be at least 45 MeV below the kaon mass.† Since the mass resolution

---

* The average kinetic energy of a π from $K^+ \to \pi^+\pi^+\pi^-$ is 25 MeV, having $\beta \sim .5$, which is equivalent to a velocity 15 cm/ns. It therefore travels 3 cm in 3/15 ns, and the probability of decaying in this time, $\delta t/\tau$, is $3/(15 \times 26) = 7.7 \times 10^{-3}$.

† The ν is guaranteed to carry away *at least* 15 MeV.

is $\sim$ 7 MeV, this channel would not be a serious background even if the expected number of events was an order of magnitude higher.

• $K^+ \to \pi^+\pi^+\pi^-$, *two* of the π's decaying in flight:

If we use the same argument as above, demanding that both π's decay within 3 cm of the K^+ vertex, no more than 60° away from the π axis, the effective $K^+ \to \pi^+\pi^+\pi^-$ branching ratio becomes 2.1×10^{-7}. If we assume the acceptance is less than or equal to the acceptance for $K^+ \to \pi^+\mu^+\mu^-$,‡ then the number of events we expect is:

$$N \leq 0.0034 \times (0.96 \times 10^{10}) \times (2.1 \times 10^{-7})$$

$$\leq 7 \text{ Events}$$

Although in this case the mass assignments in the reconstruction algorithm would be correct, the ν's will carry off at least 30 MeV, and the reconstructed mass would be below the K^+ mass by at least 4σ.

• $K^+ \to \pi^+\pi^+\pi^-$, *all three* of the π's decaying in flight:

If we assume that two of the π's decay under the constraints described above, and that the third π decay before reaching the drift chamber, the reconstructed mass could in principle be quite close to that of a K^+. If we allow the third π a full nanosecond to reach the drift chamber, the effective branching ratio for $K^+ \to \pi^+\pi^+\pi^-$ will be 2×10^{-9}. Since the acceptance can be no better than that for $K^+ \to \mu^+\nu\mu^+\mu^-$, the expected number events from this channel will be:

$$N \leq 0.002 \times (0.96 \times 10^{10}) \times (2 \times 10^{-9})$$

$$\leq .04 \text{ Events}$$

Hence, this is not a possible background.

‡ The acceptance will certainly be less than that for $K^+ \to \pi^+\mu^+\mu^-$, since at least 30 MeV is lost to the ν's, decreasing the energy available for the charged particles. In addition, the momentum balance at the vertex, which is subject to cuts in the analysis, will tend to be bad.

5.5 THE $K^+ \to \pi^+\pi^0$, $\pi^0 \to \gamma e^+e^-$ BACKGROUND

It is well known that the distribution of opening angles between the e^+ and e^- from $\pi^0 \to \gamma e^+e^-$ is strongly biased toward zero[33,34].

If $K^+ \to \pi^+\pi^0$, $\pi^0 \to \gamma e^+e^-$ events were a significant background component after the final analysis, we would expect the opening angle distribution of events passing the analysis to "pile up" against any cut made in this quantity. Fig. 39 shows the distribution of minimum[§] opening angles (in the $x-y$ plane) for the 37 $K^+ \to \pi^+\pi^-e^+\nu$ events discussed in a previous section of this chapter, and for the three $K^+ \to \pi^+\mu^+\mu^-$ candidates. Also indicated is where any cut was made during the analysis.

We can clearly see that the events are *not* clustered near the cut, but rather the contrary. The $K^+ \to \pi^+\pi^-e^+\nu$ events seem to be biased toward larger angles, and the nearest $K^+ \to \pi^+\mu^+\mu^-$ candidate is over 40° from the cut.

We interpret this to mean that $K^+ \to \pi^+\pi^0$, $\pi^0 \to \gamma e^+e^-$ is *not* a background at the present sensitivity.

It should also be pointed out that the reconstructed mass of any events of this sort will in general be much too high, since the two electrons will be assigned muon masses by the reconstruction algorithm. The probability that the missing γ will carry away just the right energy to make the mass come out to m_K would be very small.

§ The smallest of the three possible opening angles.

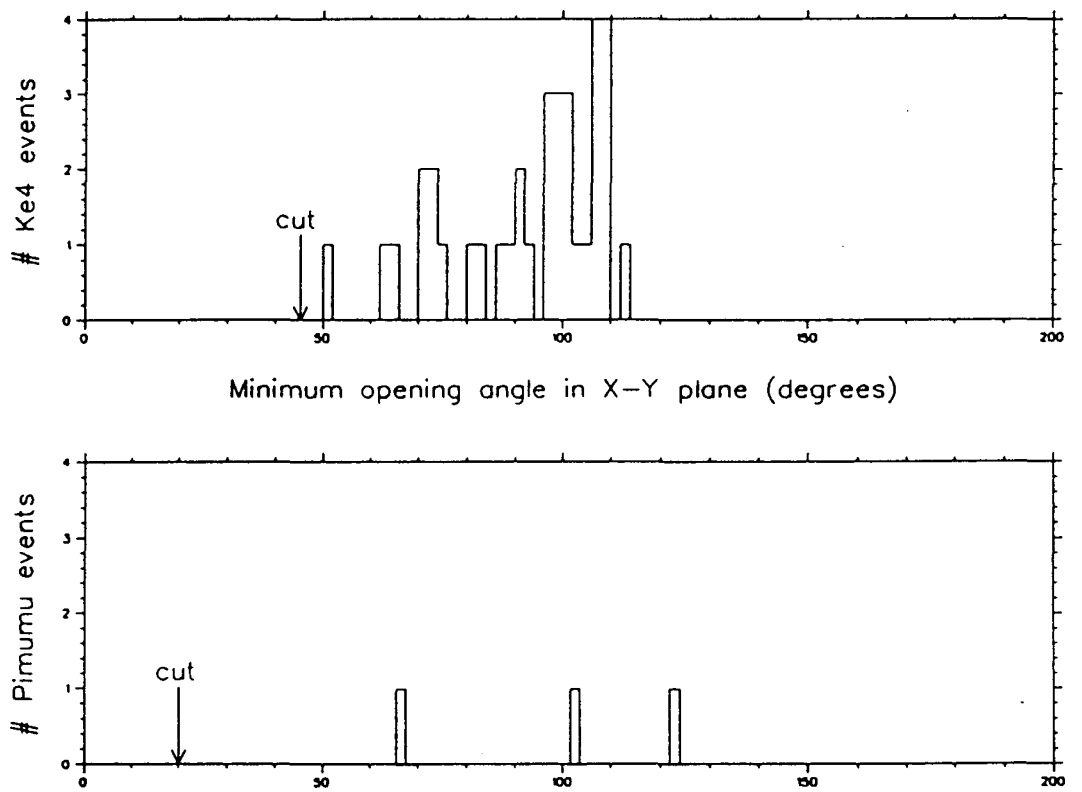

Figure 39. The distribution of minimum opening angles in the $x-y$ plane, for the selected $K^+ \to \pi^+\pi^-e^+\nu$ events (top), and for the $K^+ \to \pi^+\mu^+\mu^-$ candidates (bottom).

6. Conclusions

6.1 The $K^+ \to \pi^+\mu^+\mu^-$ Results

The result of the data analysis was that we are left with three events that are consistent with $K^+ \to \pi^+\mu^+\mu^-$ as defined by the selection cuts used. We have also determined the total acceptance for $K^+ \to \pi^+\mu^+\mu^-$ using these cuts. The least one can do with this information is quote an upper limit:

$$\mathrm{BR}(K \to \pi^+\mu^+\mu^-) \leq \frac{\mathrm{N}(90\%CL)}{(\mathrm{Acceptance}) \times (\mathrm{Exposure})}$$

In previous chapters we found:

Acceptance($K^+ \to \pi^+\mu^+\mu^-$)	0.0034
Exposure	0.96×10^{10}

And from the Particle Data Book:

N(90% CL)(3 events)	6.68

Using these values we can obtain an upper limit for the branching ratio of the process $K^+ \to \pi^+\mu^+\mu^-$:

$$\boxed{\mathrm{BR}(K^+ \to \pi^+\mu^+\mu^-) \leq 2.1 \times 10^{-7} \qquad (90\%\ \mathrm{CL})}$$

This is better than an order of magnitude improvement on the present limit for $K^+ \to \pi^+\mu^+\mu^-$ which is $\mathrm{BR}(K^+ \to \pi^+\mu^+\mu^-) \leq 2.4 \times 10^{-6}$[16].

Interpretation of the results would be somewhat incomplete if we said no more than the above. If we make the assumption that the only background process to enter at this sensitivity is $K^+ \to \pi^+\pi^-e^+\nu$, then we can make a strong argument why two of the three candidates (#1 and #2) have a very low probability of being background.

Each of these events has both positive tracks entering the range stack, and the probability of an e^+ mimicking a μ^+ or a π^+ under these circumstances is minute. A 100 MeV/c e^+ entering the range stack will not only deposit 100 MeV of visible energy in the detector, but will tend to distribute this energy over several counters as it showers. On the other hand, a 100 MeV/c $\pi^+(\mu^+)$ will deposit 32(40) MeV of visible energy in one or two counters. For this reason, candidates #1 and #2 are not consistent with any decay mode containing a final state e^+. Even if we are pessimistic and estimate that 1 in 100 $\pi\pi e\nu$ events will have its e^+ entering the range stack in such a way that it looks like a π^+ or a μ^+, the background rate would be less than 0.1 event since the monte carlo predicts that there should be at most 9 $K^+ \to \pi^+\pi^-e^+\nu$ events in the final sample.* It should also be noted that when the final sample of Monte Carlo $\pi\pi e\nu$ events (11 in total that passed all $\pi\mu\mu$ selection cuts) were examined by hand, *none* had two high momentum positive tracks entering the range stack.

Candidate #3, on the other hand, is as consistent with $K^+ \to \pi^+\pi^-e^+\nu$ as it is with $K^+ \to \pi^+\mu^+\mu^-$, although according the standards defined by the selection cuts it is *not inconsistent* with $K^+ \to \pi^+\mu^+\mu^-$, which is why we were compelled to keep it when quoting the upper limit.

If the assumption that the only background is $K^+ \to \pi^+\pi^-e^+\nu$ is correct, then we are justified in claiming to observe two $K^+ \to \pi^+\mu^+\mu^-$ events, and can therefore quote a central value for the branching ratio:

$$\mathrm{BR}(K \to \pi^+\mu^+\mu^-) = \frac{\mathrm{N}}{(\mathrm{Acceptance}) \times (\mathrm{Exposure})}$$

Resulting in:

$$\boxed{\mathrm{BR}(K^+ \to \pi^+\mu^+\mu^-) = (6.1 \pm 4) \times 10^{-8}}$$

* This estimate is certainly too high since the π^- is not properly accounted for in the monte carlo. (See chapter 5 for more details).

We showed in the introduction that a value for the $K^+ \to \pi^+\mu^+\mu^-$ branching ratio can be obtained by scaling the $K^+ \to \pi^+e^+e^-$ branching ratio by the appropriate kinematic factor. As before, we find:

$$BR(K^+ \to \pi^+\mu^+\mu^-)_{\rm TH} = (5.3 \pm 1) \times 10^{-8}$$

We see that our result is agrees well with this calculation, however it should be noted that the statistical error in our result is high since the it is based on only two events. The probability of measuring n when the true mean of the sample is μ is determined by the Poisson distribution:

$$P(n,\mu) = \frac{\exp^{-\mu}\mu^n}{n!} \tag{6.21}$$

Fig. 40 shows the probability of measuring 2 as a function of the true mean of μ of the Poisson distribution. Notice the characteristic tail toward higher values of μ.

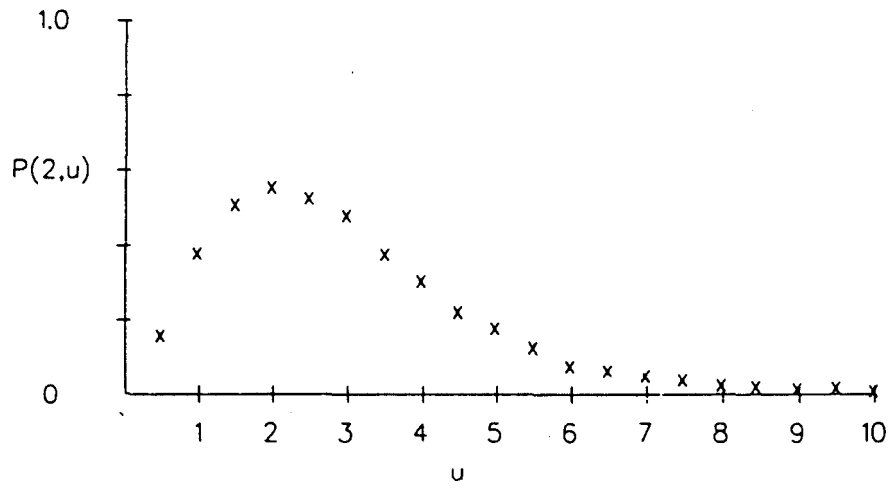

Figure 40. A plot of $P(2,\mu)\, vs\, \mu$, where $P(n,\mu)$ is the Poisson distribution as defined in (6.21).

6.2 The $K^+ \to \mu^+\nu\mu^+\mu^-$ Results

Based on the same three events found in the $\pi\mu\mu$ analysis, we can quote an upper limit on the process $K^+ \to \mu^+\nu\mu^+\mu^-$. Using the acceptance found in chapter 4, we conclude

$$\boxed{\mathrm{BR}(K^+ \to \mu^+\nu\mu^+\mu^-) \leq 3.7 \times 10^{-7} \qquad (90\%\ \mathrm{CL})}$$

assuming a uniform phase-space distribution. This is the first experimental limit set on this decay mode.

6.3 The $K^+ \to \pi^+ H$; $H \to \mu^+\mu^-$ Result

Using the $K^+ \to \pi^+ H$; $H \to \mu^+\mu^-$ $\mathcal{E}_{\mathrm{TOTAL}}$ *vs* M_H relationship found in chapter 4, we can deduce the upper limit for this process as a function of M_H, as shown in Fig. 41. The "bumps" are due to the three $\pi\mu\mu$ candidates found earlier.

Since the branching ratio for $H \to \mu^+\mu^-$ is close to unity for Higgs masses in the range $2m_\mu \geq M_H \geq 2m_\pi$, the above result yields a substantial improvement over the previous upper limit for $K^+ \to \pi^+ H$ in this mass region, which was $\mathrm{BR}(K^+ \to \pi^+ H) \leq 4 \times 10^{-5}$[18].

6.4 Future Improvements

6.4.1 Short Term

The next run of E787 will start in January, 1989. There are two factors in this run that should allow us to increase our $K^+ \to \pi^+\mu^+\mu^-$ sample by about an order of magnitude while improving the quality of the data acquired:

(*i*) Transient recorders will be present on all layers of the range stack. This will allow us to distinguish between e^+'s and (π^+'s or μ^+'s), as well as between μ^-'s and (π^-'s or e^-'s). This ability will provide for a more efficient way of rejecting background events containing e^+'s, e^-'s or π^-'s.

(*ii*) The effective running time should be 6 $\to$ 7 times longer than the last time, at slightly higher intensity.

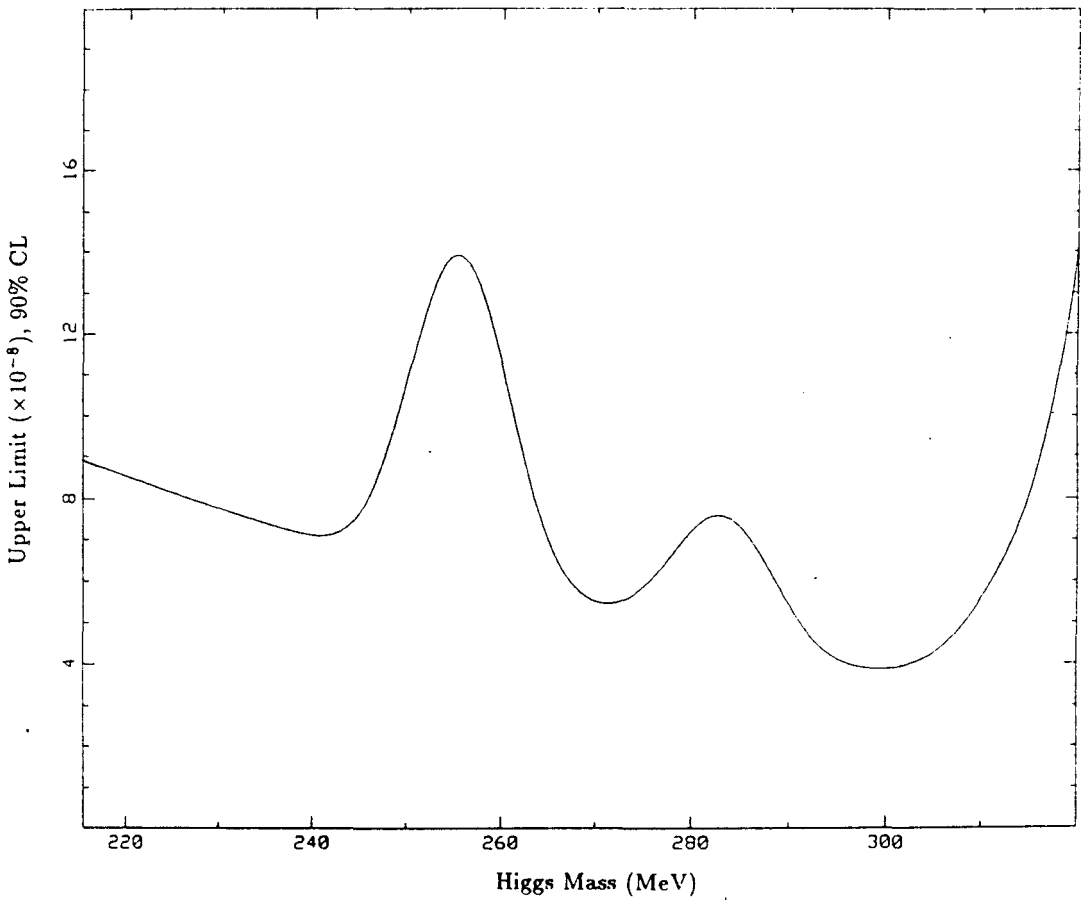

Figure 2. The 90% CL upper limit of BR($K^+ \to \pi^+ H$)·BR($H \to \mu^+\mu^-$) *vs* the mass of the Higgs.

6.4.2 Long Term

A study is under way looking into detector improvements for a possible dedicated $\pi\mu\mu$ run sometime in the future. Some of the possible modifications being studied are:

- Finer segmentation of the inner range stack layers. This might make energy-momentum-range a more powerful technique for particle identification, specifically for distinguishing π's from μ's.
- A smaller target. With the present configuration, most $K^+ \to \pi^+\mu^+\mu^-$ events originate at the edge of the target. Making the target smaller will increase the number of events having all three track entering the drift chamber.
- Improved I-counters having finer segmentation and better light collection.

— A new drift chamber. Since the present drift chamber was not specifically designed to reconstruct low momentum tracks, events containing these tracks are often discarded causing a loss of efficiency. Also, if a reliable z measurement were available for all tracks, including ones having low momentum, the mass resolution would improve significantly allowing easier signal-background separation.

The study is by no means finished, and which (if any) of the above possible suggestions will improve the $\pi\mu\mu$ detection ability is not known.

A. Trigger Hardware Description

A.1 Introduction

This section presents in some detail the functioning of the Level 0/Level 1 trigger hardware built for E-787. The different trigger groups are introduced, and the timing sequence for a typical physics trigger is described. The interaction with Level 2 is also discussed.

A.2 System Overview

At present, the trigger system is divided into three levels $(0, 1, 2)$, each in turn more sophisticated and time consuming. Level 0 is entirely composed of fast combinational logic, and introduces about 40ns of deadtime per event. The Level 1 cycle time is $\sim 7\mu s$, and the level2 software filter involves hundreds of microseconds.

There is at present provision for four different trigger classes or "groups". Each group is unique in the way it issues gate signals to the various detector systems. For instance, Group A triggers all have a particle entering the fiducial volume of the detector ($T \cdot A$ required) and will issue detector* gates based on the timing of $T \cdot A$, and beam gates based on $\check{C}_K$. Group B triggers, on the other hand, are beam

* The *beam* components are the counters and chambers which interact with the K^+up to and including the target, and the *detector* components are everything else. Hence for a normal stopping kaon event, the *beam* components look at the K^+before it decays and *detector* components look at the decay products.

triggers and all gates will be based on the timing of $\check{C}_K$. Table I shows the group assignments.

Group	Description	Beam	Detector	Comment
A	Physics triggers	$\check{C}_K$	T · A	T · A required
B	Beam triggers	$\check{C}_K$	$\check{C}_K$	*no* T · A required
C	Cosmic triggers	T · A	T · A	T · A required
D	Other	Ext.	Ext.	timing from trigger source

Table I: Trigger groups

A.3 Group A

Group A contains the triggers of physics interest. This includes those searching for rare K^+ decay modes, the RS calibration trigger, and minimum bias triggers looking for π^+ or K^+ beam signals in coincidence with a T · A.

This group deserves special attention as it is more complicated than the others, using several unique boards and buses, and being the only group for which Level 1 triggers are implemented. A schematic diagram of the level 0 system is shown in figure 42 Each board shown will be discussed below, although the reader is referred to the actual schematics for connector and wiring details.

To illustrate the sequence of events for a group A trigger, consider a K^+ stopping in the target and decaying into (among other things) a π^+ that enters the range stack. Like other group A triggers, the Level 0 deadtime is initiated by T · A. The range (stopping layer) of the π^+ is deduced by the Range Cards (RC1B), while pulse heights from the range stack hextants, barrel veto, and end-caps are summed by fan-in modules. This total energy information is discriminated to produce veto signals, which are latched and placed on the trigger bus by the Trigger Transmitter (TT1A). The stopping layer information from the range crates is also latched in this way, along with other external conditions such as delayed coincidence, Čerenkov data, and topology information from the PHI boards (described later). The Trigger Cards (TB1B; described in the Trigger Bus section) make a Level 0 decision based on the state of the trigger bus.

As mentioned above, all group A triggers (and some others) require a "T · A" as a basic timing strobe. For each sector, this signal is the OR of the T-counter ends

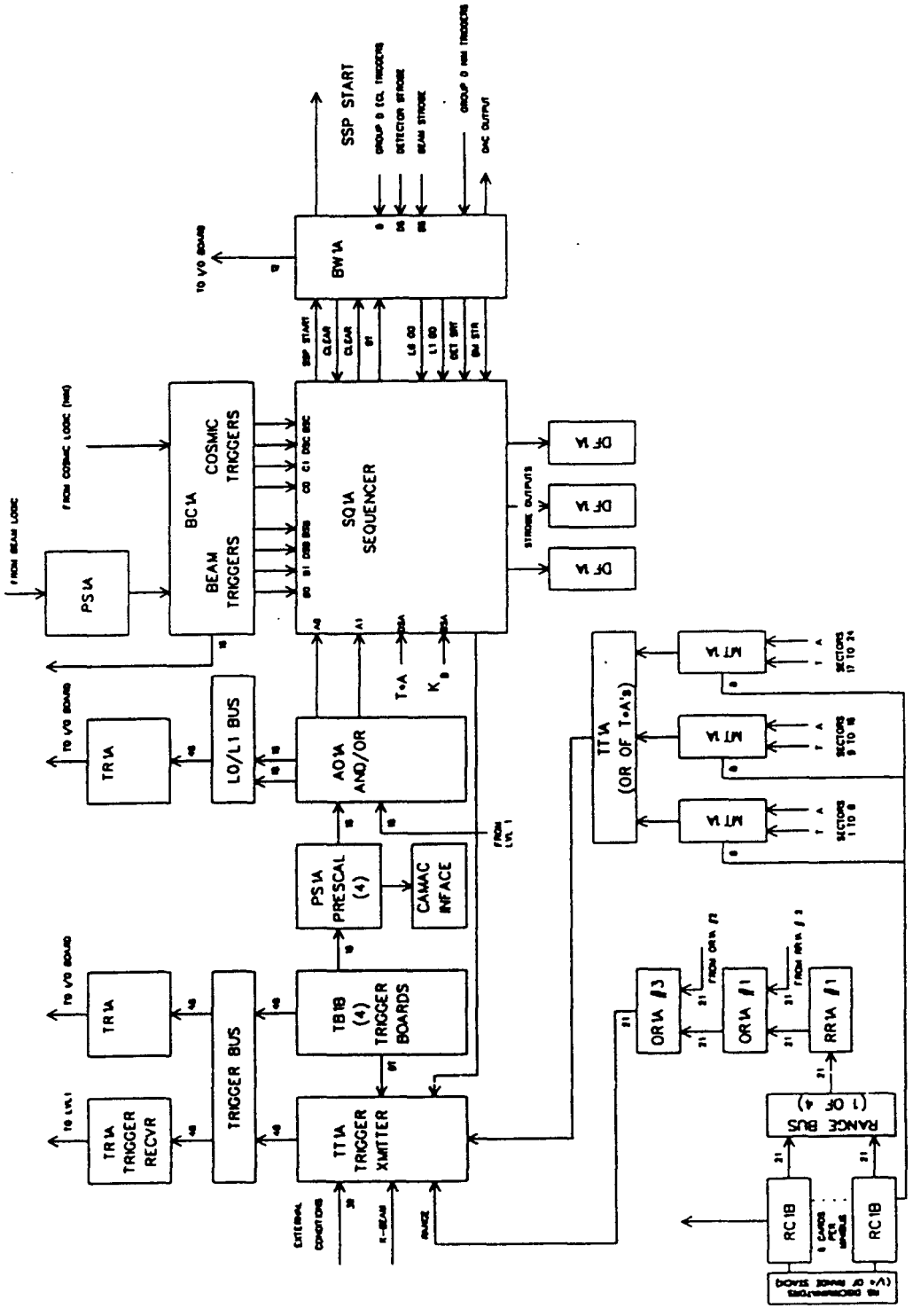

Figure 42. Block diagram of the Level 0 trigger system.

ANDed with the AND of the A-counter ends, i.e. $T \cdot A = (T_{+z} + T_{-z}) \cdot (A_{+z} \cdot A_{-z})$. The cable lengths are such that the leading edge of T · A from a given sector is determined by the mean arrival time of A_{+z} and A_{-z} from that sector. This time averaging is performed by three mean-timer boards (MT1A), which also form the T · A signals. Each mean-timer has T and A inputs from both ends of eight sectors, and has as its outputs the eight A signals mean-timed, and the OR of all eight T · A's on the board. The final T · A to be used as a strobe is formed by OR-ing these three signals on a separate board (TA1A) and regenerating to get a constant output width.

If all 16 Level 0 triggers are *false*, nothing further happens and the next T·A that comes along will start the process again, latching information from the new event onto the trigger bus. In this case the dead-time is simply the width of T · A, about 40ns. If any Level 0 trigger is *true*, the trigger cards issue an interim inhibit (DT) signal to the transmitter. This additional deadtime is about 50ns long, and prevents any subsequent T · A from latching new information on the trigger bus until the Level 0 *GO* signal has had time to propagate through its Prescaler (PS1A) channel, the AND/OR board (AO1A) , and the Sequencer (SQ1A). The prescaling factor is adjustable from 1 to 2^{20}, with the option of passing the pulses "untouched". Each PS1A board contains four channels, and the prescale factor of all 16 channels is readable via a CAMAC interface.

If the prescaler output is *true*, the Sequencer will strobe the ADC's and TDC's, send a *GO* to the Level 1 trigger electronics, and set a flip-flop which further extends the DT signal. The timing of the strobes is determined by the group A beam strobe (BSA) and detector strobe (DSA) inputs. These are fanned out by the Sequencer into Delay-Width-Fanout boards (DF1A), which send the actual strobes to the ADC's and TDC's. In the case of $K^+ \rightarrow \pi^+ \nu \bar{\nu}$, the Level 1 decision is based on a refined range measurement*. This is implemented by creating an MLU address out of the Z information from the range stack chambers and associated electronics, the Z position of the decay vertex in the target, and the range in the target. The $K^+ \rightarrow \pi^+ \mu^+ \mu^-$ level 1 trigger demands that the number of hit target elements is greater that a preset number.

If the Level 1 decision is *true*, the Sequencer sends a *start* signal to the trigger SSP†. It then waits for the SSP's to read out the ADC's and TDC's and perform the

* At present, this is the only kind of Level 1 trigger associated with Group A, and it will be discussed in greater detail later in this note.

† The SSP *GO* signal is sent via the "Bells & Whistles" board, described in the group D section of this note.

Level 2 calculations. When the SSP's are finished, the master will send a *clear* signal to the Sequencer, which in turn issues its own set of signals to restart the TDC's and clear the ADC's. After waiting $7\mu s$ for the resetting to finish, the DT signal to the transmitter is lowered and the trigger is "restarted". If a Level 1 *false* is returned, the above restarting and clearing sequence is carried out without interrupting the SSP's. The minimum deadtime in this case is $7\mu s$. This is a combination of the time it takes to clear/restart the ADC's/TDC's (about $2\mu s$) and a $5\mu s$ hold invoked to allow the transient recorders to look at least $5\mu s$ "into the past" of any event.

The function of the AND/OR board in the above is twofold: it makes sure the Level 0 and Level 1 triggers are of the same kind, for example $K^+ \rightarrow \pi^+\mu^+\mu^-$, and it checks that the relative timing of the Level 0 and 1 signals are correct.

A.3.1 Range Bus

A detailed description of the Range Cards is given in Technote 107. Each takes the discriminator signals from one complete range stack sector, and deduces which layers (if any) in that sector belong to a positive charged track. A counter is considered part of such a track if both its ends show signals in coincidence with a $T \cdot A$ in its own sector, or in either of the two sectors "up track" from it.

Table II shows the assignments of the 21 signals each Range Card presents to its backplane. (CT represents the "charged track" requirement described above).

Pin	Signal	Pin	Signal	Pin	Signal
$C3$	$B \cdot CT$	$C11$	$16 \cdot CT$	$C21$	19
$C4$	$C \cdot CT$	$C12$	16	$C23$	$20 \cdot CT$
$C5$	$11 \cdot CT$	$C14$	$17 \cdot CT$	$C25$	20
$C6$	$12 \cdot CT$	$C16$	17	$C26$	$21 \cdot CT$
$C7$	$13 \cdot CT$	$C17$	$18 \cdot CT$	$C28$	21
$C8$	$14 \cdot CT$	$C19$	18	$C29$	A
$C9$	$15 \cdot CT$	$C20$	$19 \cdot CT$	$C30$	$T \cdot A$

Table II: Range Card Backplane Assignments

The Range Cards are arranged in four groups of six, each group having the above signals wire-OR ed on an ECL backplane. The resulting 21 bits from each group are further OR ed by the OR-1A cards resulting in a final 21 bit range word,

logically equivalent to all 24 Range Cards being connected by one long backplane, rather than by four shorter ones[‡] .

A.3.2 Trigger Bus

Up to 16 group A Level 0 triggers can be implemented at any one time, four on each of four wirewrap trigger cards. These cards make their decisions based on the information latched onto the trigger bus by the transmitter board. The actual triggers are built using ECL logic chips appropriately wired together by the user. The state of the latches on the transmitter, and hence the levels observed by the trigger boards, will be changed by every T · A unless DT is asserted.

Table III shows tentative assignments for the 16 group A triggers.

Board	Chan.	Trigger	Board	Chan.	Trigger
A1	1	$K^+ \to \pi^+ \nu\bar{\nu}$	A2	1	$K_{\mathbf{beam}} \cdot T \cdot A$
A1	2	$K^+ \to \pi^+ \nu\bar{\nu}$ (p)	A2	2	$K^+ \to \mu^+ \nu$ (2)
A1	3	$K^+ \to \pi^+ \nu\bar{\nu}$ (2)	A2	3	$K^+ \to \mu^+ \nu$ (1)
A1	4	$K^+ \to \pi^+ \gamma\gamma$	A2	4	$K^+ \to \pi^+ \pi^0$
A3	1	$K^+ \to \pi^+ \mu^+ \mu^-$	A4	1	development
A3	2	$K^+ \to \pi^+ \gamma\gamma$ (p)	A4	2	development
A3	3	unassigned	A4	3	development
A3	4	unassigned	A4	4	development

Table III, Group A triggers

As mentioned above, the trigger bus carries the logical information upon which Level 0 decisions are made. It is composed of 48 differential ECL signals, whose

‡ Segmenting the backplane serves to minimize the distance from any one trigger card to a receiver, thereby increasing the effective bandwidth of the bus.

assignments are shown below in Table IV.

Line	Signal	Line	Signal	Line	Signal
$T1$	$B \cdot CT$	$T17$	$K_{\mathbf{beam}}$	$T33$	unassigned
$T2$	$C \cdot CT$	$T18$	$\pi_{\mathbf{beam}}$	$T34$	unassigned
$T3$	$11 \cdot CT$	$T19$	$K_{\mathbf{targ}}$	$T35$	unassigned
$T4$	$12 \cdot CT$	$T20$	Delayed coin.	$T36$	unassigned
$T5$	$13 \cdot CT$	$T21$	BV	$T37$	unassigned
$T6$	$14 \cdot CT$	$T22$	ECM	$T38$	unassigned
$T7$	$15 \cdot CT$	$T23$	ECP	$T39$	unassigned
$T8$	$16 \cdot CT$	$T24$	I-Counter	$T40$	unassigned
$T9$	$17 \cdot CT$	$T25$	unassigned	$T41$	Calibration
$T10$	$18 \cdot CT$	$T26$	unassigned	$T42$	Physics
$T11$	$19 \cdot CT$	$T27$	unassigned	$T43$	T · A/2
$T12$	$20 \cdot CT$	$T28$	N(T · A)=1	$T44$	T · A/4
$T13$	$21 \cdot CT$	$T29$	N(T · A)=2	$T45$	T · A/8
$T14$	19	$T30$	N(T · A)=3	$T46$	T · A/16
$T15$	20	$T31$	N(T · A)> 3	$T47$	T · A(not lat)
$T16$	21	$T32$	unassigned	$T48$	$K_{\mathbf{beam}}$(not lat)

Table IV, Trigger Bus Assignments

The state of the trigger bus can be examined via receiver boards (TR1A), which read the 48 bus lines and present them to the front panel as differential ECL signals. As well as being useful for timing and debugging, these signals will be read by the data acquisition system through the I/O boards and will be made "part" of any event written to tape.

The Sequencer and AND/OR boards reside on "their own" 48 signal backplane segment, the Level 0/Level 1 bus. They both transmit bits (on mutually exclusive lines) to this bus, but neither reads from it. The information transmitted by the AND/OR board reflects the state of the 16 Level 0 triggers and their Level 1 counterparts. These data are then read by a receiver (as above) and fed into an I/O board to be accessed by the SSP's, which will execute different filtering algorithms depending on the particular type of Level 0/1 trigger that passed.

A.4 THE ϕ BOARD

The phi board is basically a tailor made memory lookup unit based on 10ns ECL PROM's. The board takes the 24 T and 24 A signals from the range-crates, forms the relevant coincidences and counts the number of T · A clusters found.* The board outputs, among other things, the number of clusters found. (This number is demanded to be 2 or 3 by the level 0 $K^+ \rightarrow \pi^+\mu^+\mu^-$ trigger).

The board can also be programmed to look for other unique track topologies, although this feature has yet to be used.

A.4.1 The Linear Sums

The total energy in a given system was obtained by combining all the phototube signals using linear fan-in modules. The barrel veto and endcap sums were discriminated using appropriate thresholds (5 MeV and 10 MeV respectively) and supplied as external conditions on the trigger bus.

The range stack energy was combined into six sums of four sectors each. These were individually discriminated with thresholds of 10 MeV, and the resulting *hextant bits* were available for use at level 1 .

A.5 GROUP B

The group B (beam) triggers do *not* require a T · A , and all the timing strobes associated with them will be based on $\check{C}_K$. The actual beam logic will be done in NIM, and the signal reaching the trigger system will simply be prescaled and fed into the Sequencer. The prescaler will be the same kind used for group A triggers, and a kluge board (BC1A) will be used to latch the prescaled beam trigger and output the proper strobes and levels to the Sequencer and I/O boards.

* "Clustering" means that adjacent T · A do not count separately.

A.6 Group C

Once generated, these triggers will be prescaled and fed through the BC1A board to the Sequencer and I/O boards. In this respect they are treated as group B triggers, except their timing strobes are based on T · A rather than K_{beam}.

A.7 Group D

This class of triggers is designed to be "user accessible", and special effort has been made to make them easy to implement. To this end, a special "Bells & Whistles" (BW1A) board has been designed and built that allows the casual user to input a trigger source (pulser etc.) simply by plugging into a NIM input on the front panel. The BW1A generates the required timing strobes and handles all communication with the Sequencer and I/O boards. It is also designed to generate an End-Cap calibration trigger, based on $K^+ \rightarrow \mu^+\nu$, which is otherwise difficult since this trigger does not fit neatly into any of the other groups.

The other function performed by the BW1A board is to look for and, if desired, correct ADC gate faults (the generation of beam and detector strobes too widely separated in time), and SSP start faults (starting the SSP's without having gated the ADC's). A related feature is its ability to generate its own Level 2 *done* signal, allowing the trigger system to be cycled for testing without the need for computer intervention.

A.8 The Trigger Words

As mentioned above, various levels are passed on to fastbus I/O boards via receiver boards which sit on the various backplane sections. These bits will be written as part of the event buffer, and some will be used by the SSP's to make decisions.

At present, seven 32 bit "trigger words" have been assigned, and are outlined below. The low order byte of the first word is comprised of the Level 0 and Level 1 trigger results for the four groups, as presented to the Sequencer. The upper three

bytes are for general information, and some suggestions are shown.

Bit	Signal	Bit	Signal	Bit	Signal
2^0	A Level 0	2^8	Spill Gate	2^{16}	NTA 0
2^1	A Level 1	2^9	ADC gate fault	.	.
2^2	unassigned	2^{10}	SSP gate fault	2^{20}	NTA 4
2^3	B Level 1	2^{11}	End-of-spill	2^{21}	RSHEX 1
2^4	unassigned	2^{12}	SB0	.	.
2^5	C Level 1	2^{13}	SB1	2^{26}	RSHEX 6
2^6	unassigned	2^{14}	SB2	2^{27}	$N_{TG} > 25$
2^7	D Level 1	2^{15}	SB3	2^{27}	$N_{TG} > 12$

Table V(i): Word 1 bit assignments

The second word contains information about the triggers in group A. Each of the 16 group A triggers is assigned two bits (one for Level 0 and one for Level 1), and these bits make up the second trigger word.*

Board	Chan.	Lvl 0	Lvl 1	Board	Chan.	Lvl 0	Lvl 1
A1	1	2^0	2^{16}	A2	1	2^4	2^{20}
A1	2	2^1	2^{17}	A2	2	2^5	2^{21}
A1	3	2^2	2^{18}	A2	3	2^6	2^{22}
A1	4	2^3	2^{19}	A2	4	2^7	2^{23}
A3	1	2^8	2^{24}	A4	1	2^{12}	2^{28}
A3	2	2^9	2^{25}	A4	2	2^{13}	2^{29}
A3	3	2^{10}	2^{26}	A4	3	2^{14}	2^{30}
A3	4	2^{11}	2^{27}	A4	4	2^{15}	2^{31}

Table V(ii): Word 2 bit assignments

* During the run, the 2^{12}'th and 2^{13}'th bit were stuck HIGH.

The third trigger word is assigned to groups B, C, and D. Since few (if any) of these triggers will have Level 1 components, no distinction is made between Level 0 and Level 1.

Group	Signal	Bit	Group	Signal	Bit
B	$K_{\mathbf{beam}}$	2^0	D	Endcap calib.	2^{16}
B	$\pi_{\mathbf{beam}}$	2^1	D	unassigned	2^{17}
B	unassigned	2^2	D	unassigned	2^{18}
B	unassigned	2^3	D	unassigned	2^{19}
B	unassigned	2^4	D	unassigned	2^{20}
B	unassigned	2^5	D	unassigned	2^{21}
B	unassigned	2^6	D	unassigned	2^{22}
B	unassigned	2^7	D	unassigned	2^{23}
C	T · A	2^8	D	Pulser	2^{24}
C	T · A · Tgt	2^9	D	End-of-Spill	2^{25}
C	unassigned	2^{10}	D	User 3	2^{26}
C	unassigned	2^{11}	D	Target LED	2^{27}
C	unassigned	2^{12}	D	User 5	2^{28}
C	unassigned	2^{13}	D	User 6	2^{29}
C	unassigned	2^{14}	D	User 7	2^{30}
C	T · A · IC	2^{15}	D	User 8	2^{31}

Table V(iii): Word 3 bit assignments

The fourth word contains information from the inputs (lower order 16 bits) and outputs (upper order 16 bits) of MLU # 1 used in the Level 1 refined range trigger.

Bit	Signal	Bit	Signal	Bit	Signal	Bit	Signal
2^0	Z_{RS} 0	2^8	N_{TG} 3	2^{16}	ΔZ 0	2^{24}	G1
2^1	Z_{RS} 1	2^9	E_{TG} 0	2^{17}	ΔZ 1	2^{25}	G2
2^2	Z_{RS} 2	2^{10}	E_{TG} 1	2^{18}	ΔZ 2	2^{26}	G3
2^3	Z_{RS} 3	2^{11}	E_{TG} 2	2^{19}	ΔZ 3	2^{27}	G4
2^4	Z_{RS} 4	2^{12}	E_{TG} 3	2^{20}	NGOOD 0	2^{28}	G5
2^5	N_{TG} 0	2^{13}	N=1	2^{21}	NGOOD 1	2^{29}	G6
2^6	N_{TG} 1	2^{14}	unassigned	2^{22}	NGOOD 2	2^{30}	G7
2^7	N_{TG} 2	2^{15}	NGOOD 4	2^{23}	NGOOD 3	2^{31}	G8

Table V(iv): Word 4 bit assignments

The fifth word contains information from the inputs (lower order 16 bits) and outputs (upper order 16 bits) of MLU # 2 used in the Level 1 refined range trigger.

Bit	Signal	Bit	Signal	Bit	Signal	Bit	Signal
2^0	SL 0	2^8	(Level 1) 0	2^{16}	G9	2^{24}	G17
2^1	SL 1	2^9	(Level 1) 1	2^{17}	G10	2^{25}	G18
2^2	SL 2	2^{10}	(Level 1) 2	2^{18}	G11	2^{26}	G19
2^3	SL 3	2^{11}	(Level 1) 3	2^{19}	G12	2^{27}	G20
2^4	unass.	2^{12}	HEX L1 go	2^{20}	G13	2^{28}	G21
2^5	unass.	2^{13}	Stop Half	2^{21}	G14	2^{29}	G22
2^6	unass.	2^{14}	Stop Hex 0	2^{22}	G15	2^{30}	G23
2^7	unass.	2^{15}	Stop Hex 1	2^{23}	G16	2^{31}	G24

Table V(v): Word 5 bit assignments

The final two trigger words reflect the bits latched on the trigger bus. Since the trigger bus is only 48 signals wide, the high order 16 bits of trigger word seven can be used for future expansion.

Bit	Signal	Bit	Signal	Bit	Signal	Bit	Signal
2^0	T1	2^8	T9	2^{16}	T17	2^{24}	T25
2^0	T2	2^9	T10	2^{17}	T18	2^{25}	T26
2^0	T3	2^{10}	T11	2^{18}	T19	2^{26}	T27
2^0	T4	2^{11}	T12	2^{19}	T20	2^{27}	T28
2^0	T5	2^{12}	T13	2^{20}	T21	2^{28}	T29
2^0	T6	2^{13}	T14	2^{21}	T22	2^{29}	T30
2^0	T7	2^{14}	T15	2^{22}	T23	2^{30}	T31
2^0	T8	2^{15}	T16	2^{23}	T24	2^{31}	T32

Table V(vi): Word 6 bit assignments

Bit	Signal	Bit	Signal	Bit	Signal	Bit	Signal
2^0	T33	2^8	T41	2^{16}	unassigned	2^{24}	unassigned
2^1	T34	2^9	T42	2^{17}	unassigned	2^{25}	unassigned
2^2	T35	2^{10}	T43	2^{18}	unassigned	2^{26}	unassigned
2^3	T36	2^{11}	T44	2^{19}	unassigned	2^{27}	unassigned
2^4	T37	2^{12}	T45	2^{29}	unassigned	2^{28}	unassigned
2^5	T38	2^{13}	T46	2^{21}	unassigned	2^{29}	unassigned
2^6	T39	2^{14}	T47	2^{22}	unassigned	2^{30}	unassigned
2^7	T40	2^{15}	T48	2^{23}	unassigned	2^{31}	unassigned

Table V(vii): Word 7 bit assignments

B. Trigger Implementation

B.1 Beam Logic

The "beam" trigger signals, K_{beam} and K_{targ}, were formed as shown in figure 43. These were used as external conditions* by the Level 0 trigger.

B.2 Timing Strobes

The *detector* timing strobe was derived from the Level 0 trigger T · A signal. As described in the trigger hardware section, the T · A signal is the result of ORing the T · A's from all 24 sectors. In order to minimize the uncertainty in the timing of the final OR-ed T · A , the cables of the A-counters were trimmed to align the outputs of the meantiming circuits. The uncertainty in this alignment was ~ 1 ns.

The *beam* timing strobe was derived from the Čerenkov $\check{C}_K$ signal.

B.3 Group A Triggers

B.3.1 Level 0

A list of the Level 0, Group A triggers which were implemented during the run is given on the next page.

* See the section on trigger hardware for an explanation of this.

Definitions of Implemented Level 0 Group A Triggers:

$K^+ \to \pi^+\nu\bar{\nu}(1)$ $(T \cdot A) \cdot B_{\mathrm{CT}} \cdot K_{\mathrm{B}} \cdot K_{\mathrm{T}} \cdot IC \cdot DC \cdot \overline{(19_{\mathrm{CT}} + 20_{\mathrm{CT}} + 21_{\mathrm{CT}} + BV + ECM + ECP)}$

$K^+ \to \pi^+\nu\bar{\nu}(2)$ $(T \cdot A) \cdot B_{\mathrm{CT}} \cdot K_{\mathrm{B}} \cdot K_{\mathrm{T}} \cdot IC \cdot DC \cdot \overline{(12_{\mathrm{CT}} + 13_{\mathrm{CT}} + 14_{\mathrm{CT}} + 15_{\mathrm{CT}} + 16_{\mathrm{CT}} + 17_{\mathrm{CT}} + 18_{\mathrm{CT}})} \cdot \overline{(19 + 20 + 21 + BV + ECM + ECP)}$

$K^+ \to \pi^+\pi^0$ $(T \cdot A) \cdot B_{\mathrm{CT}} \cdot K_{\mathrm{B}} \cdot K_{\mathrm{T}} \cdot \overline{(19_{\mathrm{CT}} + 20_{\mathrm{CT}} + 21_{\mathrm{CT}})}$

$K^+ \to \mu^+\nu(1)$ $(T \cdot A) \cdot B_{\mathrm{CT}} \cdot K_{\mathrm{B}} \cdot K_{\mathrm{T}} \cdot (19_{\mathrm{CT}} + 20_{\mathrm{CT}} + 21_{\mathrm{CT}})$

$K^+ \to \mu^+\nu(2)$ $(T \cdot A) \cdot B_{\mathrm{CT}} \cdot K_{\mathrm{B}} \cdot K_{\mathrm{T}} \cdot 21_{\mathrm{CT}} \cdot BV$

$K^+ \to \pi^+\gamma\gamma$ $(T \cdot A) \cdot B_{\mathrm{CT}} \cdot C_{\mathrm{CT}} \cdot 11_{\mathrm{CT}} \cdot 12_{\mathrm{CT}} \cdot 13_{\mathrm{CT}} \cdot 14_{\mathrm{CT}} \cdot 15_{\mathrm{CT}}) \cdot K_{\mathrm{B}} \cdot K_{\mathrm{T}} \cdot IC \cdot DC \cdot (BV + ECM + ECP) \cdot \overline{(19_{\mathrm{CT}} + 20_{\mathrm{CT}} + 21_{\mathrm{CT}})}$

$K^+ \to \pi^+\mu^+\mu^-$ $(T \cdot A) \cdot K_{\mathrm{B}} \cdot K_{\mathrm{T}} \cdot DC \cdot (2T \cdot A's \text{ or } 3T \cdot A's) \cdot \overline{(C_{\mathrm{CT}} + 11_{\mathrm{CT}} + 12_{\mathrm{CT}} + 13_{\mathrm{CT}} + 14_{\mathrm{CT}} + 15_{\mathrm{CT}} + 16_{\mathrm{CT}} + 17_{\mathrm{CT}} + 18_{\mathrm{CT}})} \cdot \overline{(19 + 20 + 21 + BV + ECM + ECP)}$

Where:

X_{CT}	The X'th Range Stack layer is part of a charged track
K_{B}	$\check{C}_{\mathrm{K}} \cdot B4 \cdot E_{\mathrm{Tg}}$
K_{T}	$K_{\mathrm{B}} \cdot \overline{VC}$
IC	I-Counter sum above 0.15 MeV
VC	V-Counter sum above 2.0 MeV
BV	Barrel Veto above 5 MeV
ECM	Upstream Endcap above 10 MeV
ECP	Downstream Endcap above 10 MeV
DC	Delayed coincidence between $\check{\mathrm{C}}_{\mathrm{K}}$ and IC (~ 2) ns

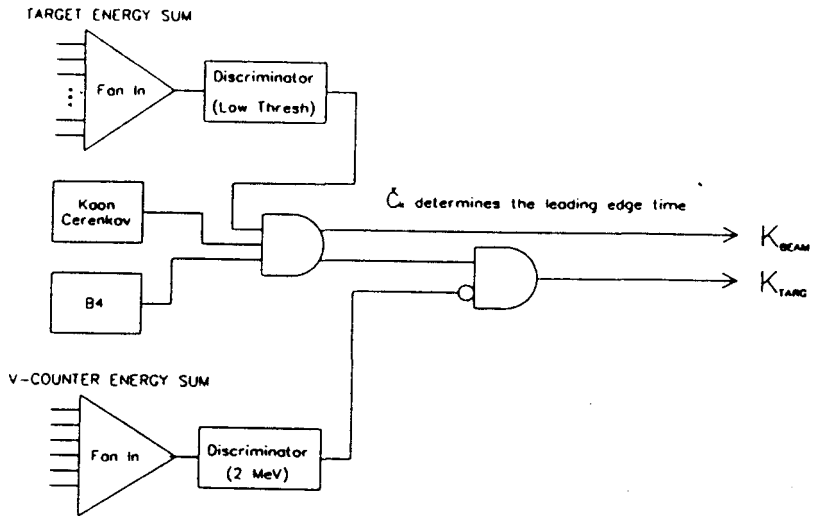

Figure 43. Logic diagram showing how the K_{beam} and K_{targ} signals were formed.

B.3.2 Level 1

The Group A, Level 1 triggers were defined in the following way:

$K^+ \rightarrow \pi^+\nu\bar{\nu}(1)$	Range and Hextant
$K^+ \rightarrow \pi^+\nu\bar{\nu}(2)$	none
$K^+ \rightarrow \pi^+\pi^0$	none
$K^+ \rightarrow \mu^+\nu(1)$	none
$K^+ \rightarrow \mu^+\nu(2)$	none
$K^+ \rightarrow \pi^+\gamma\gamma$	Hextant
$K^+ \rightarrow \pi^+\mu^+\mu^-$	N_{TARG}

Where:

Range	Dip angle information from the inner layer RSPCs and the number of hit target elements are combined to refine the crude stopping layer range estimate.
Hextant	No more than one non-adjacent range stack hextant above 10 MeV.
N_{TARG}	Number of struck target elements greater than 20

B.4 Group B C and D Triggers (Level 0 Only)

Definitions of Implemented Level 0 Group B Triggers

K_{BEAM}	K_{BEAM}

Definitions of Implemented Level 0 Group C Triggers

Cosmic	$(T \cdot A)\cdot IC$

Definitions of Implemented Level 0 Group D Triggers

Pulser	
Target LED	
Endcap Calib	$EC \cdot \overline{(T \cdot A + \Sigma E_{RS} + BV)}$

C. The E787 Collaboration

M.S. Atiya, I-H. Chiang, J. Frank, J. Haggerty, M. Ito,
T.F. Kycia, K.K. Li, L.S. Littenberg, R.C. Strand, C. Woody

Brookhaven National Laboratory

D.S. Akerib, D.R. Marlow, P.D. Meyers,
M.A. Selen, F.C. Shoemaker, A.J.S. Smith

Princeton University

G. Azuelos, E. Blackmore, D. Bryman,
L. Felawka, P. Kitching, Y. Kuno, J. Macdonald,
T. Numao, P. Padley, J-M. Poutissou
R. Poutissou, J. Roy

TRIUMF

W.C. Louis

Los Alamos National Laboratory

References

1. see for example E.D. Commins and P.H. Bucksbaum. "*Weak interactions of leptons and quarks*", Cambridge University Press (1983) and references therein.
2. Y. Asano, et al., Phys. Lett. **107B**, 159 (1981)
3. A. Pais, *Phys. Rev.* **86**, 663 (1952)
4. M. Gell-Mann, *Phys. Rev.* **92**, 833 (1953)
5. K. Nishijima, *Prog. Theor. Phys.* **13**, 285 (1955)
6. T.D. Lee and C.N. Yang *Phys. Rev.* **104**, 254 (1956)
7. J.H. Christenson, J. Cronin, V. Fitch, and R. Turlay, *Phys. Rev. Lett.* **13**, 138 (1964)
8. S.L. Glashow, J. Iliopoulos, and L. Maiani, *Phys. Rev. D* **2**, 1285 (1970)
9. P.A.M. Dirac, *Proc. Roy. Soc.* **A117**, 610 (1928)
10. R.P. Feynman, and M. Gell-Mann, *Phys. Rev.* **109**, 193 (1958)
11. M. Kobayashi, and K. Maskawa, *Prog. Theor. Phys.* **49**, 282 (1972)
12. T. Inami, and C.S. Lim, *Prog. Thor. Phys.* **65**, 297 (1981)
13. J. Ellis, J.S. Hagelin, and S. Rudaz, *Phys. Lett.* **B192**, 201 (1987)
14. G. Ecker, A. Pich, and E. de Rafael, *Nuc. Phys. B* **291**, 692 (1987)
15. D.S. Beder, and G.V. Dass, *Phys. Lett.* **59B**, 444 (1975)
16. Bisi *et al.*, *Nuovo Cim.* **35**, 768 (1965)
17. Camerini *et al.*, *Nuovo Cim.* **37**, 1795 (1965)
18. T. Yamazaki *et al.*, *Phys. Rev. Lett.* **52**, 1089 (1984)
19. S. Dawson, Submitted to *Proceedings of the 1988 DPF Meeting*, Storrs, Conn.
20. S. Raby, G.B. West, C.M. Hoffman, Los Alamos Preprint, LA-UR-88-2667

21. A.M. Diamant-Berger *et al.*, *Phys. Lett.* **62B**, 485 (1976)
22. R. S. Chivulula and A. V. Manohar, *Boston Univ. preprint* BUHEP-88-7
23. E787 Collaboration Progress report, October 9, 1985
24. E787 Technical Note 127
25. E787 Technical Note 102
26. E787 Technical Note 138
27. E787 Technical Note 144
28. E787 Technical Note 126
29. E787 Technical Note 146
30. M. D. Hildreth, Princeton University senior thesis, 1988
31. L. Rosselet *et al. Phys. Rev. D* **3**, 574 (1977)
32. M.P. Guthrie, R.G. Alsmiller, H.W. Bertini, Oak Ridge Preprint, August, 1968
33. M. A. Schardt, J. S. Frank *et al.*, *Phys. Rev. D* **23**, 639 (1981)
34. K. O. Mikaelian and J. Smith, *Phys. Rev. D* **5**, 1763 (1972)